Etude des propriétés des magnétotransport de (Ge,Mn) semiconducteur ferromagnétique sur GaAs(001) pour lélectronique de spin

Ing-Song Yu

▶ **To cite this version:**

Ing-Song Yu. Etude des propriétés des magnétotransport de (Ge,Mn) semiconducteur ferromagnétique sur GaAs(001) pour lélectronique de spin. Matière Condensée [cond-mat]. Université Joseph-Fourier - Grenoble I, 2010. Français. NNT : . tel-00526338

HAL Id: tel-00526338

https://theses.hal.science/tel-00526338

Submitted on 14 Oct 2010

HAL is a multi-disciplinary open access archive for the deposit and dissemination of scientific research documents, whether they are published or not. The documents may come from teaching and research institutions in France or abroad, or from public or private research centers.

L'archive ouverte pluridisciplinaire **HAL**, est destinée au dépôt et à la diffusion de documents scientifiques de niveau recherche, publiés ou non, émanant des établissements d'enseignement et de recherche français ou étrangers, des laboratoires publics ou privés.

NATIONAL TAIWAN UNIVERSITY

THESE

Pour obtenir le grade de

DOCTEUR DE L'UNIVERSITE DE GRENOBLE
Spécialité : Physique de Matière Condensée & Rayonnement

Préparée dans le cadre d'une cotutelle entre
L'UNIVERSITE DE GRENOBLE ET L'UNIVERSITE NATIONALE DE TAIWAN

Arrêtés ministériels : 6 janvier 2005 - 7 août 2006

Présentée et soutenue publiquement par

Yu Ing-Song

le 31 juillet 2010

Etude des propriétés des magnétotransport de (Ge,Mn) semiconducteur ferromagnétique sur GaAs(001) pour lélectronique de spin

---

Thèse dirigée par **Cibert Joël**

JURY

- **Monsieur Kuroda Shinji** - **Professor/Japon** - **Président, Rapporteur**
- **Monsieur Hung Kuan-Ming** - **Professor/Taïwan** - **Rapporteur**
- **Monsieur Jamet Matthieu** - **Professor/France** - **Examinateur**
- **Monsieur Cibert Joël** - **Professor/France** - **Directeur de thèse**
- **Monsieur Cheng Hung-Hsiang** - **Professor/Taïwan** - **Co-directeur de thèse**

Thèse préparée au sein de **l'Institut Nanosciences et Cryogénie (INAC)-CEA, l'Instutut Néel-CNRS** et **l' Ecole Doctorale de Physique**

Remerciements

Au début, je tiens à exprimer de très vifs remerciements à Matthieu Jamet, chef du laboratoire Nanostructures et Magnétisme et Joël Cibert de l'Institut Néel, mon directeur de thèse, qui m'a proposé ce sujet de thèse en cotutelle entre Université Joseph Fourier en France et la National Taiwan University à Taïwan. J'ai beaucoup appris grâce à eux à Grenoble.

Ensuite, je tiens à remercier Shinji Kuroda de l'Université Tsukuba au Japon d'avoir accepté d'être le président du jury lors de ma soutenance à Taïwan et aussi pour avoir été le rapporteur du présent manuscrit. Je remercie également les professeurs Taïwanais, Kuan-Ming Hung de la National Kaohsiung University of Applied Sciences, autre rapporteur de ma thèse et Hung-Hsiang Cheng de la National Taiwan University, mon co-directeur de thèse.

Pour l'aspect expérimental de ce travail en France, je tiens également à remercier sincèrement toutes les personnes avec qui j'ai pu collaborer: André Barski (MBE), Thibaut Devillers (MBE et TEM), Pascale Bayle-Guillemaud (TEM), Cyrille Beigné (Cryostat), Johan Rothman (Cryostat), Vincent Baltz (CPP transport), Clément Porret (MBE), Abhinav Jain (MBE and SQUID), Eric Prestat (TEM), Alain Marty (Simulation), Laurent Vila (E-beam lithography) et Tsu-Chien Weng (XAS à l'ESRF).

Un grand merci à tous mes collègues du laboratoire NM pour les bons moments passés. Les permanents: Matthieu, Cyrille, Laurent, Ariel, Alain, Jean-Philippe, Lucien, Robert et Patrick. Les thésards: Irina, Clément, Abhi, Michael, Louis, Thu Nhi, Pierre, Andrei, Piotr, Van Dai, Etienne et particulièrement Damien (tu m'as présenté ta famille: Anne-Laure, Mathieu et Gisèle qui ont été très sympathiques à mon égard. On a passé beaucoup de bonnes soirées, surtout ton mariage, et aussi de très bons moments de ski). Merci également à tous mes amis à Grenoble: Tsu-Chien (tu m'as beaucoup aidé), Chao-Yu, Woei-Fuh, Tammy, Malene, Murali, Geta, Nam, Somani, Amet.....

Enfin, je remercie ma famille: mes parents, Hsiao-Chiao et Jai-He pour leur soutien.

Contents

1 State-of-the-art **3**
1.1 Spintronics 3
1.2 Ferromagnetic semiconductors 7
1.3 Non-uniform ferromagnetic semiconductors 11
1.4 GeMn ferromagnetic semiconductor 13
1.4.1 Growth of (Ge,Mn) films 13
1.4.2 Magnetotransport of (Ge,Mn) films 15
1.5 Conclusions 19

2 Experimental methods **21**
2.1 (Ge,Mn) thin film growth 21
2.1.1 Molecular Beam Epitaxy (MBE) 21
2.1.2 Reflection High Energy Electron Diffraction (RHEED) 24
2.1.3 Spinodal decomposition 25
2.1.4 Growth of (Ge,Mn) thin films 25
2.2 Microstructure analysis 28
2.2.1 Transmission Electron Microscopy (TEM) 28
2.2.2 Secondary Ion Mass Spectrometry (SIMS) 29
2.3 Magnetic measurements 31
2.3.1 Superconducting QUantum Interference Device (SQUID) 31
2.3.2 Superparamagnetism 33
2.3.3 Magnetic phase analysis 34
2.4 Magnetotransport measurements 36
2.4.1 Sample preparation 36
2.4.2 Helium cryostat system 36
2.5 Mechanisms of magnetotransport 38
2.5.1 Hall effect 38
2.5.2 Anomalous Hall effect 39
2.5.3 Magnetoresistance 40

3 Results and discussion **45**
3.1 Ga-GeMn samples 46
3.1.1 Self-organized Mn-rich nanocolumns 46
3.1.2 Magnetic properties of Ga-GeMn 51
3.1.3 Magnetotransport of Ga-GeMn 55
3.2 As-GeMn samples 67
3.2.1 3D nano-precipitate growth 67
3.2.2 Magnetic properties of As-GeMn 71
3.2.3 Magnetotransport of As-GeMn 78
3.3 Discussion and simulation 86
3.3.1 Energy-band diagram of nanostructures and Ge matrix 86
3.3.2 Simulation of magnetotransport 88

4 Conclusions and outlooks **93**

Introduction

Spintronics, combining electron and spin, is a new branch of electronics. As microelectronics is well developed today, researchers say that chipmakers in the coming years will likely hit a barrier in Moore's Law. Spintronics provides a solution to prevent chip designers from gaining performance by shrinking their chips and holds promise in minimizing power consumption for next-generation consumer electronics. The starting point was the discovery of giant magnetoresistance (GMR) effects twenty years ago, by Albert Fert and Peter Grunberg. Initially a subject of fundamental research, and thanks to improvements in the nanofabrication technology, spintronics rapidly lead to novel applications which are incorporated in today's computers.

The simplest method of generating a spin-polarized current in a metal is to pass the current through a ferromagnetic material. Today, in metal-based spintronic devices, the most common application of this effect is a GMR device such as magnetic sensor, hard disk drive and MRAM. In order to extend their applications, semiconductor-based spintronic devices are developing and will hopefully emerge for next-generation electrical and optical devices. Ferromagnetic semiconductors are important candidates for spin injection into semiconductors. Group IV ferromagnetic semiconductors have a high potential due to their compatibility with the mainstream Si technology. Besides, a combination with III-V compound semiconductors would extend their potential to optical and optoelectronics applications.

In this thesis, we have grown (Ge,Mn) ferromagnetic semiconductors on insulating GaAs(001) substrates. It was shown previously that (Ge,Mn) layers grown on germanium substrates are highly inhomogeneous (they contain Mn-rich nanocolumns) and display interesting magnetic and magnetotransport properties: room temperature ferromagnetism, strong anomalous Hall effect and magnetoresistance. Our initial motivation was to investigate more easily these magnetotransport properties. Actually, we have found that the diffusion or segregation of gallium and arsenic from the substrate, and the

morphology of the growing surface, deeply alter the growth mode and the magnetotransport properties, so that we learned a lot about various mechanisms of growth and magnetotransport.

Here is the organization of this manuscript.

- **Chapter 1** *State-of-the-art*: Spintronics and its applications are introduced. Then, the needs and limitations of ferromagnetic semiconductors are reported. Finally, we mention the recent development of (Ge,Mn) ferromagnetic semiconductor.

- **Chapter 2** *Experimental methods*: This chapter presents the experimental techniques used to realize this thesis, such as Molecular Beam Epitaxy for (Ge,Mn) thin film growth, *in-situ* Reflection High-Energy Electron Diffraction to monitor the surface morphology and crystal structure of substrates and thin films. The microstructure and chemical composition of (Ge,Mn) films were investigated using Transmission Electron Microscopy, and Secondary Ion Mass Spectrometry, respectively. Magnetic measurements are performed using a Superconducting Quantum Interference Device (SQUID) magnetometer. (Ge,Mn) films were processed by optical lithography into double Hall-cross bars in order to perform magnetotransport measurements in a Helium cryostat setup. Finally, the basic magnetotransport mechanisms will be introduced at the end of this chapter.

- **Chapter 3** *Results and discussion*: In the main chapter of this thesis, by using two different GaAs(001) wafers, we report that surface morphology and chemical species on the surface of the GaAs substrates change the growth mechanisms of our (Ge,Mn) films, which induces different types of nanostructures in these films. These different nanostructures exhibit different magnetic and magnetotransport properties. First, we introduce the results of *Ga-GeMn* films grown with *epiready* GaAs(001) substrates. Then, *As-GeMn* films grown with amorphous Arsenic capped GaAs(001) substrates are discussed. Finally, a simulating tool is employed to calculate the magnetotransport properties, and the results are compared to our experimental results.

- **Chapter 4** *Conclusions and outlooks*: We summarize the conclusions about the two groups of (Ge,Mn) films and their spin-dependent transport properties.

Chapter 1

State-of-the-art

In this chapter, we introduce spintronics and its applications. Then, the needs and limitations of ferromagnetic semiconductors are reported. Finally, we mention the recent development of (Ge,Mn) ferromagnetic semiconductor.

1.1 Spintronics

Spintronics is a rapidly emerging field of science and technology that will most likely have a significant impact on the future of all aspects of electronics as we continue to move into the 21th century. Conventional electronics is based on the charge of the electron. Attempts to use another degree of freedom of an electron, its *spin*, have given rise to a new, rapidly evolving field, known as spintronics[1] or magnetoelectronics[2]. The basic theory for spintronics is almost as old as the concept of electron spin itself. In the mid-thirties, Mott postulated[3] two spin channel model, that certain electrical transport anomalies in the behavior of the metallic ferromagnets arose from the ability to consider the spin-up and spin-down conduction electrons as two independent families of charge carriers, each with its own distinct transport properties.

For the experiments on spin-dependent electron transport phenomena in solid-state devices, the origins can be traced back to 1970s the ferromagnet/superconductor tunneling experiments pioneered by Meservey and Tedrow[4] and initial experiments on magnetic tunnel junctions (MTJs) by Julliere[5]. The Tunnel magnetoresistance (TMR) is a magnetoresistive effect that occurs in magnetic tunnel junctions. This is a component consisting of two ferromagnets separated by a thin insulator in figure 1.1. If the insulating layer is thin enough (typically a few nanometers), electrons can tunnel from

one ferromagnet into the other. Since this process is forbidden in classical physics, the tunnel magnetoresistance is a strictly quantum mechanical phenomenon. Meanwhile, due to the development of nano-fabricating technologies, TMR has lead to the emergence of Magnetic Random Access Memory (MRAM) and reprogrammable magnetic logic devices. This spintronic based MRAMs should rival the speed and rewritability of conventional RAM and retain their state (and thus memory) even when the power is turned off (non-volatile property).

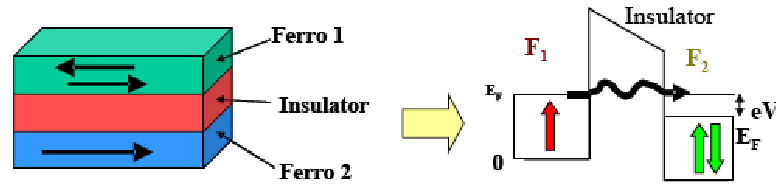

Figure 1.1: Illustration of Julliere's model of TMR in MTJ.

More than twenty years ago, spintronics made a big step due to the observation of spin-polarized electron injection from a ferromagnetic metal to a normal metal by Johnson and Silsbee (1985)[6] and the discovery of giant magnetoresistance (GMR) effect independently by the group of Albert Fert[7] and the one of Peter Grunberg[8], whom 2007 Nobel Prize in physics are awarded to. As Figure 1.2 shows, this effect is observed as a significant change in the electrical resistance depending on whether the magnetization of adjacent ferromagnetic layers are in a parallel or an antiparallel alignment. The overall resistance is relatively low for parallel alignment and relatively high for antiparallel alignment. For the applications of GMR effect, it has been used extensively in the read heads of modern hard disk drives and magnetic sensors. A hard disk storing binary information can use the difference in resistance between parallel and antiparallel layer alignments as a method of storing 1s and 0s. A high GMR is preferred for optimal data storage density. Current perpendicular-to-plane (CPP) spin valve GMR currently yields the highest GMR. Research continues with older current-in-plane (CIP) configuration and also in TMR spin valves which enable disk drive densities exceeding 1 Terabyte per square inch.

For extending the applications of spintronics to microelectronics, researchers are interested in the integration of magnetic materials and semiconductors. The first use of semiconductors for spintronics can be traced back at least

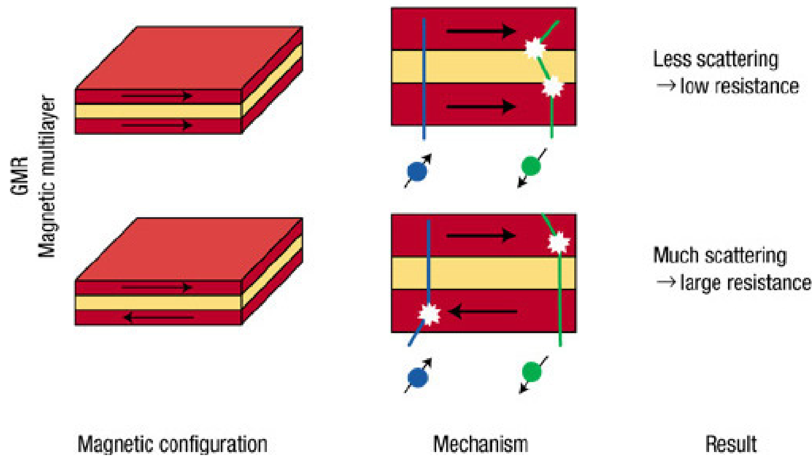

Figure 1.2: The operational principle of GMR[11].

as far as the theoretical proposal of a spin field-effect-transistor (Spin-FET) by Datta and Das in 1990[9]. Figure 1.3 shows the Spin-FET with a narrow semiconductor channel between two electrodes named the source and the drain. There is gate electrode, which is above the channel, to be applied a voltage such as a traditional FET. This Spin-FET has a ferromagnetic source and drain so that the current flowing into the channel is spin-polarized. When a voltage is applied to the gate, the spins rotate due to the Rashba effect as they pass through the channel and the drain rejects these antialigned electrons. A Spin-FET would have several advantages over a conventional FET. Flipping an electron's spin takes much less energy and can be done much faster than pushing an electron out of the channel. One can also imagine changing the orientation of the source or drain with a magnetic field, introducing an additional type of control that is not possible with a conventional one *i.e.* logic gates whose functions can be changed on the fly. However, the low injection efficiency of spin-polarized current from ferromagnetic metal to semiconductor limits its applications in spintronics because of the large conductivity mismatch between the metallic ferromegnet and the semiconductor[10]. Thus, spin injection into semiconductors is an important topic for researchers.

One of the methods to increase the injection efficiencies of spin-polarized current into a semiconductor is using ferromagnetic or paramagnetic semiconductors, which attract a lot of attention in this field. For example, spintronics in an optical device as shown in figure 1.4, a spin Light-Emitting Diode (Spin-LED) is realized by a paramagnetic semiconductor ($Be_xMn_yZn_{1-x-y}$)

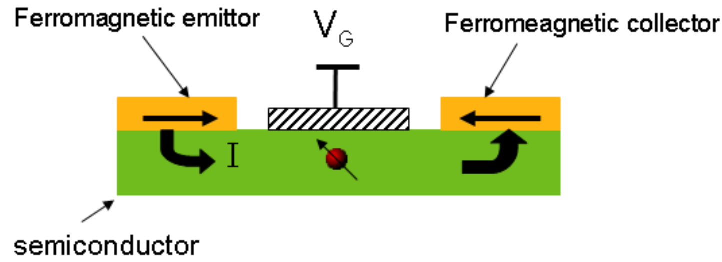

Figure 1.3: Spin field-effect-transistor of Datta and Das.

as a spin aligner integrated with GaAs/AlGaAs LED[12]. Very large degree of spin-polarization is achieved in this device, although it is limited to low working temperatures. Besides, another work was conducted by the group of H. Ohno on the spin polarization of holes injected in a GaAs-based spin-LED from GaMnAs, spin polarization was close to 85%[13].

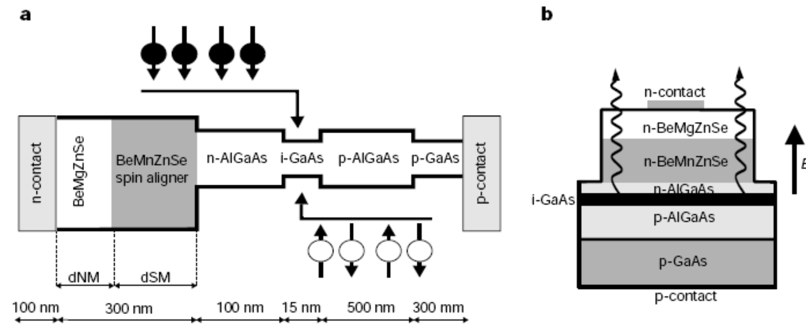

Figure 1.4: (a) Schematic band structure of the spin-aligner light-emitting diode. Spin-polarized electrons are injected from the left into the active GaAs layer, unpolarized holes from the right, (b) Side view of the device showing the direction of the magnetic field and the emitted light[12].

1.2 Ferromagnetic semiconductors

Ferromagnetic semiconductors are semiconductor materials that exhibit both ferromagnetism and semiconductor properties. Recently, this field of semiconductor spintronics has been developed, which is concerned with ways to control the spin degree of freedom of electrons in semiconductor. As magnetic semiconductors are used in electronic devices, these materials could provide a new type of control of conduction; not only traditional electronics are based on control of charge carriers (n- or p-type), but also practical magnetic semiconductors would allow control of quantum spin state (spin-up or spin-down). This would theoretically provide near-total spin polarization, which is an important property for spintronics applications. The classification of magnetic semiconductors is shown as follows:

- *CMS*: In the late 1960s and 1970s, concentrated magnetic semiconductors (CMS) that have a periodic array of magnetic element in crystal lattice (see figure 1.5(A)) were extensively studied such as europium chalcogenides and semiconducting spinels. Exchange interactions between the electrons in the semiconducting band and the localized electrons at the magnetic ions lead to a number of interesting properties. Unfortunately, the crystal structure of such magnetic semiconductors is quite different from that of Si and GaAs, which limits their potential for applications.

- *DMS*: As the same method of doping semiconductors with impurities to change their properties (n-type or p-type), magnetic elements are introduced into non-magnetic semiconductors to make them magnetic. This category of semiconductors, called diluted magnetic semiconductors (DMSs; figure 1.5(B)), are alloys of nonmagnetic semiconductor (figure 1.5(C)) and magnetic elements[14].

In the beginning, most of the work in making semiconductors ferromagnetic has focused on II-VI-based compound semiconductors such as CdTe or ZnSe which were doped with magnetic ions (such as manganese) to introduce localized spin $S = 5/2$ in the matrix and result in a diluted magnetic semiconductor (DMS), but without modifying the carrier density. However, their Curie temperatures are not sufficient high for technological applications, and they are not metallic[15]. In the 1990s, DMSs of III-V-based compound semiconductors were successfully fabricated by introducing Mn ions, but Mn atoms are much less soluble than in II-VI semiconductors making them much more difficult to dilute into a semiconductor a semiconductor

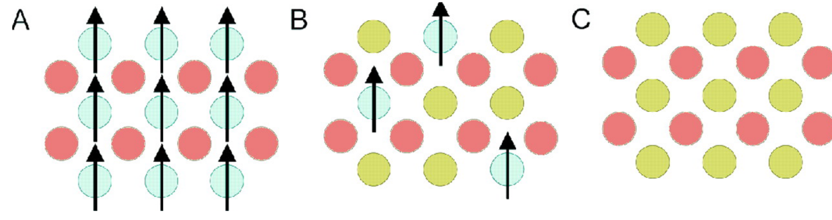

Figure 1.5: Three types of semiconductors: (A) a magnetic semiconductor, in which a periodic array of magnetic element is present; (B) a diluted magnetic semiconductor, an alloy between nonmagnetic semiconductor and magnetic semiconductor; and (C) a nonmagnetic semiconductor, which contains no magnetic ions[14].

such (GaMn)As. By using a low temperature MBE technique, it is possible to grow crystals with higher Mn concentration in a non-equilibrium state and prevent Mn ions from precipitations. T_C achieved at that time was 110K for 5.5% Mn-doped GaAs[41]. The experiment and theory of (GaMn)As are successfully developed[14],[18]. The theoretical prediction of T_C for different DMSs is shown as figure 1.6 by Zener model. Now, the highest T_C of (GaMn)As is 173K, which was achieved by the group of Gallagher and Campion in UK[17]. Theoretically, wide band gap DMSs such as (GaMn)N, (GaCr)N and (ZnCo)O are proposed as good candidates for high T_C material. However, up to now, the modest T_C of DMSs from the experimental results still limits their applications in spintronics. Scientists keep trying many fabrication techniques and different materials to increase T_C up to room temperature for future applications.

For the application of magnetic semiconductor, electric field inducing ferromagnetism is another interesting topic, and the ability to externally control the properties of magnetic materials would be highly desirable from fundamental and technological viewpoints. For example in the case of (InMn)As reported by Ohno's group[25], they applied an electric field as the method in semiconductors in figure 1.7(a) *i.e.* using an insulating-gate field-effect transistor structure, and ferromagnetism in the thin film of magnetic semiconductor can be controlled. At $V_G < 0$, hole carriers accumulate in the channel layer and make the hysteresis loop lager as shown in figure 1.7(b).

So far, the classification CMS or DMS can not describe all the magnetic semiconductors. In fact, during the magnetic semiconductor growth, the DMS matrix with the coherent segregation is observed in some magnetic semiconductors. In this non-uniform magnetic semiconductor, mag-

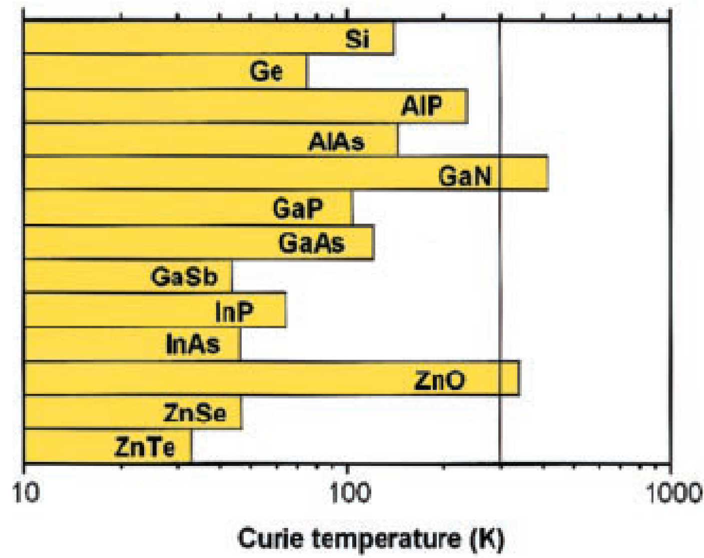

Figure 1.6: Computed value of the Curie temperature T_C by Zener's model for various p-type semiconductors containing 5%Mn and 3.5×10^{20} holes at different temperatures.[18].

netic properties attribute to their separative phases with higher T_C, which is neither DMS nor CMS, and these non-uniform ferromagnetic semiconductors with high Curie temperature will be discussed in next section.

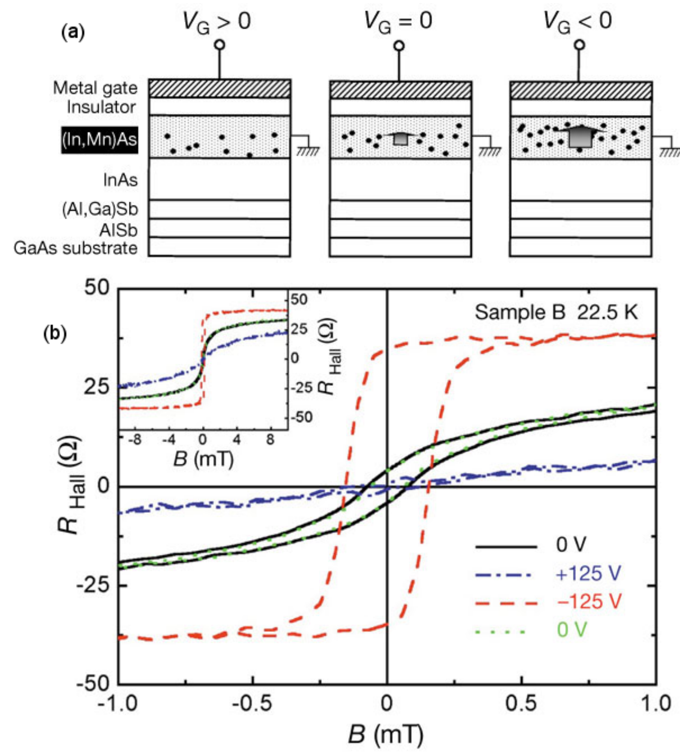

Figure 1.7: (a) Cross-section of a metal-insulator-semiconductor structure under different gate biases V_G. (b) R_{Hall} versus field curves under different gate biases at temperature 22.5K shows field-effect control of the hole-induced ferromagnetism in magnetic semiconductor (In,Mn)As[25].

1.3 Non-uniform ferromagnetic semiconductors

In order to have a higher T_C magnetic semiconductors for the applications in spintronics, Non-uniform ferromagnetic semiconductors and diluted magnetic oxides (DMO) may provide a solution[66]. Here, we discuss the Non-uniform ferromagnetic semiconductor from the recent experimental results and theoretical predictions.

In general, some DMS systems exhibit a solubility gap and show phase separation in thermal equilibrium. As is known in alloy physics, in the quenching process for such systems spinodal decomposition occurs *i.e.*, local density fluctuations are amplified and finally lead to random patterns of high concentration regions which connect each other. This spinodal decomposition (2D or 3D) leads to the formation metal rich nanostructures exhibiting higher T_C than the DMS films. It has been reported in (Ge,Mn) films[19],[20],[21], in Cr and Fe-doped GaN[22],[23] or ZeTe[24].

Non-uniform ferromagnetic semiconductors such as (Ga,Mn)As and (Ga,Mn)N are theoretically predicted by Sato *et al*[26] in figure 1.8. They proposed that spinodal decomposition phase in DMS offers the possibility to have high Curie temperature even if the magnetic exchange interaction is short ranged by Monte Carlo method.

In Non-uniform ferromagnetic semiconductor systems, when the concentration of magnetic impurities exceeds the solubility limit, a variety of magnetic nanocrystals embedded coherently into the semiconductor are formed in a self organized manner. According to the present insight, these nanocrystals containing a high density of magnetic constituent account for the persistence of ferromagnetic features up to high temperatures. The shape and dimension and, thus, the blocking temperature of the nanocrystals can be controlled by codoping with shallow dopants and through growth conditions. Functionalities of these multicomponent systems are described together with prospect for their applications in spintronics, nanoelectronics, photonics, plasmonics , and thermoelectrics[66].

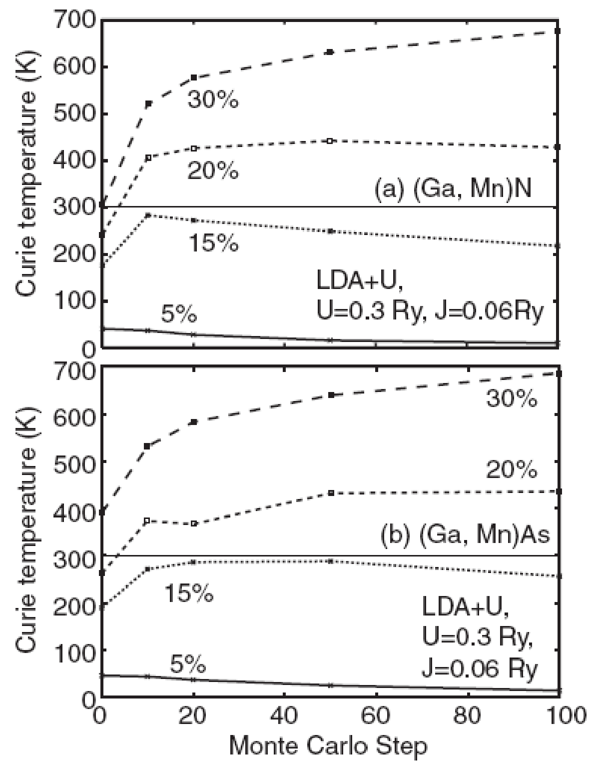

Figure 1.8: (a) (Ga,Mn)N and (b) (Ga,Mn)As as a function of the number of Monte Carlo steps. Curie temperatures are calculated with corrected parameter J (effective magnetic exchange interaction) by LDA+U[26].

1.4 GeMn ferromagnetic semiconductor

Group-IV magnetic semiconductors with Mn doping, such as SiMn, GeMn and SiGeMn, have high potential for the applications in spintronics due to:

- Compatibility with mainstream silicon technology.
- Mn magnetic impurity as an acceptor at substitutional site in the crystal lattice.
- Very long spin relaxation time which comes from weak spin-orbital coupling in Si and Ge[28].

Here, we focus on the study of GeMn magnetic semiconductor. Recently, some groups have grown Mn-doped Ge films by using different growth techniques such as Mn implantation, low temperature MBE and chemical vapor deposition (CVD). Since 2002, the first experimental results are reported by the group of B. T. Jonker in USA[29]. As figure 1.9 shows, they grew $Ge_{1-x}Mn_x$ films ($0.006<x<0.035$) by low temperature MBE with Curie temperature from 25 to 116 K, which is linear with Mn concentration. Anomalous Hall effect was observed, which could be modulated by applying a gate voltage, and the magnetic moment corresponded to 1.4 - 1.9 Bohr magnetons (μ_B)/Mn. Despite the low growth temperature, Mn diffusion/phase separation resulted in small precipitates of 2 to 6 nm in diameter with a Mn concentration higher than that of the surrounding matrix. Their T_C is larger than the one of theoretical prediction by Zener model[18]. This might be due to their non-uniformity as mentioned in previous section.

1.4.1 Growth of (Ge,Mn) films

From the phase diagram of Ge and Mn binary alloy in figure 1.10, we can understand the limitation of GeMn DMS growth because of the very low solubility of Mn in Ge matrix. Several stable and metallic phases form in equilibrium growth such as $GeMn_{3.4}$, Ge_2Mn_5, Ge_3Mn_7, $GeMn_2$, Ge_3Mn_5 and Ge_8Mn_{11}. Last two phases are ferromagnetic and identified in the non-uniformity (Ge,Mn) films. In some cases especially for high temperature growth or annealing after growth, parasitical metallic nanoclusters of Ge_3Mn_5 in (Ge,Mn) films, which is the most stable GeMn alloy and ferromagnetic up to 300 K, are formed[33],[34],[35]. Another stable precipitate Ge_8Mn_{11} with Curie temperature around 300°C is also reported by Park *et al*[36].

Some reviews of experimental results on (Ge,Mn) growth are listed below:

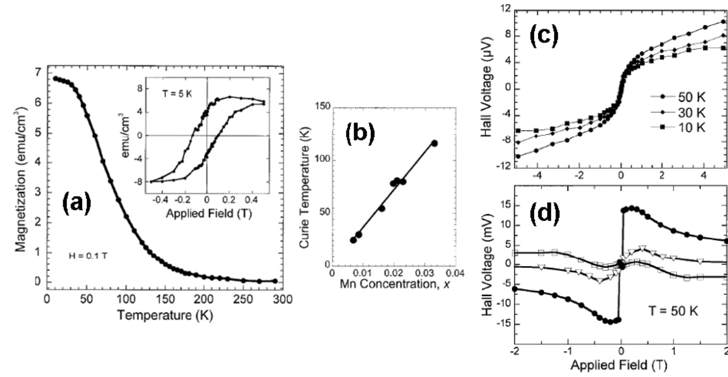

Figure 1.9: (a) Temperature dependence of the magnetization for $Ge_{0.98}Mn_{0.02}$ (b) T_C of (Ge,Mn) films as a function of Mn concentration (c) Anomalous Hall effect for $Ge_{0.977}Mn_{0.023}$ (d) Modulation of AHE by gate voltage at 50K[29].

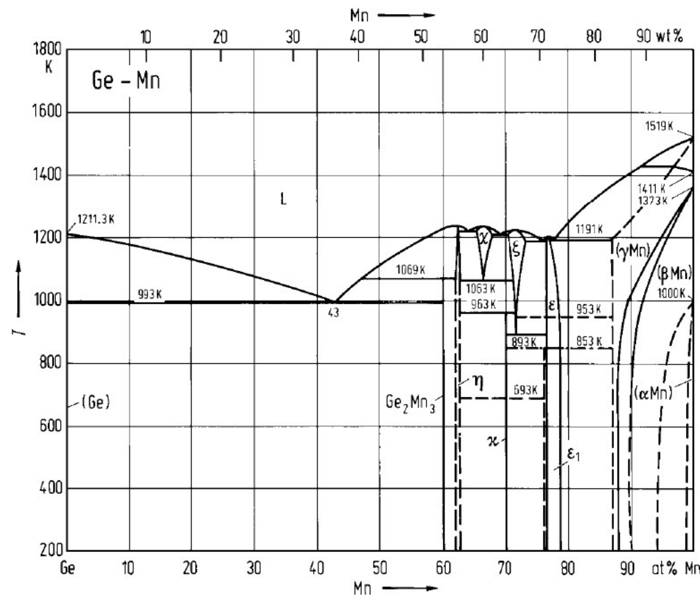

Figure 1.10: Phase diagram of GeMn binary system[30].

- Ottaviano *et al* realized Mn implantation in Ge[37]. The crystal structure of Ge was disorder after implantation. The Ge_3Mn_5 was observed after annealing in figure 1.11(a).

- Kang *et al* studied chemical distribution of non-uniform (Ge,Mn) bulk in figure 1.11(b) and its local electronic structure. They suggested that the observed ferromagnetism in (Ge,Mn) arises from the Mn-rich phase which is Ge_8Mn_{11}[38].

- Bougeard *et al* observed the nanometer-sized clusters which are areas with increased Mn content on substitutional lattice sites compared to the host matrix by low temperature MBE[39]. For higher growth temperature, Ge_3Mn_5 formed in (Ge,Mn) film as shown in figure 1.11(c).

- Inhomogeneous (Ge,Mn) films are evidenced with self-assembled Mn rich nanostructures (nanocolumns) by low temperature MBE as shown in figure 1.12 by Jamet *et al.* This nano-scale spinodal decomposition phase in DMS makes T_C higher than room temperature[21]. This nanostructure is also observed by Li *et al*[19].

- Room-temperature ferromagnetism in $Ge_{1-x}Mn_x$ nanowires are also observed by Kazakova *et al* who used the supercritical fluid inclusion-phase technique to synthesize within the pores of anodized aluminum oxide membranes[31].

- Another $Ge_{1-x}Mn_x$ nanowires with 20 μm in length and 60 nm in diameter using the thermal vapor transport method were synthesized by Cho *et al.* The magnetic hysteresis conformed the room-temperature ferromagnetism of $Ge_{1-x}Mn_x$ nanowires, which is maximized at x = 0.1. They found Mn substitution is more effective to form significant ferromagnetic Ge nanowires, compared to the Co or Fe substitution[32].

1.4.2 Magnetotransport of (Ge,Mn) films

Magnetotransport properties including magnetoresistance (MR) and Hall effect are attributed to the interplay between cooperative phenomena and carrier transport[80]. Such as the study of p-type (Ga,Mn)As DMS, the p-d exchange between holes and Mn $3d$ spins was determined from these measurements by Matsukura *et al* who demonstrated that ferromagnetism of (Ga,Mn)As has its origin in the Ruderman-Kittel-Kasuya-Yosida (RKKY) interaction mediated by holes[41]. For the development of (Ge,Mn) film growth, some studies of magnetotransport properties on (Ge,Mn) have been carried out as follows:

- B. T. Jonker *et al* reported MR measurements on nanoscale Ge_8Mn_{11} ferromagnetic clusters embedded in (Ge,Mn) DMS matrix, which change from negative (≈6%) below ≈22 K to positive(≈60%)[36]. They also observed Anomalous Hall effect[29], which could be modulated by applying a gate voltage in figure 1.9(d).

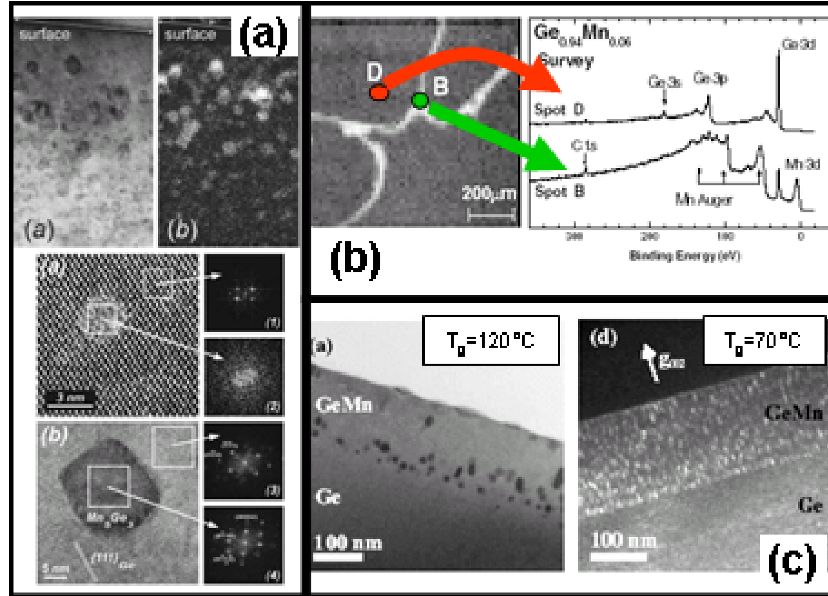

Figure 1.11: (a) Images of Transmission Electron Microscopy (TEM) show the result of Mn implantation in Ge crystal[37]. Before annealing, amorphous precipitates are observed; after annealing, Ge_3Mn_5 inclusion appears (b) Scanning photoelectron microscopy (SPEM) studied the chemical composition. The bright spot is Mn-rich regime made of Ge_8Mn_{11} phase[38]. (c) TEM images show $Ge_{0.95}Mn_{0.05}$ by MBE growth at 120°C and 70°C. For 120°C, the film contents Ge_3Mn_5 clusters and for 70°C, precipitates are coherently bound to the surrounding[39].

- Tsui *et al* studied the growth, magnetic and magnetotransport properties of Co and Mn-doped Ge magnetic semiconductors with high doping concentration ($Co_{0.12}Mn_{0.03}Ge_{0.85}$). Very high T_C(≈270 K), large positive MR and AHE are observed[42].

- Jamet *et al* realized high T_C (Ge,Mn) films with ferromagnetic Mn-rich nanocolumns on Ge(001) wafer, which has a giant positive MR in figure 1.12(c) and strong AHE up to room temperature in figure 1.12(d).

- Li *et al*[19] also reported a giant positive MR that correlates directly with the distribution of magnetic impurities (see figure 1.13(a)). Moreover, annealing at 200°C increases Mn substitution in the host matrix above the threshold for the insulator-metal transition and results in global ferromagnetism with conventional negative MR in figure 1.13(b).

- Deng *et al*[43] performed that the electrical transport of (Ge,Mn) films obey Efros variable range hopping law in the low temperature range.

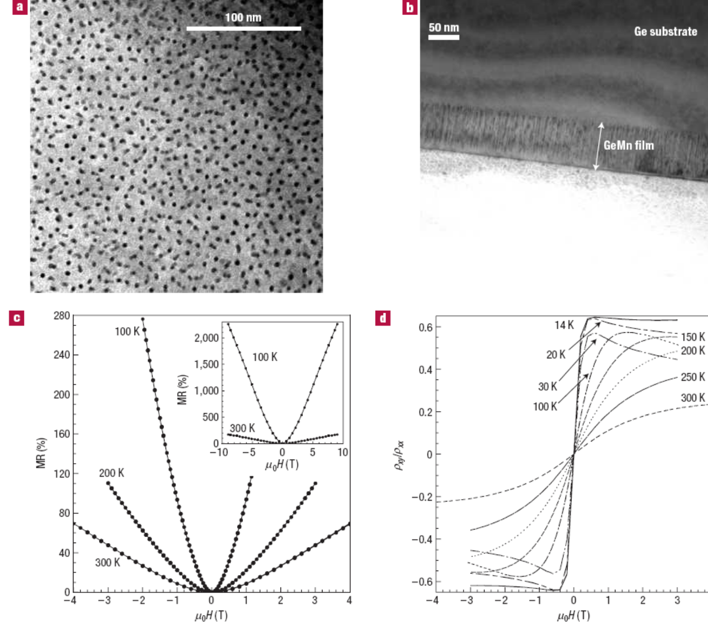

Figure 1.12: Transmission electron microscopy observations (a) Low-magnitude plane view of nanocolumns. (b) Low-magnitude cross-sectional image of the 80 nm (Ge,Mn) layer, the nanocolumns are perpendicular to the film plane and appear as dark line[21]. (c) High-Temperature MR with the magnetic field applied perpendicular to the film. Inset: high field dependence of the MR at 100 and 300 K. (d) Hall angle ρ_{xy}/ρ_{xx} versus magnetic field recorded at different temperature shows strong AHE[21].

A negative coefficient of the ordinary Hall effect of p-type carriers was found in the variable range hopping at low temperature. AHE was observed in $Ge_{0.949}Mn_{0.051}$ grown on Ge(001) below Curie temperature, indicating the carrier-mediated intrinsic ferromagnetism (see figure 1.13(c)).

- The transport properties of $Ge_{0.92}Mn_{0.08}$ grown on GaAs(001), highly dependent on the substrate temperature and the interdiffusion of impurities at the interface, were studied by Uchitomi *et al*[44].
- Riss *et al*[45] reported on the temperature- and field-driven metal-insulator transition in diluted (Ge,Mn) magnetic semiconductors accompanied by magnetic ordering, MR (see figure 1.13(d)) reaching thousands of percents, and suppression the AHE (see figure 1.13(e)) by a magnetic field up to 33.3 T. They argued that the strong magnetic disorder leads to localization of charge carriers and is the origin

of the unusual properties of (Ge,Mn) alloys.

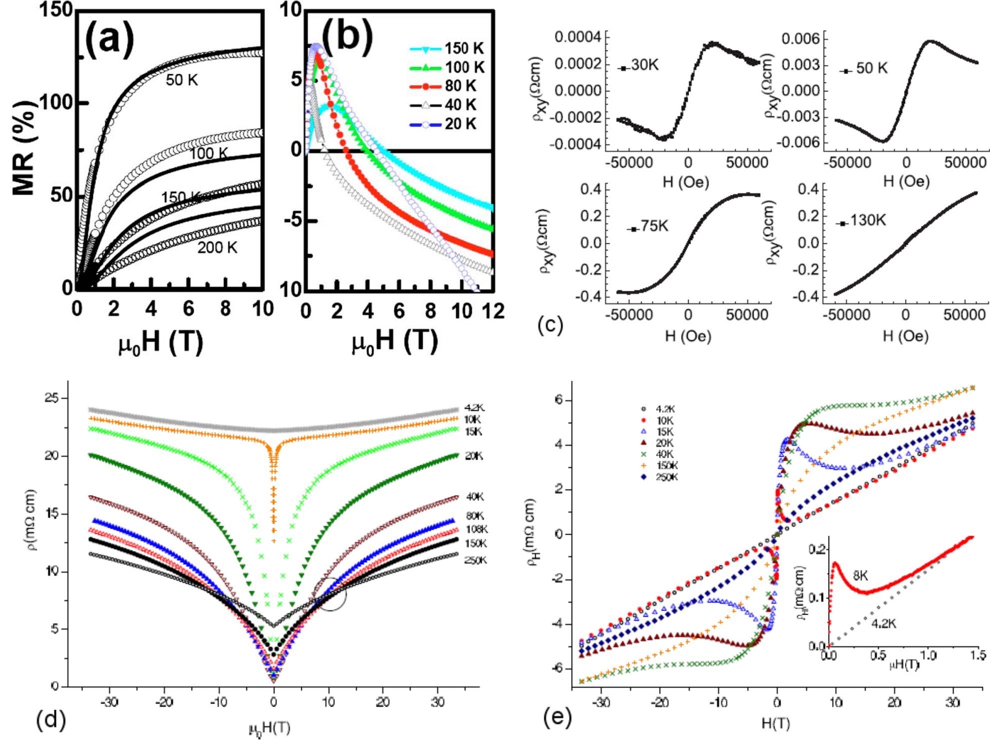

Figure 1.13: (a) Giant MR of as-grown $Ge_{0.95}Mn_{0.05}$ (b) MR of postannealed $Ge_{0.95}Mn_{0.05}$[19] (c) The magnetic field dependence of Hall resistivity of $Ge_{0.949}Mn_{0.051}$ at different temperature[43] (d) MR of 2%Mn samples as a function of magnetic field up to 33.3 T at different temperatures. The cross-over region between the metallic-like and insulating phase is indicated by the circle[45] (e) Hall resistivity measured in the 2%Mn samples at different temperatures. Inset: zoon of the 4.2 K and 8 K data at low field[45].

1.5 Conclusions

Spintronics is a technique with fast track from the discovery of GMR and MTJ materials to the incorporation of these materials in commercial devices. Recently, spin-dependent transport in semiconductor is a starling activity and rapidly developing for the integration of spin-electronic devices into the traditional semiconductor technology. Ferromagnetic semiconductors with high T_C are desired strongly for spin injection into semiconductors. (Ge,Mn) ferromagnetic semiconductor is a potential candidate for the applications in spintronics.

Chapter 2

Experimental methods

This chapter presents the experimental techniques used to realize this thesis, such as Molecular Beam Epitaxy (MBE) system for (Ge,Mn) thin film growth, *in-situ* Reflection High-Energy Electron Diffraction (RHEED) to monitor the surface morphology and crystal structure of substrates and thin films. The microstructure and chemical composition of (Ge,Mn) films are investigated using Transmission Electron Microscopy (TEM), and Secondary Ion Mass Spectrometry (SIMS) respectively. Magnetic measurements are performed using Superconducting QUantum Interference Device (SQUID) magnetometry. (Ge,Mn) films are processed by optical lithography in double Hall-cross bars to allow magnetotransport measurements in a Helium cryostat setup. Finally, the basic magnetotransport theory will be shortly introduced at the end of this chapter.

2.1 (Ge,Mn) thin film growth

For the growth of (Ge,Mn) thin films, we have used low-temperature Molecular Beam Epitaxy. In this section, I start with the description of MBE, its *in-situ* RHEED tool, the mechanism of spinodal decomposition and the growth conditions we used to grow (Ge,Mn) thin films.

2.1.1 Molecular Beam Epitaxy (MBE)

Molecular Beam Epitaxy (MBE) is one of the methods for single crystal growth, invented in the late 1960s at Bell Laboratories by J. R. Arthur and Alfred Y. Cho[46]. It is an Ultra-High-Vacuum (UHV) technique for producing high quality epitaxial structures with a control of atoms at the monolayer scale.

The principle of MBE growth consists essentially in a flux of atoms or clusters of atoms, which are produced by heating up a solid source. In UHV conditions, these atoms have very long mean free path between collisions (longer than the chamber dimension). They adsorb onto a substrate surface with a well defined temperature, where they can diffuse and incorporate into a growing thin film or other nanostructures.

A schematic drawing of a general MBE machine is shown in figure 2.1, and some basic components are included:

- The *vacuum system* consists in a stainless steel growth chamber, connected to a preparation chamber and a load-lock module for transfer to or from the air. All the growth components must be able to resist bake-out temperatures up to 200°C for a long period of time, which is necessary to minimize out-gassing from the chamber wall to keep the UHV conditions.

- The *pumping system* must be able to sustain base pressures down to the 10^{-11} to 10^{-12} Torr range and usually consists of ion pumps, cryogenic pumps, turbo pumps and mechanical pumps.

- *Liquid N_2 cryopanels* surround the growth chamber to prevent re-evaporation from other than the hot cells, to provide the thermal isolation from cell to cell and to pump the residual gas.

- *Effusion cells* are the important components of a MBE system, because they must provide excellent flux stability, uniformity, and material purity.

- *Substrate manipulator* is used to rotate the sample and control the growth temperature. On the manipulator, substrate holders made of molybdenum are mounted on the manipulator. Wafers are glued by indium on the holder before sample growth.

- Some *analysis tools* are available in MBE systems. For example, Reflection High Energy Electron Diffraction (RHEED) is employed to check the sample surface at grazing incidence (a few degrees) by high voltage electron beam (up to 20 keV in our system). A Residual Gas Analyzer (RGA) is an essential component to check the possibility of air leak, to measure the system cleanliness and to detect residual gases and their origin. Besides, Auger Electron Spectroscopy (AES) is present in our system and used to analyze the surface composition of the films.

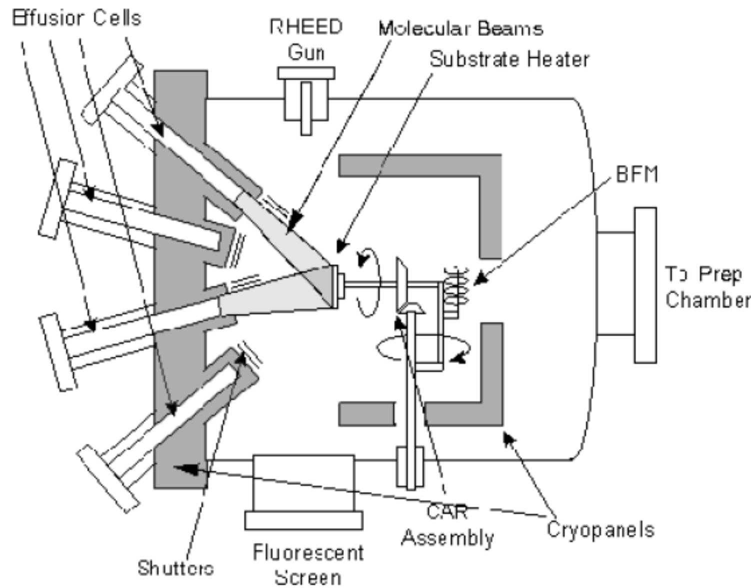

Figure 2.1: Diagram of a typical MBE system growth chamber.

The crystal growth mechanisms on the sample surface by MBE include the adsorption of atoms, the atom diffusion on the surface, nucleation of phases and desorption, which mainly depend on the growth temperature of the surface. At higher growth temperature, the atoms have more energy for diffusion on the surface and higher possibility for the growth of new phases. Desorption of atoms from the growth surface occurs at much higher temperature than our growth temperature. However, when the growth temperature is too low, atoms do not have enough energy for diffusion, there could be a polycrystal growth or amorphous growth. Therefore, to well control the growth mechanisms of thin films by MBE, the growth temperature (T_g) is a key parameter. In our case, we grow (Ge,Mn) films at low temperature to favor the growth of metastable phases. Under these conditions, as discussed later, we observed a spinodal decomposition[47].

In the present work we used a RIBER 2300 system[1]. The growth temperature was thoroughly calibrated and then adjusted from the heating current during subsequent runs: we think we obtained a reasonable reproducibility from sample to sample, but we must stress however that measuring such

[1]Collaboration with André Barski, Thibaut Devillers, Clement Porret and Abhinav Jain in CEA/INAC/SP2M/SiNaPS

low temperatures in a UHV environment is a difficult task and our values of the growth temperatures should not be compared without care with those reported by other groups.

2.1.2 Reflection High Energy Electron Diffraction (RHEED)

RHEED is a technique used to characterize the surface of crystalline materials, which is particularly employed in a MBE system. A high energy beam (3 - 100 keV, 20 keV in our case) is directed towards the sample surface at a grazing angle of incidence. The electrons are diffracted by the crystal structure of the sample and then impinge on a phosphor screen mounted opposite to the electron gun, as shown in figure 2.2. Most often, the resulting pattern on the screen is a series of streaks. The distance between the streaks is an indication of the surface lattice unit cell size. The grazing incidence angle ensures surface specificity despite the high energy of the incident electrons, hence the streaky pattern observed if the surface is atomically flat. If the surface has a rougher surface, the RHEED pattern becomes spotty.

Meanwhile a layer-by-layer growth mode can lead to oscillations of the RHEED pattern , which can be used to follow the conditions of epitaxy growth and the growth rate in monolayer per second (*e.g.*, the case of Ga, As molecular beams on GaAs(001) surface)[48].

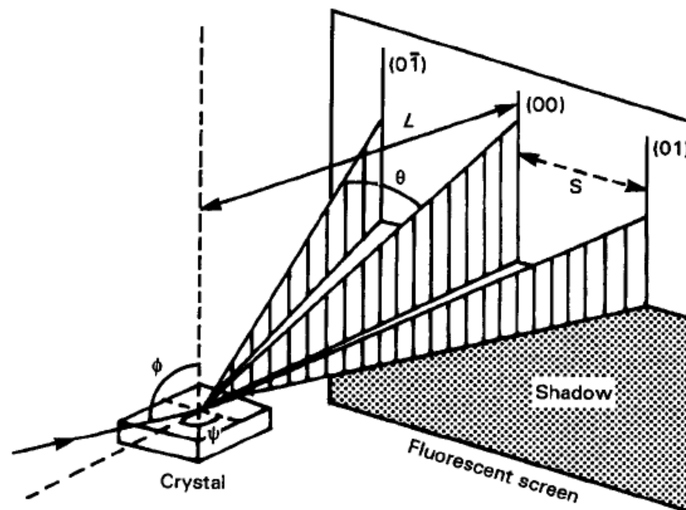

Figure 2.2: A schematic diagram of the RHEED experiment.

2.1.3 Spinodal decomposition

Spinodal decomposition is a mechanism by which a solution of two or more components can separate into distinct regions with distinctly different chemical compositions (and possibly different physical properties). In order to understand spinodal decomposition, we can make use of the binary phase diagram and the Gibbs free energy curve such as in figure 2.3. In this binary system with element A and B, c is the concentration of B in the alloy. The spinodal decomposition mechanism takes place when the Gibbs free energy of mixing has a region of negative curvature. Then the free energy is minimized if nucleation and growth take place in the two neighbouring regions, where the curvature is positive.

To be more precise, for a composition of the alloy in the spinodal decomposition region, the free energy change is negative for an arbitrarily small fluctuation in composition; *i.e.* it occurs spontaneously, such that one part of the system gets more concentrated at the expense of another. The system is inherently unstable and phase separation occurs. In contrast, an average composition within the two-phase region, but outside of the spinodal curves requires large composition fluctuations to decrease its energy.

From a more practical standpoint, spinodal decomposition provides a means of producing a very finely dispersed microstructure that can significantly enhance the physical properties of the material[49].

Finally, we should mention that the term spinodal decomposition is used when a mere change of composition is observed. In the case of (Ge,Mn), more recent studies show that two different structures are involved in the Mn-rich and Mn-poor regions.

2.1.4 Growth of (Ge,Mn) thin films

For our samples, (Ge,Mn) thin films were grown on semi-insulating GaAs(001) substrates ($\rho > 10^7 \Omega$.cm) by low temperature Molecular Beam Epitaxy (LT-MBE). Ge and Mn atoms are co-evaporated onto GaAs substrates from Knudsen cells in ultra-high-vacuum conditions ($p \approx 10^{-11}$ mbar) at a low substrate temperature, T_g from 90°C to 120°C, and the deposition rate of (Ge,Mn) is approximately to 0.2Å/sec[21]. Average Mn concentration is from 2% to 10%, and controlled by adjusting the temperature of the Mn Knudsen cell.

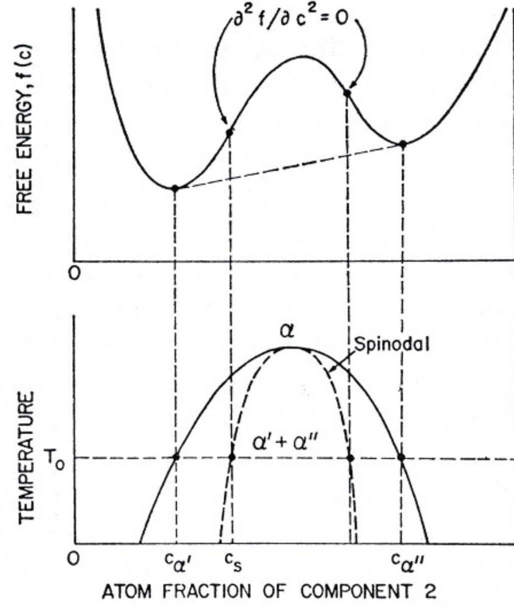

Figure 2.3: Phase diagram and free energy of a spinodal decomposition.

Before the (Ge,Mn) thin film growth, a clean and single crystal GaAs surface is necessary, so the native oxide or the amorphous Arsenic capping layer (see below) present initially on GaAs were desorbed by heating the substrate in the UHV growth chamber. In order to have a good GaAs surface condition before (Ge,Mn) growth, we have tested several methods to prepare the GaAs surface. According to different surface conditions of GaAs(001) before the growth of the 80 nm thick (Ge,Mn) film, we classify our samples into two groups as:

- *Ga-GeMn* : we use *epiready* GaAs(001) wafers and remove the native oxide layer on GaAs(001) substrate surface by thermal desorption to 600°C in the UHV chamber to obtain a Ga-rich surface, and then we grow a few nanometer Ge buffer growth before the (Ge,Mn) film growth. These samples are labelled Ga-GeMn hereafter.
- *As-GeMn* : we use another type of GaAs wafer with a thin undoped GaAs buffer grown first in a separate III-V epitaxy system, and protected with an amorphous Arsenic capping layer[2]. Then in our IV-IV MBE machine, we remove the As capping layer at 200°C to prepare a

[2]These GaAs(001) wafers with capping amorphous Arsenic were provided by LAAS-CNRS at Toulouse in France.

very flat As-rich surface for the growth of (Ge,Mn) films with different Mn concentrations at different temperatures. These samples are labelled As-GeMn hereafter.

2.2 Microstructure analysis

After the sample growth, we need some analyzing techniques to understand the microstructure of our materials. Here, we describe Transmission Electron Microscopy used to analyze the microstructure of (Ge,Mn) films and Secondary Ion Mass Spectrometry used to evaluate the chemical compositions and their distribution in the films.

2.2.1 Transmission Electron Microscopy (TEM)

Transmission electron microscopy (TEM) is a microscopy technique whereby a beam of high energy electrons ($\geq$ 100kV) is transmitted through an ultra thin specimen (normally less than 100nm), interacting with the specimen as it passes through. An image is formed from the interaction of the electrons transmitted through the specimen; the image is magnified and focused onto an imaging device, such as a fluorescent screen, on a layer of photographic film, or to be detected by a sensor such as a CCD camera. A typical TEM system is shown in the figure 2.4.

TEM is capable of imaging at a significantly higher resolution than light microscopes, owing to the small de Broglie wavelength of electrons ($\lambda = h/p$, where h is Plank's constant, and p is momentum of electrons). This enables the instrument's user to examine fine detail-even as small as a single column of atoms, called High-resolution transmission electron microscopy (HRTEM), which is tens of thousands times smaller than the smallest resolvable object in a light microscope. At smaller magnifications TEM image contrast is due to absorption of electrons in the material, due to the thickness and composition of the material. At higher magnifications complex wave interactions modulate the intensity of the image, requiring expert analysis of observed images. Alternate modes of use allow for the TEM to observe modulations in chemical identity, crystal orientation, electronic structure and sample induced electron phase shift as well as the regular absorption based imaging[50].

In the present work TEM observations were performed by Pascale Bayle-Guillemot[3], Thibaut Devillers and Eric Prestat using a JEOL 4000EX microscope with an acceleration voltage of 400 kV.

[3]CEA-Grenoble/INAC/SP2M/LEMMA

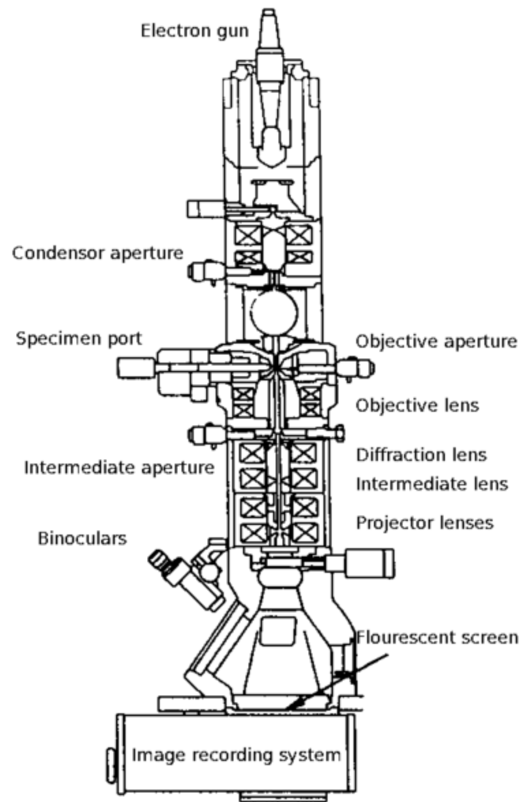

Figure 2.4: A typical TEM system.

2.2.2 Secondary Ion Mass Spectrometry (SIMS)

Secondary Ion Mass Spectrometry (SIMS) is widely used for analysis of trace elements in solid materials, especially semiconductors and thin films. The SIMS technique is noted for its exceptional sensitivity, depth profiling capability, mass range from hydrogen(H) to uranium(U), and lateral resolution of 1 μm or less. SIMS is superior to other related surface analysis techniques where high sensitivity (detection limits in the *ppb* range), extended dynamic concentration range, and the ability to perform isotope analysis are of concern. The fundamental basis of SIMS analyses is the measurement of the mass and intensity of secondary ions produced in a vacuum by sputtering the sample surface with energetic ion or neutral beams. The sputtering beam is referred to as the primary beam and typically has a kinetic energy of several thousand electronvolts. The primary beam removes atomic or molecular layers at a rate determined principally by the intensity, mass, energy of the primary species and the physical and chemical characteristics of the sample.

Sputtering of the sample produces a variety of particles including electrons, photons, atoms, atomic clusters, molecules and molecular fragments. A small fraction of these sputter products is ionized, and these ions are the secondary ions, which are separated by mass analyzer and reach detector as shown in figure 2.5.

In the present work SIMS analyses were provided by Probion analysis using O2+ (to detect Mn, Ge, B, Si, In) or Cs+ (to detect Mn, Ga, Ge, As). Implanted germanium samples were available to calibrate B, Ga and As analyses.

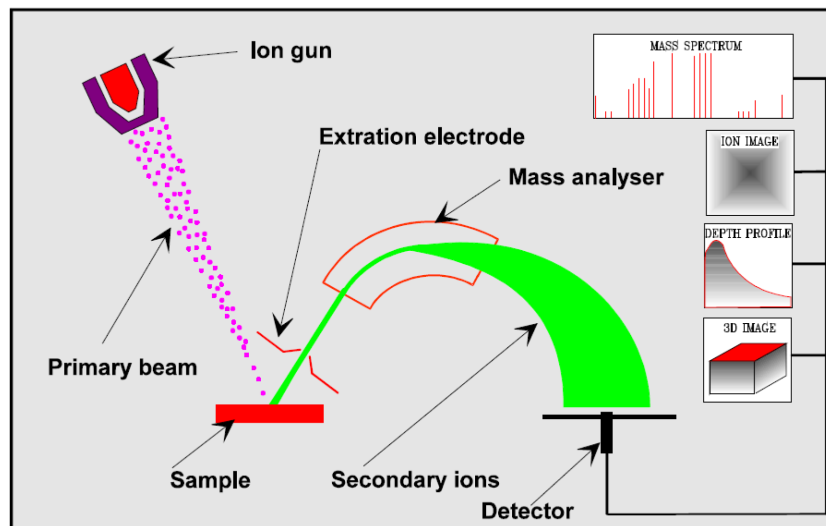

Figure 2.5: A schematic diagram of SIMS system.

2.3 Magnetic measurements

The magnetic properties of our (Ge,Mn) films were analyzed by SQUID magnetometry. Here are the introduction of basic theory of SQUID, superparamagnetic analyzing method, and our fitting method to study the magnetism of (Ge,Mn) films.

2.3.1 Superconducting QUantum Interference Device (SQUID)

For the study of the magnetic properties of (Ge,Mn) films, we use the magnetometry of Superconducting Quantum Interference Device (SQUID) which is a very sensitive device used to measure the magnetization signal as low as 10^{-8} e.m.u.. For our SQUID system, the applying magnetic field is up to 5T and its temperature range is from 2 K to 400 K. A SQUID magnetometer normally consists of:

- Superconductor coils to create a magnetic field around the sample,
- Detecting coils to detect the field induced by the sample,
- Superconducting quantum interference device to measure the magnetization,
- Temperature controlling system (cryostat and heater).

SQUID technique combines superconducting materials and Josephson junctions. A Josephson junction is a type of electronic circuit capable of switching at very high speeds when operated at temperatures approaching absolute zero, which is named for the British physicist who designed it[81]. It is made up of two superconductors, separated by a non-superconducting layer so thin that electrons can cross through the insulating barrier. The flow of current between the superconductors in the absence of an applied voltage is called a Josephson current, and the movement of electrons across the barrier is known as Josephson tunneling. Two or more junctions joined by superconducting paths form what is called a Josephson interferometer. This effect is influenced by magnetic fields in the vicinity, a capacity that enables the Josephson junction to be used in devices that measure extremely weak magnetic fields in figure 2.6. When there is no external magnetic field, the injection current (I) in the coils separates to half ($I/2$) passing through each junction. If a magnetic field (B_a) is applied perpendicular to the plane of ring, a phase difference ($\Delta\phi$) is produced in the electron-pair wave along

the path XYW and WZX, and an additional current (i) is created.

$$\Delta\phi\left(B_a\right) = \phi_W - \phi_X = n\pi\frac{\Phi_a}{\Phi_0} \tag{2.1}$$

$$\frac{I}{2} + i = i_c sin\phi_W = i_c sin(\Delta\phi + \delta) \tag{2.2}$$

$$\frac{I}{2} - i = i_c sin\phi_Z = i_c sin(\Delta\phi - \delta) \tag{2.3}$$

$$I = 2i_c cos\Delta\phi cos\Delta\phi = 2i_c sin\delta cos\left(n\pi\frac{\Phi_a}{\Phi_0}\right) \tag{2.4}$$

In these equations, Φ_0 is the quantum flux, and δ equals to $\phi_W + \phi_X$. As $sin\delta$ can not be larger than unity, we have a critical current ($I_C = 2i_c cos\left(n\pi\frac{\Phi_a}{\Phi_0}\right)$). Therefore, the measurement of this current gives the magnetic flux through the coils of SQUID.

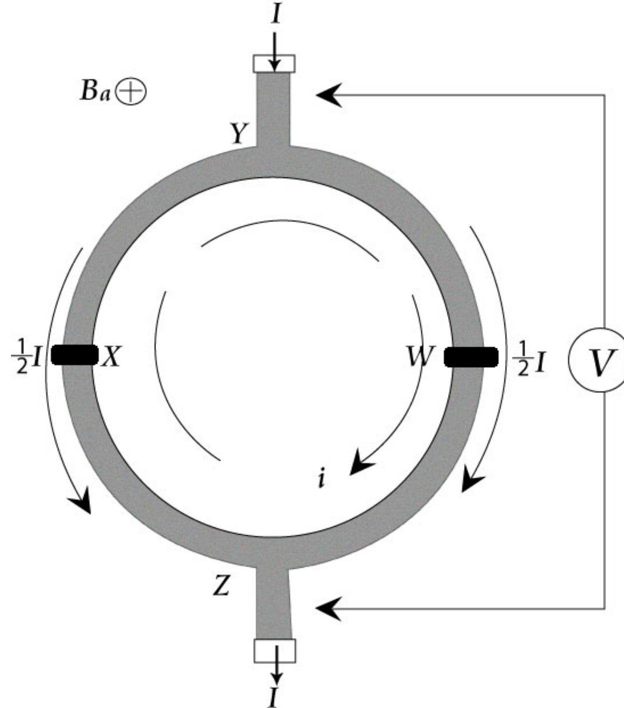

Figure 2.6: Superconducting quantum interference device as a single magnetometer.

2.3.2 Superparamagnetism

Superparamagnetism is a form of magnetism, which appears in small ferromagnetic or ferrimagnetic nanoparticles and occurs below the Curie temperature of the material. In small enough nanoparticles, magnetization can randomly flip direction under the influence of temperature. The typical time between two flips is called the Néel relaxation time (τ_N). In the absence of external magnetic field, when the time used to measure the magnetization of the nanoparticles is much longer than the Néel relaxation time ($\tau_{mes}>>\tau_N$), their magnetization appears to be in average zero: they are said to be in the superparamagnetic state. In this state, an external magnetic field is able to magnetize the nanoparticles, similarly to a paramagnet.

$$\tau_N = \tau_0 e^{\frac{\Delta E}{k_B T}} \tag{2.5}$$

$$T_B = \frac{K_1 V}{k_B ln(\frac{\tau_{mes}}{\tau_0})} \tag{2.6}$$

- ΔE is the energy barrier associated with the magnetization moving from its initial "easy axis" direction, through a "hard axis", ending at another easy axis.

- τ_N is the average length of time that it takes for the nanoparticle magnetization to randomly flip as a result of thermal fluctuations.

- τ_0 is a length of time, characteristic of the material, called the attempt time ; its typical value is 10^{-9} to 10^{-10} second.

- T_B is the temperature for which τ_N=τ_0 called the blocking temperature because, below this temperature, the magnetization is seen as "blocked" on the time scale of the measurement.

- τ_{mes} is the measuring time.

- K_1 is the constant of nanoparticle magnetic anisotropy, and V is the volum of ferromagnetic nanoparticles, and K_1V=ΔE.

- k_B is the Boltzmann constant, and T is the temperature.

Superparamagnetism is governed by a temperature T_B such that the thermal energy is equal to the energy barrier of two magnetic states (ΔE). For $T << T_B$, the particles appear as ferromagnetic. For $T \geq T_B$, the thermal energy is high enough to make it flip from one magnetic state to another,

this is the superparamagnetic state. In figure 2.7, we show an example of the so-called ZFC-FC curves measured on Fe_3O_4[51]. The sample is cooled down to the temperature below T_B without magnetic field (ZFC: zero field cooled). Then a weak field is applied, the initial magnetization is zero because the particles are blocked randomly. As the temperature increases (below T_B), some particles have enough energy to align their magnetic moment with applied field until T_B. As temperature keeps increasing, the magnetization decreases as a function of 1/T due to thermal agitation. When the sample is cooled down with field (FC) to block them again, the magnetization increases to very low temperature because the particles have been aligned by the applied field. These irreversible curves can be used to characterize the superparamagnetic properties of the samples. They can be used also to study their magnetic anisotropy by comparing with the in-plane and out-of-plane measurements of ZFC-FC curves.

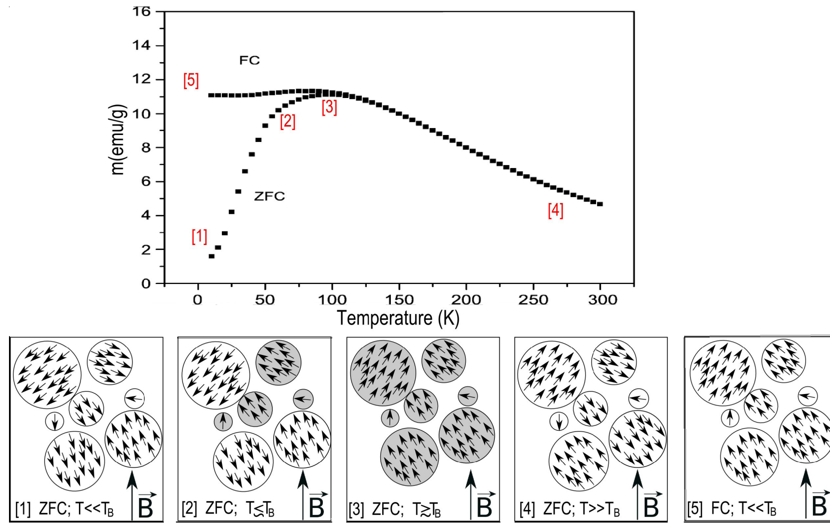

Figure 2.7: Zero Field Cooled - Field Cooled (ZFC-FC) measurement of Fe_3O_4 with blocking temperature around 100K. The sketches show the magnetization of superparamagnetic nanoparticles during ZFC-FC measurement.

2.3.3 Magnetic phase analysis

In this thesis, we use SQUID magnetometry to measure the magnetization of (Ge,Mn) films as a function of magnetic field at different temperatures. The applied magnetic field is in the direction of the surface (in-plane), unless specified. In order to separate the magnetic contribution of different phases in (Ge,Mn) films, we use a fit with a Brillouin function to subtract

the paramagnetic component, and a Langevin function is employed to fit out the magnetic moment and magnetic size of the Mn-rich phases[4]. Here, these two functions are briefly introduced.

The Brillouin function[52] is a special function defined by the following equation:

$$B_J(x) = \frac{2J+1}{2J} coth\left(\frac{2J+1}{2J}x\right) - \frac{1}{2J} coth\left(\frac{1}{2J}x\right) \tag{2.7}$$

This function is best known for arising in the calculation of the magnetization of an ideal paramagnet. In particular, it describes the dependence of the magnetization (M) on the applied magnetic field (B) and the temperature T for a total angular momentum quantum number (J) of the microscopic magnetic moments. The magnetization is given by:

$$M = Ng\mu_B J B_J(x) \tag{2.8}$$

- N is the number of atoms per unit volume,
- g is g-factor,
- μ_B is Bohr magnetron
- x is the ratio of Zeeman energy of the magnetic moment in the external field to the thermal energy $k_B T$; $x = (g\mu_B JB/k_B T)$
- k_B is Boltzman constant and T is temperature

In the classical limit, the magnetic moment can be continuously aligned in the field and J can assume all values ($J \rightarrow \infty$). The Brillouin function is then simplified into the Langevin function:

$$L(x) = coth(x) - \frac{1}{x} \tag{2.9}$$

[4]SQUID measurments were conducted by Matthieu Jamet (CEA-Grenoble/INAC/SP2M/NM) and Abhinav Jain (CEA-Grenoble/INAC/SP2M/SiNaPS)

2.4 Magnetotransport measurements

Once the (Ge,Mn) films grown by LT-MBE, some processes in cleanroom are necessary for the sample preparation. Then, we transfer it into our liquid Helium cryostat system with magnetic field up to 9 Tesla and temperature control from 3 K to 300 K for the transport measurement. Hall resistance and magnetoresistance are available during the measurement. By changing the orientation between magnetic field and sample, we also can have the anisotropic magnetoresistance measurement. Besides these techniques, I am also going to introduce the basic theory of magnetotransport including Hall effect, Anomalous Hall effect, and various magnetoresistance behaviors.

2.4.1 Sample preparation

I realized the double Hall-cross bars with 20 μm line-width by optical lithography in the PTA cleanroom[5]. All of the processes are listed as follows and shown in figure 2.8:

- Sample cleaning by D.I. water and Acetone
- First optical lithography with AZ1813
- Mesa etching by Ar ion
- Second optical lithography with AZ5214
- Metal contact with Au
- Package on carrier by Al wire bounding

2.4.2 Helium cryostat system

After the sample preparation, we use a helium cryostat system to realize the magnetotransport measurement in figure 2.9. In our helium cryostat system we can apply the magnetic field from 9 Tesla to -9 Tesla, control the temperature from 3K to 300K and change from 0 degree to 180 degree the angle between the magnetic field and the current's direction. During the measurement, we get the values of Hall resistance (R_{xy}) and magnetoresistance (R_{xx}) at different parameters, and the magnetic field is perpendicular to samples surface when not specified.

[5]Plateforme Technologique Amont(PTA) at Grenoble in France

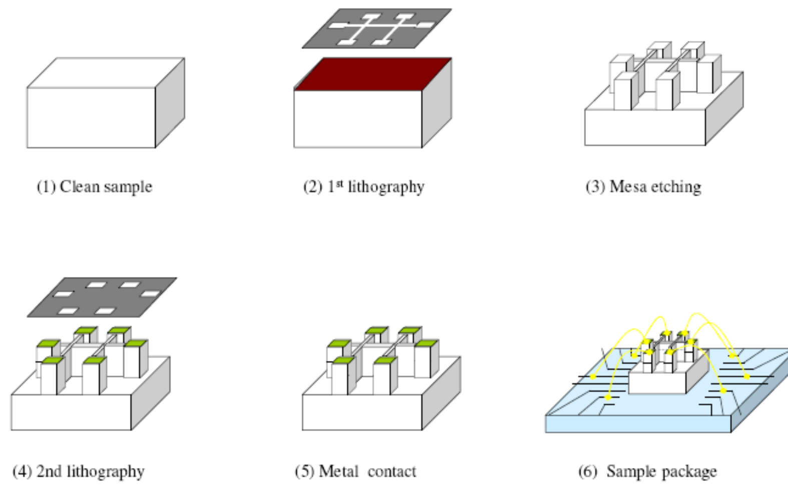

Figure 2.8: Double Hall-cross bar process.

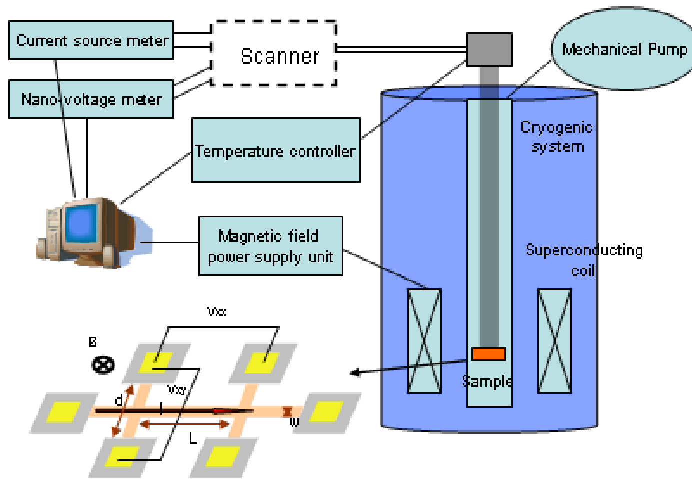

Figure 2.9: Diagram of our cryostat system.

2.5 Mechanisms of magnetotransport

When a material is subjected to an external field, currents of charge or energy may flow. These responses to applied fields are the transport properties, which provide valuable information on the material. Here, the magnetotransport phenomena, electron transport under an electric field and a magnetic field simultaneously, include Hall effect and magnetoresistance (MR). From Hall measurements, we can have the carrier type, concentration and mobility of each sample. Besides, anomalous Hall effect give us an information on the coupling of spin and orbital motion of electrons in our samples. Magnetoresistance provides a measure of the scattering events contributing to the magnetic resistance. Various magnetoresistance behaviors are also introduced in the end of this section.

2.5.1 Hall effect

The Hall effect was discovered in 1879 by Edwin Herbert Hall[53]. It comes from the nature of the current in a conductor. As Figure 2.10 shows, current consists of the movement of many small charge carriers, typically electrons, holes, or both. Moving charges experience a force, called the Lorentz Force, when a magnetic field is present that is not parallel to their motion. When such a magnetic field is absent, the charges follow a straight line. However, when a perpendicular magnetic field is applied, their path is curved so that moving charges accumulate on one face of the material. This leaves equal and opposite charges exposed on the other face. The result is an asymmetric distribution of charge density across the Hall element that is perpendicular to both the current flow path and the applied magnetic field. The separation of charges establishes an electric field that opposes the migration of further charge, so a steady electrical potential builds up for as long as the charge is flowing. From Hall measurement, we can know the carrier type of samples (p-type or n-type), carrier concentration (n), and its Hall mobility (μ). Here are equations of Hall measurement (with quantities defined in the figure):

$$\rho_{xx} = R_{xx}.\left(w/l\right).t \tag{2.10}$$

$$R_H = \left(\Delta R_{xy}/\Delta B\right).t \tag{2.11}$$

$$n = 1/\left(R_H.e\right) \tag{2.12}$$

$$\mu = R_H/\rho_{xx} \tag{2.13}$$

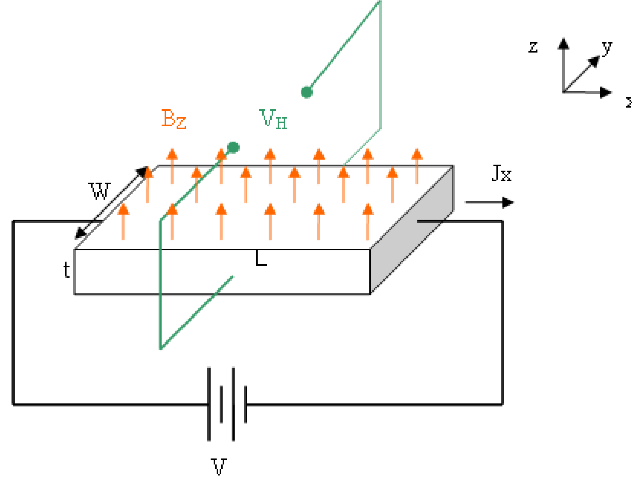

Figure 2.10: Classical Hall effect experiment

2.5.2 Anomalous Hall effect

In ferromagnetic materials, the Hall resistivity includes an additional contribution, known as the anomalous Hall effect (or the extraordinary Hall effect), which depends directly on the magnetization of the material, and is often much larger than the ordinary Hall effect. The Hall resistivity ρ_H is thus given as:

$$\rho_H = R_0 H + 4\pi R_s M \tag{2.14}$$

The first and second terms are the ordinary and anomalous Hall effect, respectively. Coefficients R_0 and R_s are called as ordinary and anomalous Hall coefficients. In the experiment of anomalous Hall effect, with increasing the external magnetic field, ρ_H changes rapidly at first, and then it tends to increase in proportion to H. This initial rapid change is caused by the magnetization term ($4\pi R_s M$). After the saturation of magnetization, ρ_H linearly changes with external magnetic field. Although it's a well-recognized phenomenon, there is still debate about its origins in the various materials. The anomalous Hall effect (AHE) can be either an extrinsic (disorder-related) effect due to spin-dependent scattering of the charge carriers, or an intrinsic effect which can be described in terms of the Berry phase effect in the crystal momentum space[54].

Intrinsic mechanism, which results from the Berry phase, was first proposed to explain AHE in 1954[55]. The essential point in the theory is a

contribution to the velocity from the Berry phase $\Omega(k)$ as shown by:

$$\dot{x} = \frac{1}{\hbar}\frac{\partial \epsilon(k)}{\partial k} - \dot{k} \times \Omega(k) \tag{2.15}$$

$$\hbar\dot{k} = -eE_{ext} - e\dot{x} \times B_{ext} \tag{2.16}$$

We see that the velocity $\dot{x}$ has a component perpendicular to E_{ext} even when $B_{ext} = 0$. A term $eE_{ext} \times \Omega(k)$ plays a role of an effective magnetic field. Because $\Omega(k)$ is a quantity in the momentum space and is dependent on the wave vector, the effective field may be interpreted as a magnetic field in the momentum space. The AHE caused by intrinsic mechanisms is called intrinsic AHE.

Most of the experiments, however, have been interpreted by extrinsic mechanisms, skew-scattering[56] and side-jump[57] in the figure 2.11. In skew-scattering mechanism, the up-spin and down-spin electrons are scattered into opposite directions; on the other hand, in side-jump mechanism, it occurs a displacement of electron path. In ferromagnetic materials, this spin imbalance makes the spin-up and spin-down charges Hall currents asymmetric and produces a Hall voltage proportional to the spin polarization. Here, the AHE caused by the extrinsic mechanisms is called extrinsic AHE[58].

Figure 2.11: Skew-scattering and side-Jump

2.5.3 Magnetoresistance

Magnetoresistance (MR) is the variation of electrical resistance due to an external magnetic field (**H**)[59]. Positive or negative MR refers to the increase or decrease of resistance with the magnetic field. MR effects in metallic, semiconducting and insulating materials have different characteristics. MR of magnetic thin films and multilayer is one of their most interesting transport properties and results from the different scattering properties of spin-up and spin-down electrons. Normally, magnetoresistance is defined as:

$$MR(\%) = \frac{R(H) - R(0)}{R(0)} \tag{2.17}$$

Where $R(H)$ is the resistance at certain magnetic field value H, and R(0) is the resistance at zero magnetic field. In our case, the magnetic field is perpendicular to the current direction when not specified.

For the thin-film samples of MR measurement, where the electric current with the current density (**j**) is usually in the film plane, MR can be measured in three geometries: $\rho_{||}$ (longitudinal MR, **H** is in the same direction of **j**), ρ_T (transverse MR, **H** is in the film plane and perpendicular to **j**), and $\rho_\perp$ (perpendicular MR, **H** is perpendicular to the film plane and perpendicular to **j**), as show in figure 2.12. In order to ascertain the characteristics of MR, it is generally necessary to measure in more than one field orientation[60].

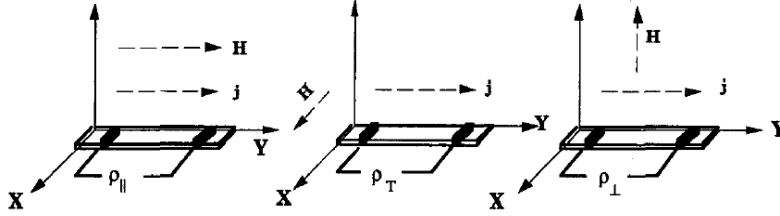

Figure 2.12: Longitudinal magnetoresistivity $\rho_{||}$, transverse magnetoresistivity ρ_T, and perpendicular magnetoresistivity $\rho_\perp$ measured in an external magnetic field (**H**) applied in different direction with respect to a current, with current density (**j**) flowing in the plane of thin-film samples.

For a Drude metal of free electrons, there is no MR, *i.e.* the resistance is independent of the magnetic field in figure 2.13(a). The characteristics of MR in various real materials at low temperatures can be summarized as:

- *Ordinary magnetoresistance* (OMR): For ordinary non-magnetic metals, such as Au and Cu, the MR is quite small. Both $\rho_{||}$ and $\rho_\perp$ are positive and vary as $\mathbf{H^2}$ in figure 2.13(b). For magnetic films (such as 100nm thick Co), OMR is observed when the magnetic field is larger than the saturation. In both cases, OMR arises from the force on an electron which is due to the Lorentz force and the electric field, and by a simple semi-classical argument, $MR \propto (\mu \cdot H)^2$).
- *Anisotropic magnetoresistance* (AMR): In ferromagnetic metals (*e.g.* Fe, Co) and alloys (*e.g.* permalloy), substantial MRs are observed.

It is almost always the case that $\rho_{||}$ is positive and ρ_T is negative, as shown in figure 2.13(c), and $\rho_{||} > \rho_T$, which is opposite to the behavior of OMR. Both $\rho_{||}$ and ρ_T can be saturated under a modest field. The AMR depends on the direction of spontaneous magnetization and is due to the rotation of the ferromagnetic domains under the external field.

- *Giant magnetoresistance* (GMR): In magnetic multilayer composed of an alternating stack of thin ferromagnetic and non-magnetic metal layers, the resistivity has remarkably different between the ferromagnetic and antiferromagnetic alignments, which is always negative, as shown in figure 2.13(d). Because of the layer structure, GMR in multilayer is not isotropic. ($\rho_\perp > \rho_{||} \cong \rho_T$). However, GMR effect was also discovered in granular magnetic systems, and it is isotropic, as shown in figure 2.13(e)[61][62].

- *Tunnel magnetoresistance* (TMR): When two ferromagnetic materials are separated by an insulating layer or an energy barrier, the spin polarization of electrons governs the MR ratio in this ferromagnetic tunnel junction. If the magnetizations are in a parallel orientation it is more likely that electrons will tunnel through the insulating film than if they are in the antiparallel orientation. Consequently, such a junction can be switched between two states of electrical resistance, one with low and one with very high resistance. This is similar to GMR, and the MR ratio is defined as:

$$MR(\%) = \frac{\rho_{AP} - \rho_P}{\rho_P} \tag{2.18}$$

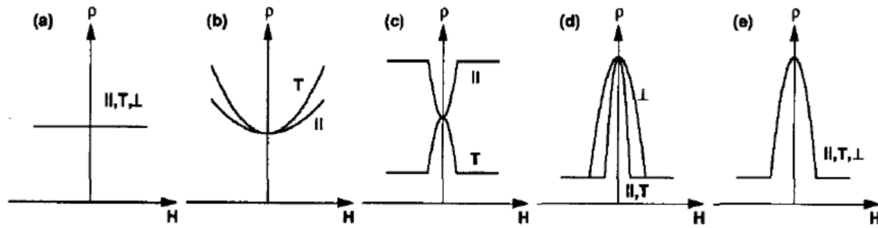

Figure 2.13: Various magnetoresistance behaviors: (a) The absence of MR in a Drude metal, (b) Ordinary MR in a non-magnetic metal, (c) Anisotropic MR in a ferromagnetic metal, (d) negative Giant MR in a multilayer, and (e) negative Giant MR in a granular solid.

In conclusion, magnetotransport is an important tool to study the thin film of ferromagnetic semiconductors, in which the magnitude of the total magnetization is typically small. The nature of AHE can serve to determine the magnitude of magnetization. Moreover, MR ratio provides information on the magnetism and on the interplay between electronic and magnetic degree of freedom. In this thesis, (Ge,Mn) films are studied by the technique of magnetotransport.

Chapter 3

Results and discussion

In this chapter, we are going to report that surface morphology and chemical species on the surface of GaAs substrates (the stoichiometry of the surface) change the growth mechanism of (Ge,Mn) films, which induces different nanostructures in these films. These different microstructures of (Ge,Mn) films present different magnetic and magnetotransport properties. In this work, by using different GaAs(001) wafers, we have two main groups of samples, *Ga-GeMn* grown with *epiready* GaAs(001) substrates and *As-GeMn* grown with amorphous Arsenic capped GaAs(001) substrates. Finally, a simulating tool is employed to calculate the magnetotransport properties in order to compare with our experimental results.

In the first part of this chapter, we focus on the Ga-GeMn samples to study their microstructures by TEM, chemical composition analysis by SIMS, magnetism by SQUID and their magnetotransport properties, which include anomalous Hall effect and different magnetoresistance behaviors at different applied magnetic fields and measuring temperatures. **In the second part**, we will investigate the As-GeMn samples by the same techniques. However, in these As-rich (Ge,Mn) films, we can find the different microstructures of (Ge,Mn) films and the segregation of Arsenic atoms in the upper (Ge,Mn) film. The transport properties are dominated by the compensation effect of donors and acceptors. Therefore, we obtain totally different magnetotransport properties and weak localization effect during the transport of electrons. **Finally**, we introduce a simulation method of magnetotransport in an inhomogeneous system , and compare its results with our experimental results.

3.1 Ga-GeMn samples

In this group of samples, Ga-GeMn, (Ge,Mn) thin films are grown on *epiready* GaAs(001) substrates, which are Ga-rich. As in the case of the growth on Ge substrates, self-organized Mn-rich nanocolumns are found in the (Ge,Mn) films, due to spinodal decomposition[21]. In the beginning of this study, the rough GaAs surface induced (Ge,Mn) film growth with non-parallel nanocolumns. Then we could grow parallel Mn-rich nanocolumns thanks to a thick buffer layer grown on the GaAs substrate, but this is not suitable for current-in-plane transport measurements. However, a new surface preparation method was developed, called "Star", in order to have a flatter surface for (Ge,Mn) films grown on GaAs(001) directly. Very low Ge flux is applied during the desorption of oxide layer. By this method, parallel Mn-rich nanocolumns can be grown directly on a GaAs substrate. Then, from the SQUID measurement, we detect two magnetic phases: one is Mn-rich nanocolumns, and the other is diluted Mn atoms in Ge matrix. Finally, magnetotransport shows us p-type doping, low Hall mobility, AHE at low field and various MR behaviors in different temperature ranges.

3.1.1 Self-organized Mn-rich nanocolumns

Before starting the (Ge,Mn) film growth, we have to remove the native oxide layer of the *epiready* GaAs(001) substrate. This is done by thermal desorption at 600°C in the ultra-high-vacuum growth chamber. Then we grow around one nanometer of Ge buffer in our MBE system. With this method, we have a very rough and Ga-rich surface, as observed by RHEED in figure 3.1(a), because Arsenic atoms also evaporate from the GaAs substrate during the desorption of the oxide layer. After (Ge,Mn) film growth on this surface, we can find 2D Mn-rich nanocolumns in (Ge,Mn) films, as for the growth on a Ge substrate, but here these self-organized nanocolumns are entangled because of the rough surface, see figure 3.1(b). By using this technique, we have grown samples named Ga-LT-10% (T_g=100°C and 10% Mn) and Ga-LT-6% (T_g=100°C and 6% Mn) in Table 3.1, see below in section 3.1.3.

In order to prepare a flat surface for (Ge,Mn) films growth, we have grown a 40nm-thick Ge buffer layer after desorption of GaAs substrate (shown in figure 3.2(a)). From HRTEM image, parallel Mn-rich nanocolumns can be grown this way on GaAs substrate (shown in figure 3.2(b)), as those on Ge substrate.

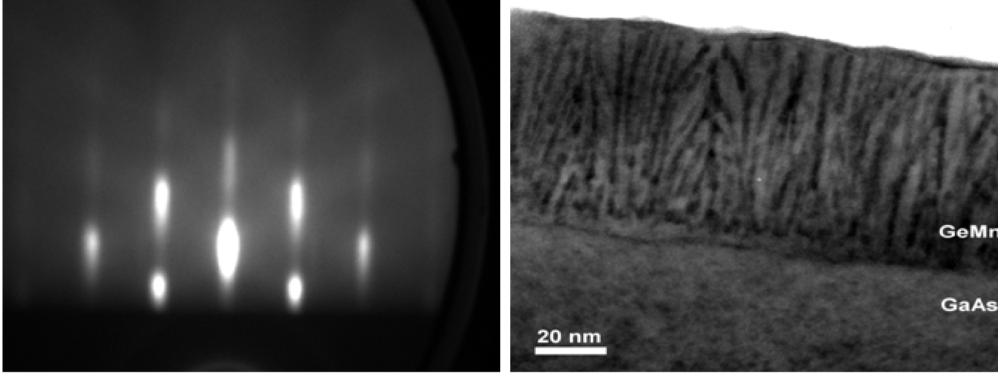

Figure 3.1: (a) Spotty RHEED pattern shows rough GaAs surface before growth, (b) By cross-section TEM image of the (Ge,Mn) film, Mn-rich nanocolumns are entangled.

These observations are well explained by the growth mechanism of Mn-rich self-organized nanocolumns in (Ge,Mn) films. The 2D spinodal decomposition involves a fast Mn diffusion on the surface of the growing sample (and comparatively negligible diffusion in the bulk) and preferential aggregation of Mn on the Mn-rich areas. Moreover, the growth of columns proceeds perpendicular to the growth surface; hence a rough surface gets nonparallel nanocolumns (figure 3.1(b)) and a flat surface gets parallel nanocolumns (figure 3.2(b)). This growth model was proposed by Sato *et al* in Kinetic Monte-Carlo simulation[26], [27].

For the Current-In-Plane (CIP) magnetotransport measurement, we need an Ge buffer layer as thin as possible to make the current pass the (Ge,Mn) films. In order to have flatter surface for (Ge,Mn) film grown directly on semi-insulating GaAs substrate, we used another technique (called "Star"), so that we can prepare a flat surface with (2×1) RHEED reconstruction, figure 3.3(a), before the (Ge,Mn) film growth. After 80 nm (Ge,Mn) grown by LT-MBE, the surface becomes rougher, and (2×1) RHEED reconstruction becomes less clear, figure 3.3(b). From the TEM observation, Mn-rich nanocolumns are parallel, and their diameter is around 3 nm in figure 3.3(c). Single crystal growth of (Ge,Mn) films is shown by High Resolution TEM image in figure 3.3(d). We prepared some samples by this technique such as samples Ga*-LT-4% (T_g=100°C and 4% Mn), Ga*-LLT-10% (T_g=90°C and 10% Mn), Ga*-LT-10% (T_g=100°C and 10% Mn) and Ga*-HT-10% (T_g=110°C and 10% Mn) for SQUID and magnetotransport measurements (listed in Table 3.1, see below in section 3.1.3).

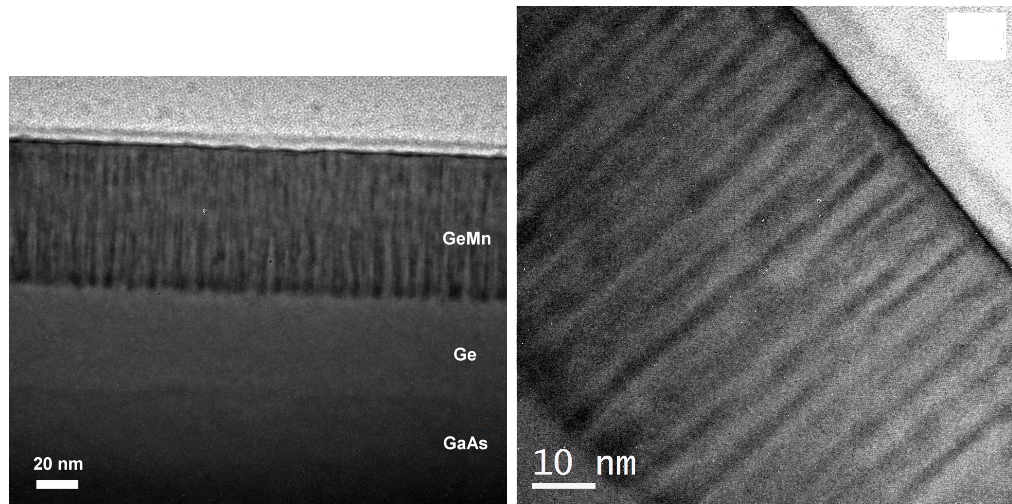

Figure 3.2: (a) (Ge,Mn) film grows on GaAs(001) with 40nm Ge buffer layer, and (b) HRTEM image shows parallel Mn-rich nanocolumns.

Besides the microstructure analysis by TEM, we used the SIMS technique to analyze the depth-profile concentration of Ga atom from (Ge,Mn) film surface to GaAs substrate: we can find that the Ga atoms diffuse from the GaAs substrate to (Ge,Mn) films in figure 3.4. This Ga diffusion affects the magnetotransport properties, which will be discussed in section 3.1.3.

To summarize, in Ga-GeMn samples, we grow (Ge,Mn) thin films on Ga-rich GaAs substrate by low temperature MBE. In these films, we have self-organized Mn-rich nanocolumns due to spinodal decomposition, and Mn-rich nanocolumn growth follows the surface morphology.

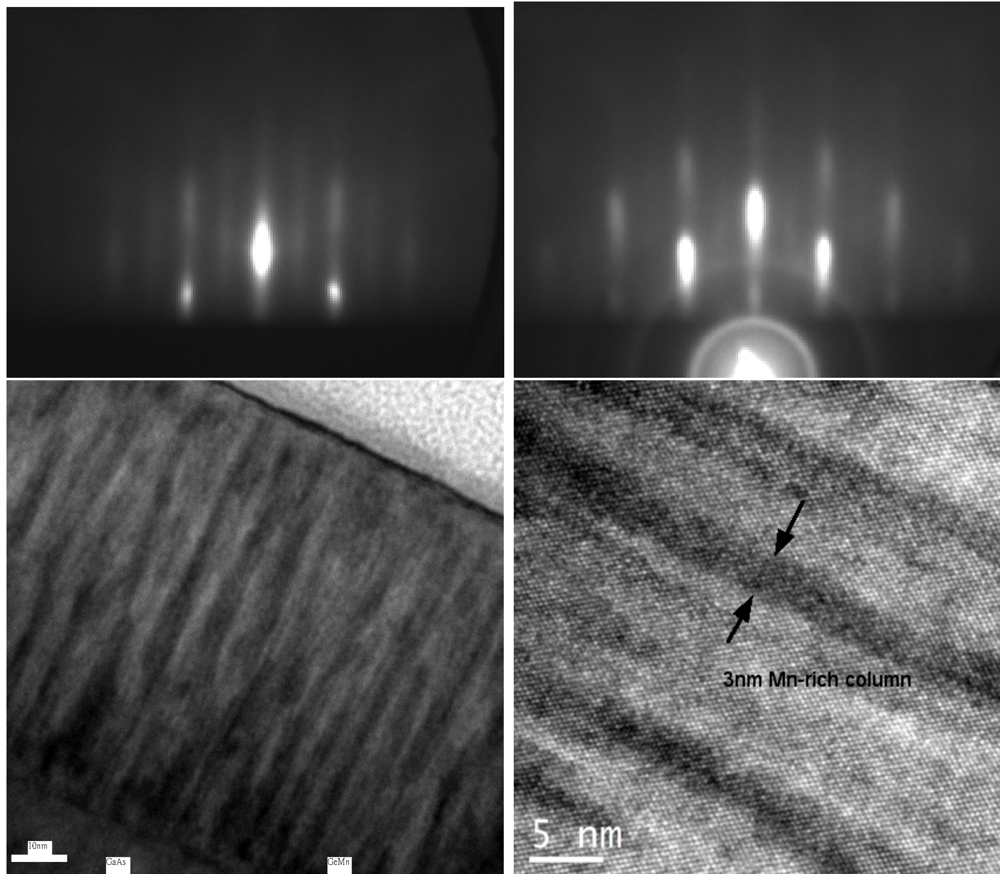

Figure 3.3: (a) (2×1) RHEED reconstruction shows flat GaAs surface, (b) RHEED pattern shows surface rougher after 80 nm (Ge,Mn) growth, (c) By cross-section TEM image of (Ge,Mn),Mn-rich nanocolumns are parallel, and (d) HRTEM image shows single crystal structure and around 3 nm columns.

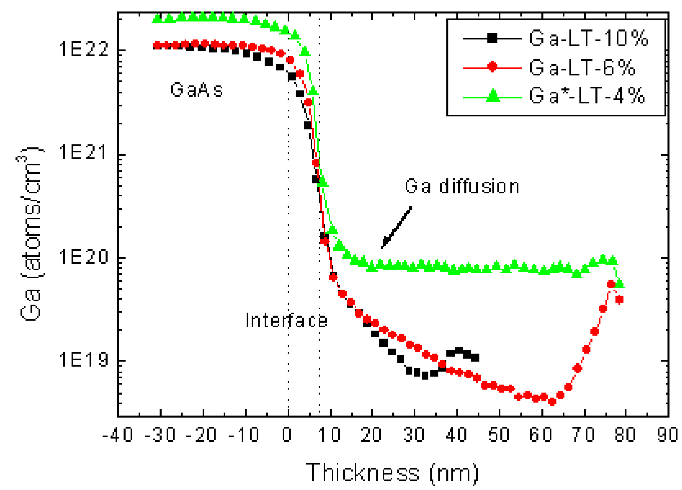

Figure 3.4: SIMS measurements of Ga profile for samples Ga-LT-10% (46 nm), Ga-LT-6% (80 nm) and Ga*-LT-4%: Ga atoms diffuse from GaAs substrate to (Ge,Mn) films.

3.1.2 Magnetic properties of Ga-GeMn

In this part, the study of magnetic property on Ga-GeMn samples is realized by SQUID magnetometry. When not specified, the external magnetic field is applied in the direction of film plane *i.e.* along [110] crystal axes.

All the magnetic measurements of Ga-LT-10% are presented in figure 3.5. They clearly evidence the presence of two magnetic phases in this material system: paramagnetic diluted Mn atoms in Ge matrix, and ferromagnetic Mn-rich nanocolumns.

In figure 3.5(a), the magnetization comes from these two phases. The very strong paramagnetic signal, which is attributed from diluted paramagnetic Mn atoms in Ge matrix, is clearly seen at low temperature. In order to obtain the magnetic signal contributed from ferromagnetic nanostructures (2D Mn-rich nanocolumns in this section), we make the assumption that it saturates below 5 T (discussed later). Then we can subtract, from the total magnetization curve, a 3/2-Brillouin function[77] fitting the paramagnetic signal from diluted Mn atoms, in order to end with a saturating magnetic signal (This fitting method was introduced in Chapter 2).

The SQUID measurement of Ga-LT-10% is reported as follows:

- *M-H curve* : We have the magnetization of (Ge,Mn) film (the curve with matrix signal) at temperature 5 K, and, after the fitting procedure, the magnetization of ferromagnetic nanocolumns (the curve without matrix signal) and (figure 3.5(a)). Figure 3.5(b) shows the magnetization at different temperatures, and the matrix signal has been subtracted for each temperature.

- M_r*-T curve* : Figure 3.5(c) shows the magnetic remanence as a function of temperature recorded after maximum field cooling (MFC) at 5 T. We find that the magnetic remanence becomes zero as the temperature rises above 15 K.

- M_s*-T curve* : From the temperature dependence of the saturation magnetization (recorded at 2 T) in figure 3.5(d), we can more clearly identify two different magnetic phases: a strong paramagnetic phase with a 1/T temperature dependence at low temperature is attributed to diluted Mn atoms in the Ge matrix, and a second magnetic phase with a Curie temperature close to 150 K is attributed to Mn-rich nanocolumns.

This is identical to the magnetotransport measurement (shown in section 3.1.3). Moreover, the saturation magnetization becomes negligible above 200 K ruling out the existence of Ge_3Mn_5 clusters in this sample.

- *ZFC-FC curve* : In figure 3.5(e), ZFC-FC curves show that Mn-rich nanocolumns are superparamagnetic with a blocking temperature close to 15 K, as already shown by the result of magnetic remanence.

- *ZFC-FC curve in-plane and out-of-plane* : Finally, the magnetic anisotropic of Ga-LT-10% is given by the comparison of in-plane and out-of-plane ZFC curves, which shows very little difference within the resolution limit of our SQUID figure 3.5(f); we thus conclude that magnetic anisotropy in Mn-rich nanocolumns is weakly out-of-plane.

From the SQUID measurement of the saturation values of Ga-LT-10%, we also can have the magnetic composition of the Mn-rich nanocolumns (40% $\pm$ 4); in addition, a Langevin fitting in the temperature range 60 K - 120 K, between T_B and T_C, gives the average magnetic moment of the Mn-rich nanocolumn ($520 \pm 50\mu_B$). (To be compared with As-GeMn samples in section 3.2.2)

Meanwhile, for the SQUID measurements on sample Ga*-LLT-10% shown in figure 3.6, we find similar results as for sample Ga-LT-10%. Figure 3.6(a) shows the magnetization at different temperatures. From the temperature dependence of the saturation magnetization (recorded at 5 T) in figure 3.6(b), we also identify two different magnetic phases, and Mn-rich nanocolumns have a Curie temperature close to 150 K. In figure 3.6(c), ZFC-FC curves show that the Mn-rich nanocolumns are superparamagnetic with a blocking temperature close to 20 K. Thus, from the SQUID measurements, there is no significant difference of magnetic properties between non-parallel Mn-rich nanocolumns and parallel Mn-rich nanocolumns.

To conclude on the magnetic properties of Ga-GeMn samples: we observe two magnetic phases (paramagnetic diluted Mn atoms in the Ge matrix, and ferromagnetic Mn-rich nanocolumns). For samples with non-parallel and parallel nanocolumns, there is no significant difference in the magnetic properties.

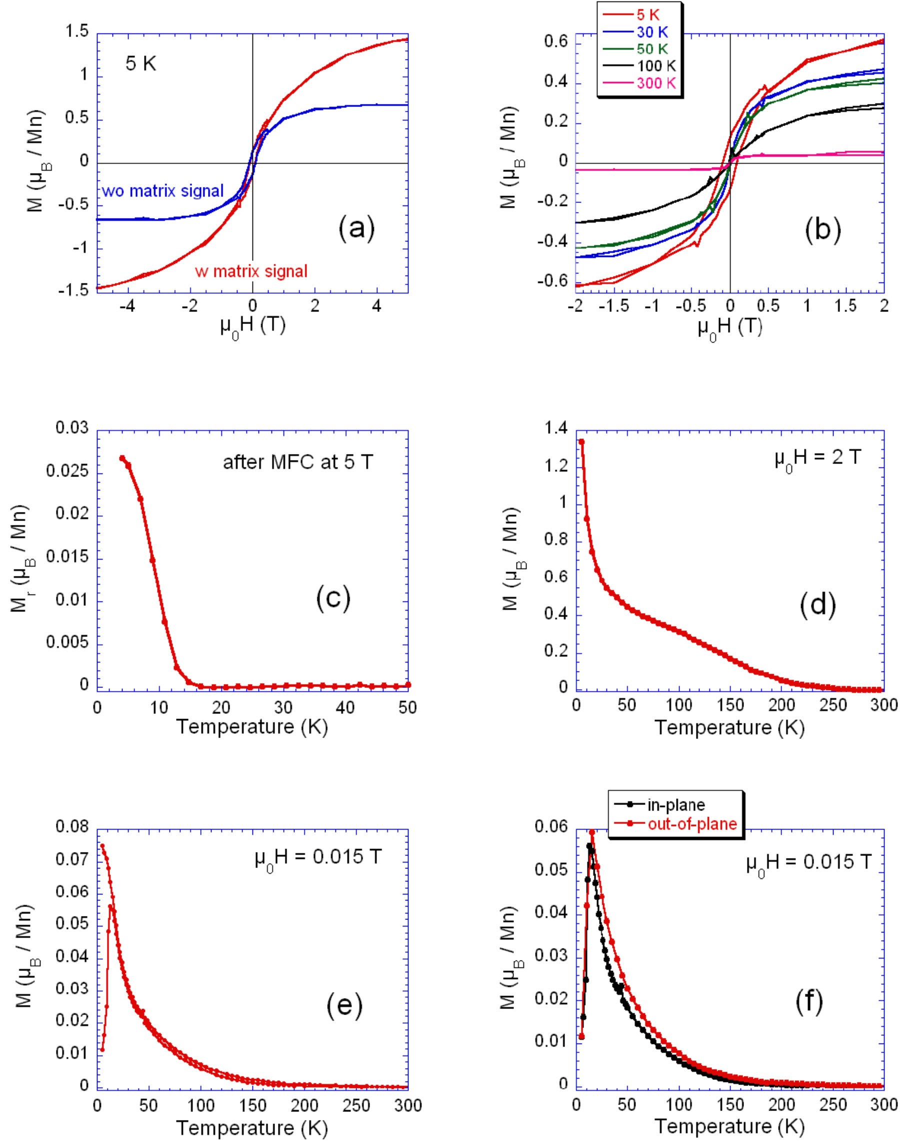

Figure 3.5: Magnetic measurements performed on Ga-LT-10% sample. (a) Magnetization curve recorded at 5 K with and without the paramagnetic signal from diluted Mn atoms. (b) Magnetization curves as a function of temperature. The matrix signal has been subtracted for each temperature. (c) Magnetic remanence as a function of temperature recorded after maximum field cooling (MFC) at 5 T. (d) Temperature dependence of the saturation magnetization recorded at 2 T. (e) ZFC-FC curves recorded under 0.015 T. (f) ZFC curves recorded in-plane (external magnetic field applied in the film plane along [110]) and out-of-plane (magnetic field perpendicular to the film plane along [001]) at 0.015 T.

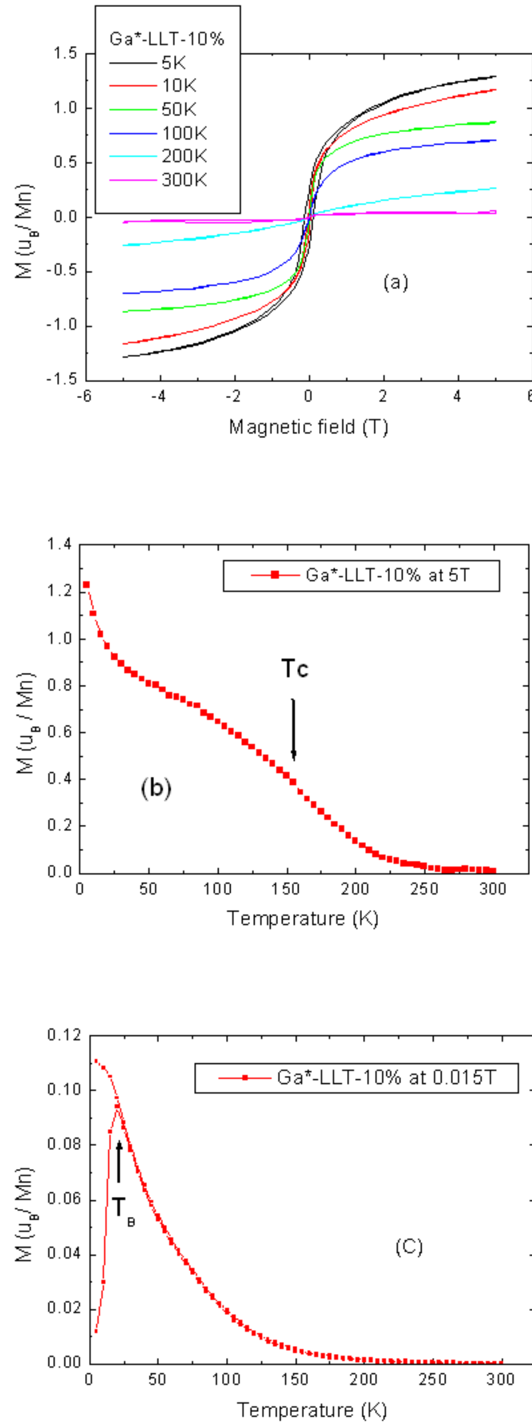

Figure 3.6: Magnetic measurements performed on Ga*-LLT-10% sample. (a) Magnetization curves as a function of temperature, (b) Temperature dependence of the saturation magnetization recorded at 5 T, and (c) ZFC-FC curves recorded under 0.015 T.

3.1.3 Magnetotransport of Ga-GeMn

For the magnetotransport measurements of Ga-GeMn samples, the electrical current passes through the (Ge,Mn) films (Current-In-Plane configuraion), and the magnetic field is perpendicular to the plane. From the transport measurement, we deduce the values of carrier density and Hall mobility shown in Table 3.1. We find that all of them exhibit p-type doping; and anomalous Hall effect is more visible for samples with 10% Mn. In order to minimize the influence of anomalous Hall effect (shown in section 3.1.3), we consider the high field slope of Hall measurement in order to derive the carrier density and Hall mobility in the (Ge,Mn) films. Meanwhile, we present the MR ratio at magnetic field equal to 8 T in Table 3.1: it changes from negative to positive, except for sample Ga*-LT-4%. (discussed in section 3.1.3).

In Ga-GeMn samples, Mn atoms act as double acceptor in germanium, with acceptor levels located 160 meV and 370 meV above the valence band edge[78], [79]. Besides, we find a significant out-diffusion of Ga, from the GaAs(001) substrate with Ga-rich surface, into the (Ge,Mn) film. As Ga also acts as an acceptor in germanium, it may enhance the hole density in Ga-GeMn samples.

Table 3.1: Carrier density, Hall mobility and MR ratio at 8 T in (Ge,Mn) films grown on GaAs(001). The Hall mobility is defined as μ_H=R_H/ρ_0 where R_H is the Hall constant and ρ_0 the zero field resistivity.

Samples	carrier density (cm^{-3})	Hall mobility ($cm^2.V^{-1}.s^{-1}$)	MR at 8 T (%)
Ga-LT-10%	$1.9.10^{19}$ / $3.0.10^{19}$ (3 K / 150 K)	10.0 / 16.2 (3 K / 150 K)	-0.43 / 0.1 (3 K / 150 K)
Ga-LT-6%	$1.4.10^{19}$ / $1.9.10^{19}$ (3 K / 150 K)	12.1 / 18.2 (3 K / 150 K)	-0.28 (3 K)
Ga*-LT-4%	$4.2.10^{19}$ / $5.8.10^{19}$ (5 K / 300 K)	41.8 / 34.1 (5 K / 300 K)	0.18 / 0.12 (5 K / 300 K)
Ga*-LLT-10%	$3.3.10^{19}$ / $4.2.10^{19}$ (4 K / 100 K)	5.4 / 8.2 (4K / 100 K)	-0.75 / 0.065 (4K / 100 K)
Ga*-LT-10%	$3.1.10^{19}$ / $4.3.10^{19}$ (4 K / 100 K)	8.0 / 10.2 (4 K / 100 K)	-0.79 / 0.102 (4 K / 100 K)
Ga*-HT-10%	$3.0.10^{19}$ / $3.9.10^{19}$ (4 K / 100 K)	10.0 / 13.0 (4 K / 100 K)	-0.81 / 0.097 (4 K / 100 K)

Resistivity, carrier density and Hall mobility

The temperature dependence of zero-field resistivity for all Ga-GeMn samples is reported in figure 3.7. We find the zero-field resistivity increasing as the temperature decreases for all Ga-GeMn samples, which is considered as an "insulating" behavior. Actually, the resistivity and carrier concentration do not change a lot from 300 K to 4 K. This is because the very high doping-level of Mn and Ga makes (Ge,Mn) films become degenerate semiconductors close to the metal-insulator transition.

Here, we also discuss how the resistivity is affected by different growth parameters:

- *Effect of growth temperature*: In figure 3.7(a), when the growth temperature (T_g) is higher, the resistivity is lower. This is due to a higher hole mobility ($\sigma = 1/\rho = n.q.\mu$) as shown in Table 3.1.
- *Effect of surface roughness*: We can not find any obvious difference between Ga-LT-10% and Ga*-LT-10% in figure 3.7(b).
- *Effect of Mn concentration*: As the Mn concentration (acceptor) is lower (Ga-LT-6%), the resistivity is higher, figure 3.7(c). However, sample Ga*-LT-4% has very low resistivity due to very high indium contamination observed by SIMS analysis shown in figure 3.8. The results on this sample will be considered with care (see for example the analysis of the ordinary magnetoresistance below). Identifying this indium contamination lead us to clean the MBE chamber, and it is absent from other samples.

In the case of pure Ge semiconductor, the relationship between mobility and doping-level (p-type) is shown in figure 3.9. The higher doping-level of hole carriers makes the Hall mobility decreasing drastically, and normally the mobility decreases as the temperature increases. Comparing with our case, we have a very high hole density in the (Ge,Mn) film ($> 2.10^{19} cm^{-3}$), but the mobility is even lower than in pure Ge semiconductor. Moreover, the mobility in our (Ge,Mn) films increases as the temperature increases. This is probably because our material system is a nonhomogeneous semiconductor (Mn-rich nanocolumns in Ge matrix). Their magnetotransport properties are influenced by such a low Hall mobility; this will be discussed later.

To summarize, (Ge,Mn) films in Ga-GeMn samples are p-type, with a high-doping level and low Hall mobility, probably because of Ga diffusion.

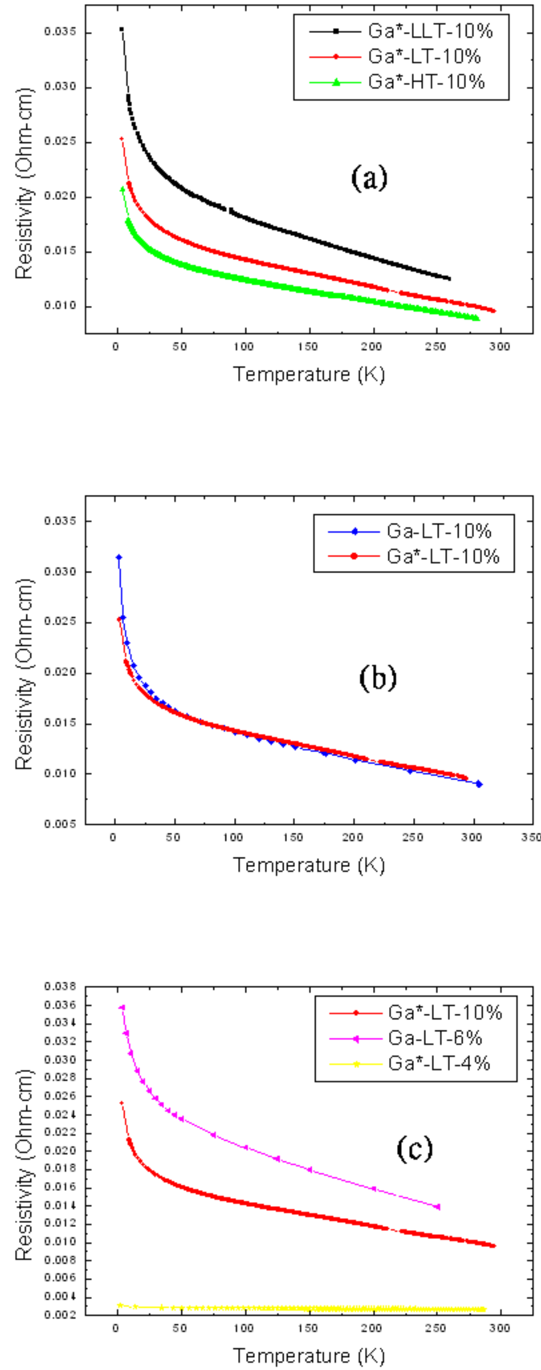

Figure 3.7: Temperature dependence of the zero-field resistivity for Ga-GeMn samples: (a) In 10% Mn samples, higher growth temperature makes (Ge,Mn) films lower resistivity (b) The curves are similar for samples with rough surface (Ga-LT-10%) and flat surface (Ga*-LT-10%), and (c) The samples with different Mn concentrations have different resistivity as a function of temperature.

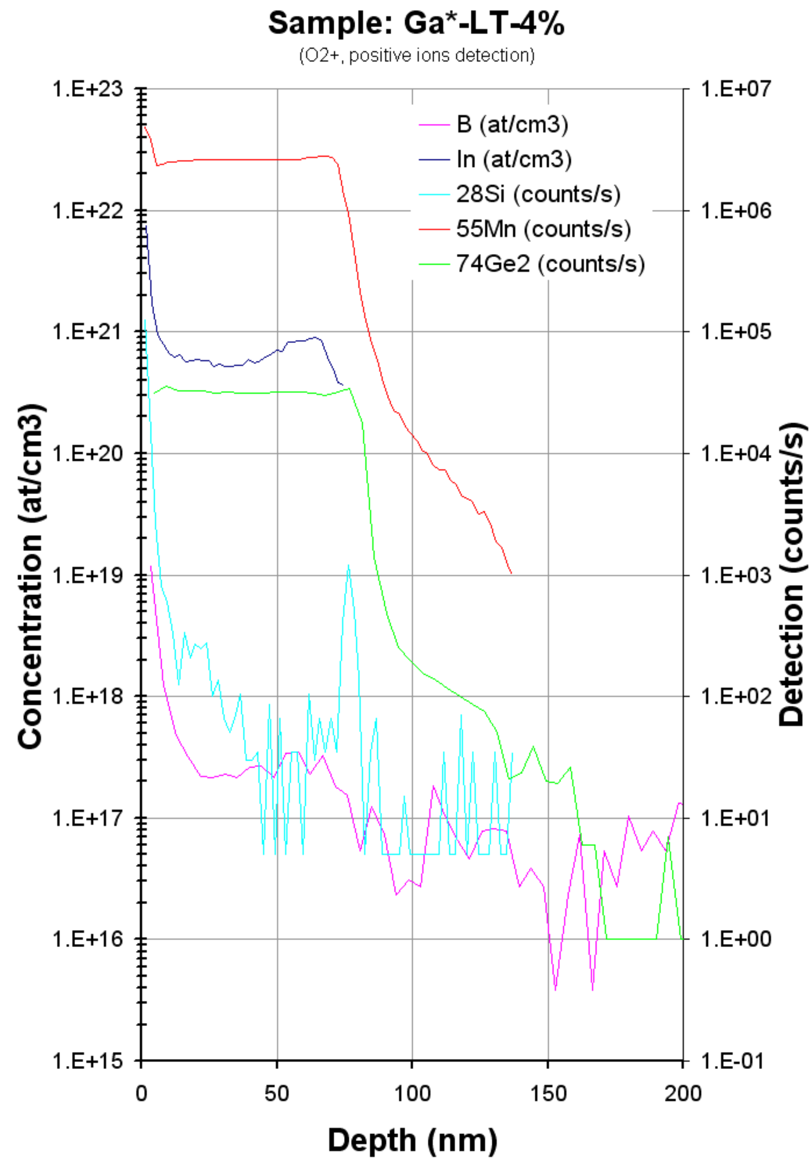

Figure 3.8: The SIMS measurement of Ga*-LT-4%: High indium concentration are observed in (Ge,Mn) film.

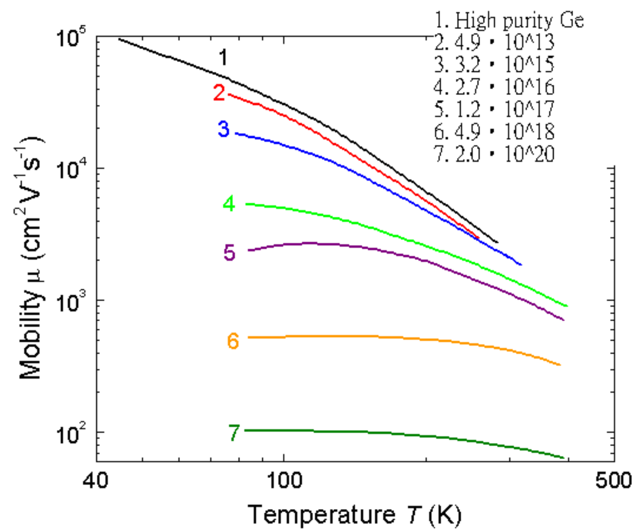

Figure 3.9: Temperature dependences of hole mobility for different doping-levels: 1. Mobility of high purity Ge is measured by time-of-flight technique, and 2-7. Mobility of different carrier density is measured by Hall-effect, N_a-N_d (cm^{-3})[67].

Hall measurements of Ga-GeMn

According to the measurement of the Hall resistance in sample Ga-LT-10%, from temperature 3 K to 150 K at magnetic field between -2 T and 2 T, shown in figure 3.10(a), we can clearly observe a non-linear part attributed to the Anomalous Hall effect. In this case, the Hall voltage depends on the magnetization, rather than on the external field. T_C is between 100 K and 125 K: above T_C there is no AHE left, just ordinary Hall effect (linear as a function of magnetic field). Moreover, we compare the Hall measurement at 3 K with the SQUID measurement at 2 K in figure 3.10(b). The behavior of Hall angle (θ_H=Atan(ρ_{xy}/ρ_{xx})) at 3 K is identical to the magnetization at 2 K. Therefore there is a clear interaction between carriers (holes) and the ferromagnetic nanocolumns.

In another sample, Ga*-LLT-10%, the Hall resistance is measured at magnetic field up to 8 T in figure 3.11(a). Hall resistance is linear at high magnetic field regime, which is ordinary Hall effect, and AHE is observed at low magnetic field below T$_C$. Because of the linear part of ordinary Hall effect, we can subtract it to have anomalous Hall resistance function of applied field in figure 3.11(b). We can find clearly the lower the temperature, the higher the anomalous Hall resistance. (*i.e.* the higher magnetization, $\rho_H = R_0H + 4\pi R_sM$). In sample Ga*-LLT-10%, anomalous Hall resistance is still visible up to 100 K. We can identify the Curie temperature of Mn-rich nanocolumn around 150 K as the result of SQUID shown in figure 3.6. Figure 3.11(c) shows the Hall angle as function of magnetic field. Finally, we compare the magnetotransport and SQUID measurements at different temperature in figure 3.11(d): Anomalous Hall resistivity is quite proportional to magnetization.

To conclude, AHE occurs in Ga-GeMn samples and disappears as the temperature is above the Curie temperature of Mn-rich nanocolumns, as identified through SQUID measurements.

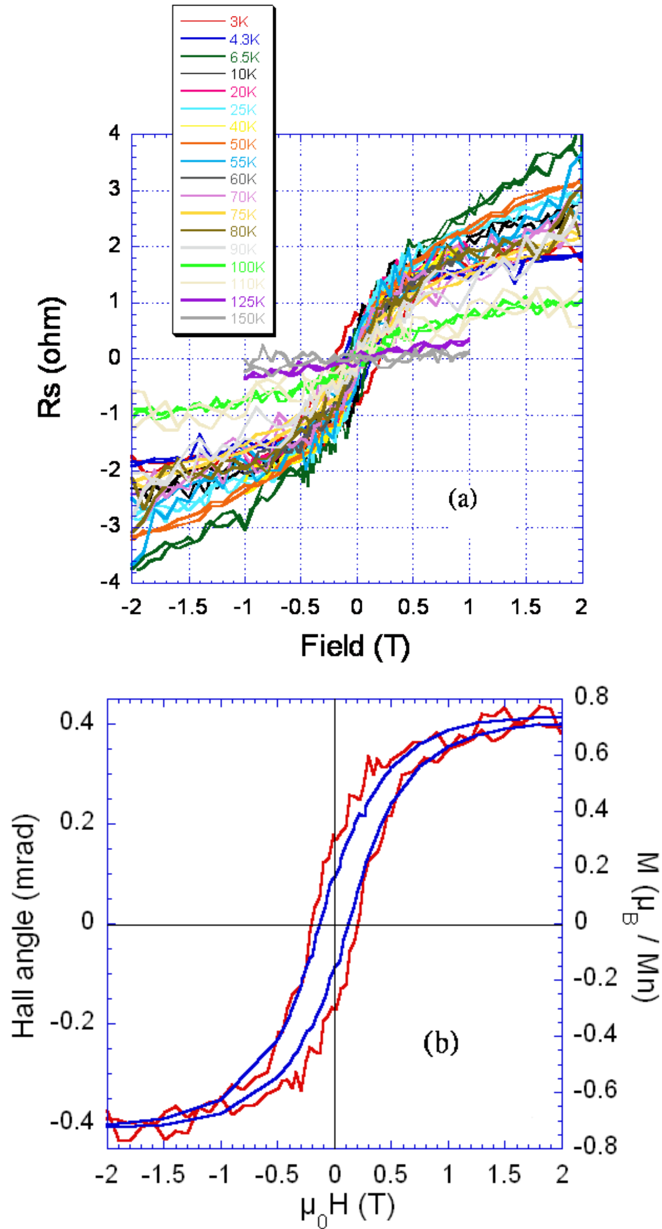

Figure 3.10: Hall measurement of Ga-LT-10%: (a) Hall resistance as a function of magnetic field is measureed at different temperatures, and (b) Anomalous Hall effect at 3 K (red) is identical to the magnetization at 2 K (blue).

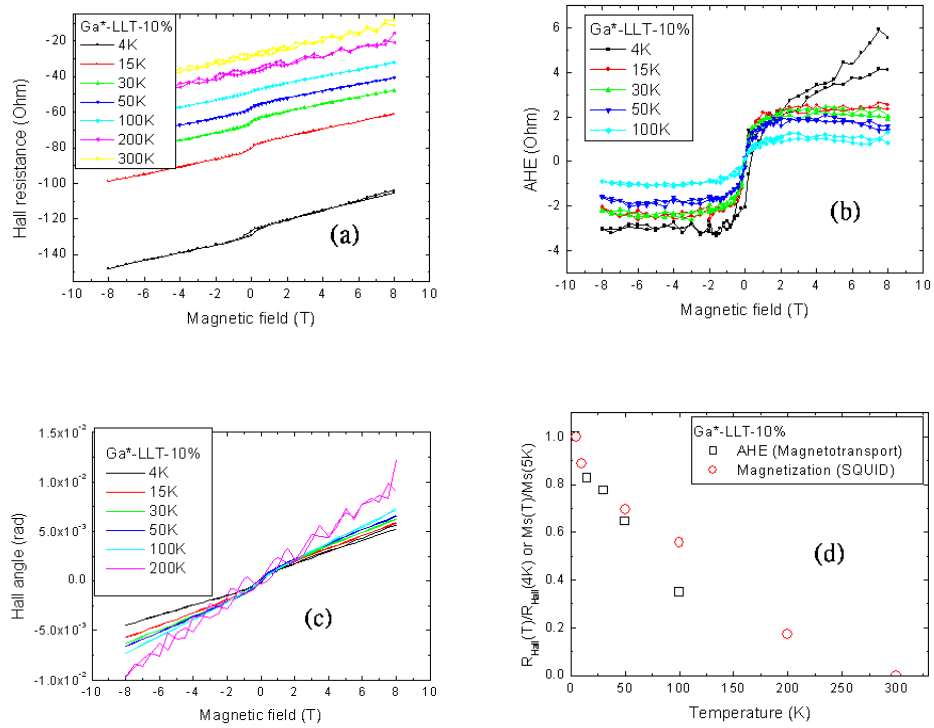

Figure 3.11: Hall measurement of Ga*-LLT-10%: (a) Hall resistance as a function of magnetic field at different temperatures , (b) Anomalous Hall resistance as a function of magnetic field, (c) Hall angle as a function of magnetic field, and (d) Comparison between AHE and magnetization.

MR measurements of Ga-GeMn

After the discussion of Hall measurements, here is another phenomenon of magnetotransport, "Magnetoresistivity"(MR). In Ga-GeMn samples, we can identify several MR behaviors at different temperature and magnetic field ranges. For example in sample Ga*-LLT-10% as shown in figure 3.12(a), we can find MR ratio from negative at low temperature to positive at high temperature.

These MR behaviors are discussed as follows:

- *Giant MR*: We attribute the effect at low temperature and low magnetic field to giant magnetoresistance (GMR), as observed in other magnetic granular systems [60]. If we take a close look at this effect at low magnetic field at 4 K, figure 3.12(b), we can observe the magnetic hysteresis. Holes move through the matrix (higher resistivity) and through the ferromagnetic Mn-rich nanocolumns (lower, spin dependent resistivity). At low temperature, the spin diffusion length (λ_{SD}) of holes in the matrix is longer than the distance between two nanocolumns. When the magnetic moments of Mn-rich nanocolumns made parallel by applying a magnetic field, some carriers experience only highly conductive nanocolumns so that the resistivity is much lower than with anti-parallel or random alignment. GMR dominates at low temperature: as the temperature increases, not only the spin diffusion length becomes shorter, but also the magnetic moment of nanocolumns decreases, so the GMR effect decreases rapidly. The absence of anisotropy is consistent with GMR effect (not shown). However, the absence of saturation even at high field (8 T, see figure 3.12(a)), is surprising: we tentatively ascribe this effect to the presence of superparamagnetic parts in the film.

- *Ordinary MR*: At temperature 15 K and 30 K, MR mixes the positive and negative parts, see figure 3.12(c). As the temperature is high enough, the MR ratio becomes positive, and its value is very small. At the magnetic field higher than 1.5 T, we can find a MR parabolic as a function of magnetic field (the fitting curve in figure 3.12(c)). We attribute this to Ordinary MR (OMR) and we will discuss it later.

- *Hall MR*: Meanwhile, we can find a special MR which saturates at magnetic field (around 1.5 T), which we propose to call Hall MR (HMR). By subtracting the parabolic OMR, we can obtain HMR as a function of magnetic field shown in figure 3.12(d). As will be shown in last part of this chapter, it is due to the presence of AHE in the nanocolumns.

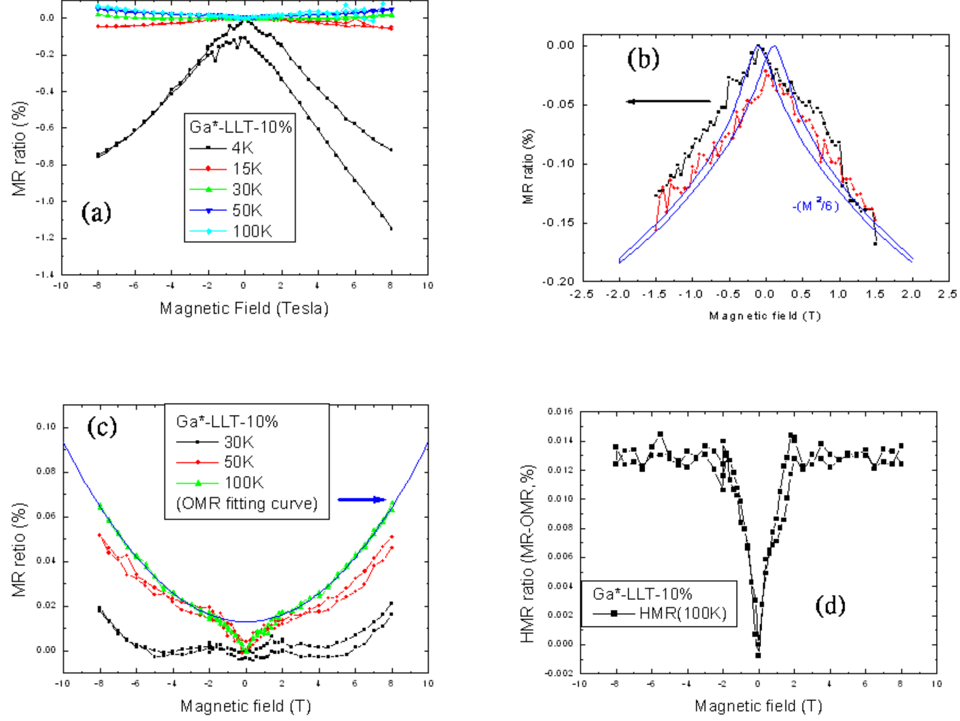

Figure 3.12: MR measurement of Ga*-LLT-10%: (a) The MR ratio changes form negative at low temperature to positive at high temperature, (b) GMR effect occurs at temperature 4 K with magnetic hysteresis; black and red arrows indicate the change direction of applied field, (c) Positive MR at higher temperature is made of OMR effect (at all magnetic field range) and HMR effect (just at low field range), (d) HMR is obtained by subtracting the parabolic OMR.

Moreover MR measurements in sample Ga-LT-10% are shown in figure 3.13. Because we have more measuring temperatures, we can identify more precisely the different MR regimes as a function of temperature. For T> T_C (around 125 K) or at high magnetic fields, MR is parabolic which corresponds to ordinary magnetoresistance. For T_C> T> T_B (around 15 K), MR shows a linear behaviour at low magnetic field, and this corresponds to HMR. Finally, for T≤ T_B, we observe negative MR which might be attributed to GMR.

MR results in sample Ga-LT-10% compare with the other samples as follows:

- *GMR*: Ga-LT-10% sample has weaker GMR effect, which disappears

earlier and saturates around 5 T. It would be interesting to know whether this weaker value might be due to non-parallel nanocolumns in this film.

- *HMR*: HMR effect is similar to that in Ga*-LLT-10% samples.
- *OMR*: OMR effect can be observed at all temperature ranges (from 3 K at high field to 250 K). Above the T_C, we just find OMR effect.

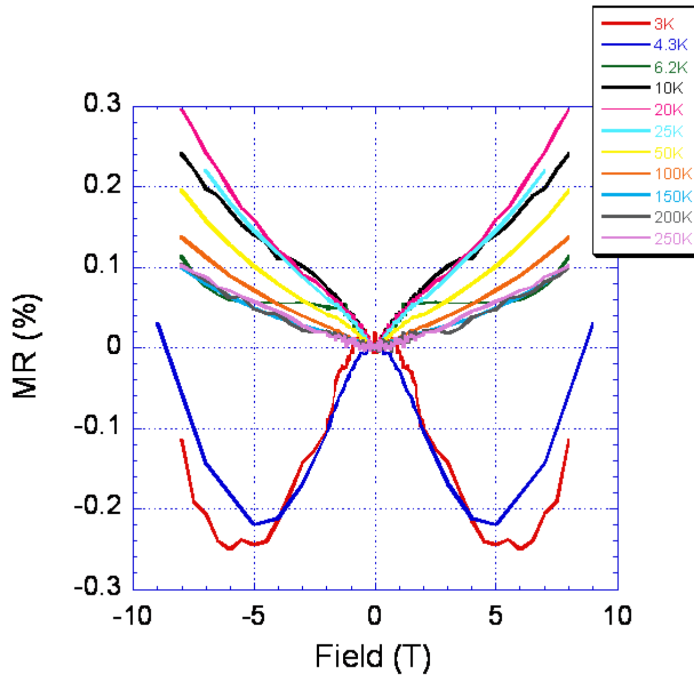

Figure 3.13: MR ratio of Ga-LT-10% is measured at different temperatures from 3 K to 250 K.

Finally we would like to discuss the OMR effect as a function of Hall mobility. OMR is a parabolic function of magnetic field ($\propto B^2$), so we fix the magnetic field at 8 T in order to investigate the relationship between the Hall mobility and OMR ratio in Ga-GeMn and p-type As-GeMn samples (reported in next section). And then, we plot the OMR ratio as function of Hall mobility (μ^2) in figure 3.14. We find that OMR ratio is proportional to $(\mu \cdot B)^2$ in all samples. The only exception is Ga*-LT-10%, which is probably affected by the high indium content. This confirms our interpretation of this contribution to MR as OMR.

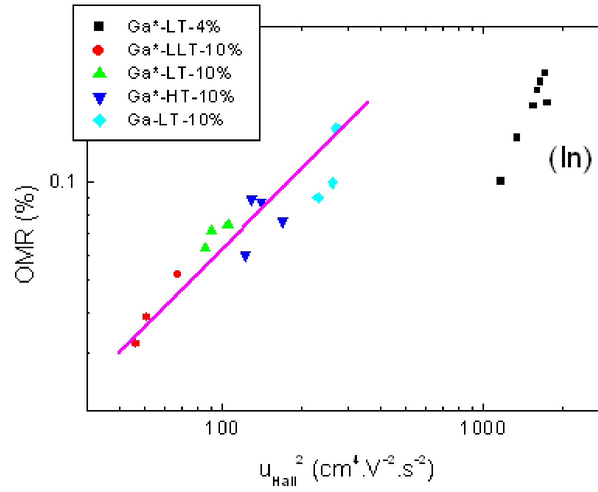

Figure 3.14: OMR ratio is proportional to $(\mu)^2$ in Ga-GeMn samples.

To summarize this section, we identify these mechanisms in Ga-GeMn samples:

- ***OMR**, characterized by its $(\mu \cdot B)^2$ behavior,*
- ***GMR**, as in other non-homogeneous system,*
- ***HMR**, a new mechanism related to AHE, which will be discussed later in this chapter.*

3.2 As-GeMn samples

In this section, we discuss another group of samples, *As-GeMn*. We use the GaAs(001) substrate protected by amorphous arsenic capped layer to grow As-rich (Ge,Mn) thin films, which is another way to have a very flat GaAs surface for (Ge,Mn) growth. After the growth, there are also the study of their microstructure by TEM, element composition analysis by SIMS, magnetic properties by SQUID, and magnetotransport properties.

Instead of self-organized nanocolumns in Ga-GeMn samples, randomly distributed nano-precipitates are present in these (Ge,Mn) films, and so do Ge_3Mn_5 nanoclusters especially for higher growth temperature. Therefore, three magnetic phases are observed; the magnetotransport properties are heavily influenced by Arsenic impurities: compensation effect between donors and acceptors, highly anisotropic magnetoresistance behaviors and weak localization of electron transport.

3.2.1 3D nano-precipitate growth

To grow As-GeMn samples, semi-insulating GaAs(001) wafer is covered with a thin undoped GaAs buffer protected with an amorphous As capped layer in a separate III-V epitaxy MBE system. In our IV-IV MBE machine, we remove the arsenic capped layer at 200°C in order to prepare a very flat, As-rich GaAs surface, with (2×4) RHEED reconstruction; then we grow 80 nm (Ge,Mn) films with different Mn concentrations (2%, 6% and 10%) at different temperatures (100°C and 110°C). Samples grown by this preparation method will be designated as As-LT-2% (T_g=100°C), As-LT-6%, As-HT-6% (T_g=110°C) and As-LT-10%.

After (Ge,Mn)films growth, SIMS technique is employed to analyze chemical elements and their distribution. We can clearly find that (Ge,Mn) samples contain a large amount of arsenic atoms up to 10^{19} at./cm^3 with a surface rich profile shown in figure 3.15. This arsenic incorporation in (Ge,Mn) films is in agreement with the well-known surfactant effect of As during the growth of Ge on GaAs surfaces[64] leading to an As-rich surface and As atoms incorporation. This effect changes the growth mechanism of (Ge,Mn) films, causes the n-type doping for transport, and also influences their magnetism as well as magnetotransport properties reported in the following sections.

In the beginning, we expected the growth of (Ge,Mn) films with such flat GaAs substrate surface for the parallel Mn-rich nanocolumns along ⟨001⟩ di-

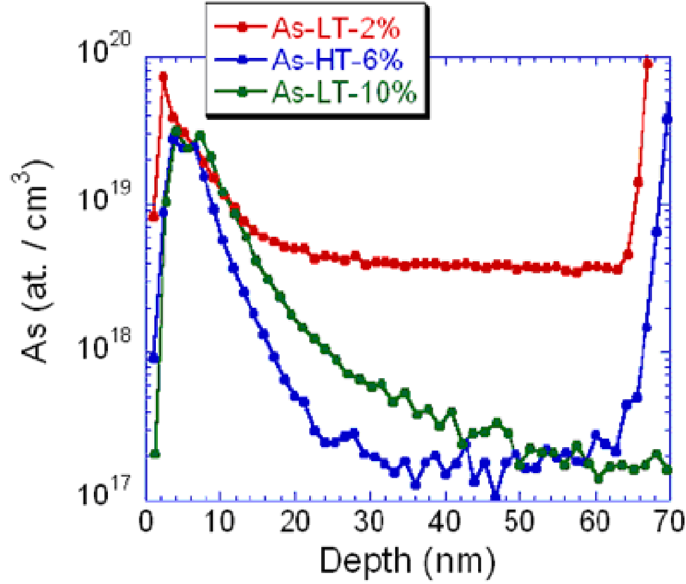

Figure 3.15: SIMS measurements of As-LT-2%, As-HT-6% and As-LT-10%: we find high As concentration in the (Ge,Mn) film, especially in the upper layer of (Ge,Mn).

rection. However, from the observation of TEM images, we can find the Mn-rich nano-precipitates randomly distribute in (Ge,Mn) film, figure 3.16(a), and these around 3 nm precipitates are fully coherent with the diamond germanium lattice by HRTEM shown in figure 3.16(b) in sample As-LT-2%. Moreover, for the sample As-HT-6% grown at higher temperature, some Ge_3Mn_5 clusters start to form, and the Moiré contrasts are visible due to these clusters in figure 3.17(a) and (b). In brief, these As-rich GaAs surfaces not only change the growth mechanism of (Ge,Mn) films but also make Ge_3Mn_5 clusters appear easily.

The presence of As near the surface of the growing layer offers a possible explanation for this change of character of the spinodal decomposition, from nanocolumns to 3D nano-precipitates. According to Ref.[69], in GeMn material system, Mn atoms are incorporated into germanium in a subsurface interstitial position, and further diffusion within the growth plane: this offers a growth mechanism for 2D spinodal decomposition[26]. However, codoping with arseic element changes the charge state of Mn atoms in Ge matrix, thus reducing Coulomb repulsion and enhancing the effect of attractive Mn-Mn pair interaction, making the nucleation of Mn-rich precipitates easier[66].

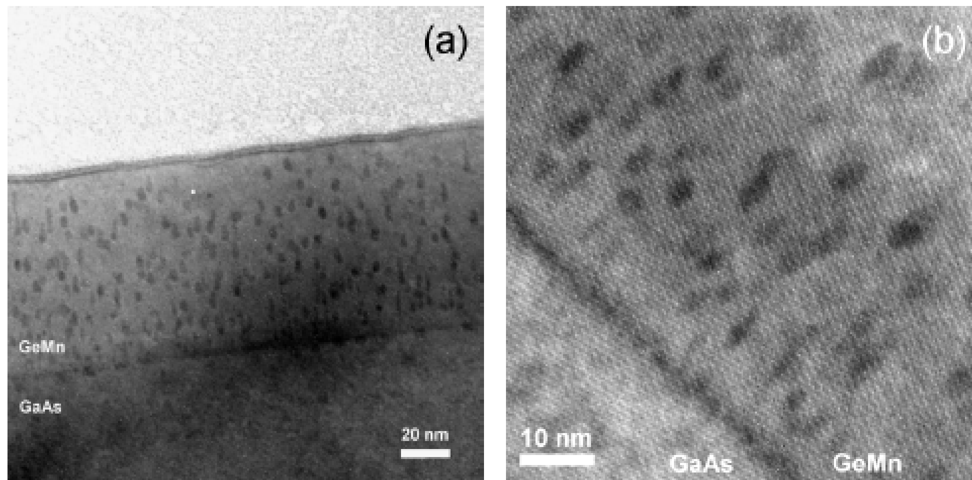

Figure 3.16: (a) Cross-section TEM image of a 80 nm (Ge,Mn) film, As-LT-2%, and (b) High Resolution TEM image shows Mr-rich coherent precipitates.

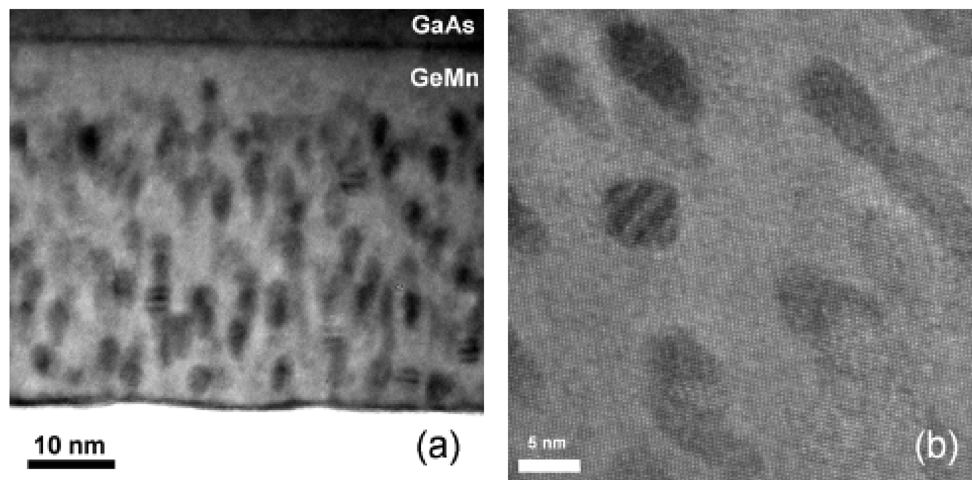

Figure 3.17: (a) Cross-section TEM image of a 80 nm Ge,Mn) film, As-HT-6%, and (b) High Resolution TEM image shows Mr-rich coherent precipitates as well as Moiré contrast due to the present of Ge_3Mn_5 clusters

Besides, the presence of donors like arsenic is expected to displace the equilibrium between interstitial Mn (another donor) and substitutional Mn (an acceptor), enhancing the amount of substitutional Mn (which from nucleation centers for further Mn aggregation)[68], and reducing the amount of interstitial Mn (thus decreasing the incorporation into already existing clusters). These different mechanisms induced by the presence of As conspire to

favor a growth process dominated by nucleation, contributing to make the spinodal decomposition 3D.

To sum up this section, 3D Mn-rich nanoprecipitates and Ge_3Mn_5 clusters are grown in (Ge,Mn) films for all As-GeMn samples. Two effects of the arsenic may explain this observation: the arsenic surfactant effect, may be also its donor character.

3.2.2 Magnetic properties of As-GeMn

In this part, we report the magnetic measurements on As-GeMn samples and also compare with Ga-GeMn samples. By using the same analyzing method as sample Ga-LT-10% in section 3.1.2, SQUID measurements clearly show the presence of three different magnetic phases in this group of samples: paramagnetic Mn atoms diluted in Ge matrix, a low-T_C (50 K) magnetic phase attributed to Mn-rich precipitates, and ferromagnetic Ge_3Mn_5 clusters.

In samples As-LT-2% (figure 3.18(c)) and As-LT-6% (figure 3.19(c)), the magnetic remanence as a function of temperature exhibits a strong decrease up to 50 K and no magnetic signal above. However in saturation magnetization (shown in figure 3.18(d)) and ZFC-FC curves (shown in figure 3.19(f)), a field induced magnetic signal remains up to 300 K. This magnetic signal is thus attributed to superparamagnetic Ge_3Mn_5 clusters (even though we cannot completely exclude the presence of MnAs precipitates because we see the SIMS result in the previous section that (Ge,Mn) films grown on As-rich surfaces contain a sizeable amount of As atoms.) In samples As-HT-6% and As-LT-10%, we observe almost the same magnetic behavior except that the magnetic remanence remains positive up to 300 K. Therefore, increasing the growth temperature or Mn concentration results in the formation of Ge_3Mn_5 (or MnAs) clusters ferromagnetic up to 300 K within the (Ge,Mn) film. Increasing the growth temperature leads to larger clusters and hence a higher average blocking temperature whereas increasing the Mn content leads to a broader size distribution in agreement with TEM observations.

The low temperature peak in ZFC curves corresponds to superparamagnetic Mn-rich precipitates (shown in figure 3.19(f), figure 3.20(f), and figure 3.21(f)), the peak maximum giving their average blocking temperature T_B. T_B values of all samples are listed in Table 3.3. At T_B, we also observe a kink in the temperature dependence of magnetic remanence. Indeed, up to $T = T_B$ most of the ferromagnetic Mn-rich precipitates become superparamagentic and the magnetic remanence decreases rapidly. For $T_B > T > T_C$, only remains the magnetic signal from the biggest ferromagnetic Mn-rich precipitates become superparamagnetic and the magnetic remanence decreases more slowly. Above $T = T_C$=50 K, the magnetic signal from Mn-rich precipitates becomes negligible.

In As-GeMn samples, by subtracting from the total magnetization curve a 3/2-Brillouin function (magnetic signal from the matrix with diluted Mn atoms), we have the magnetization without matrix signal as function of ap-

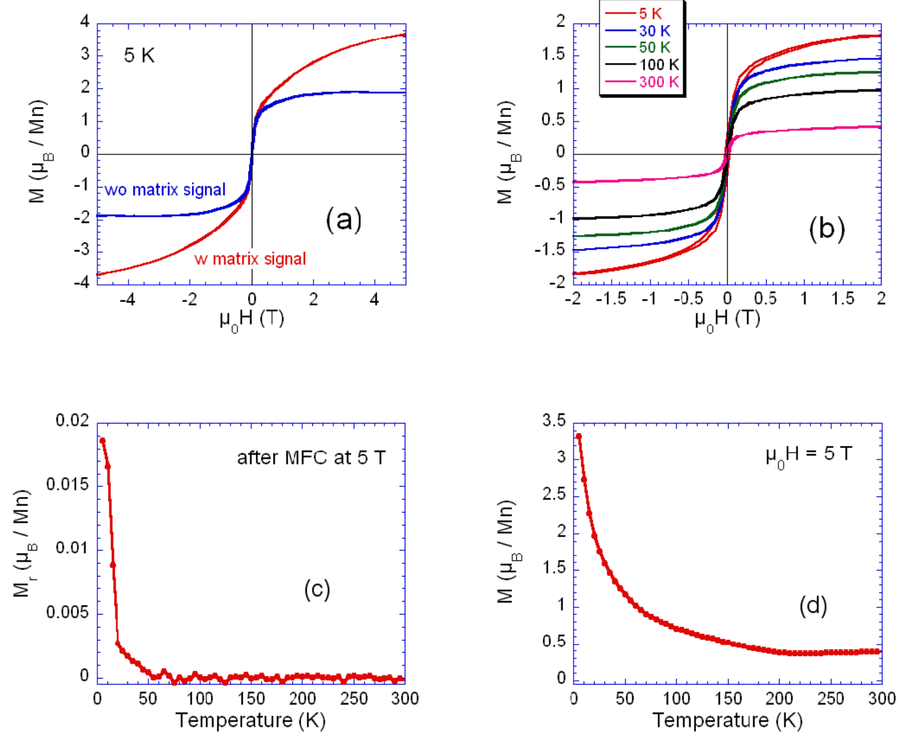

Figure 3.18: Magnetic measurements performed on As-LT-2% sample. (a) Magnetization curve recorded at 5 K with and without the paramagnetic signal from diluted Mn atoms. (b) Magnetization curves as a function of temperature. The matrix signal has been subtracted for each temperature. (c) Magnetic remanence as a function of temperature recorded after maximum field cooling (MFC) at 5 T. (d) Temperature dependence of the saturation magnetization recorded at 5 T.

plied magnetic field at 5 K, which is made of two other magnetic phases (precipitates and clusters) in figure 3.18(a), figure 3.19(a), figure 3.20(a), and figure 3.21(a). Therefore, we can separate two magnetic signals of precipitates and clusters at temperature above 50 K, assuming that the saturation magnetization of Ge_3Mn_5 clusters remains constant from 5 K to 100 K. Using this procedure, we find the relative magnetic contributions of each phase, as listed in Table 3.2. Moreover, in order to have average magnetic moment of each phase, we use a Langevin equation to fit the magnetization curves in the temperature range between T_B and T_C as shown in Table 3.3.

From the results in Table 3.2 and Table 3.3, we can make some conclusions:

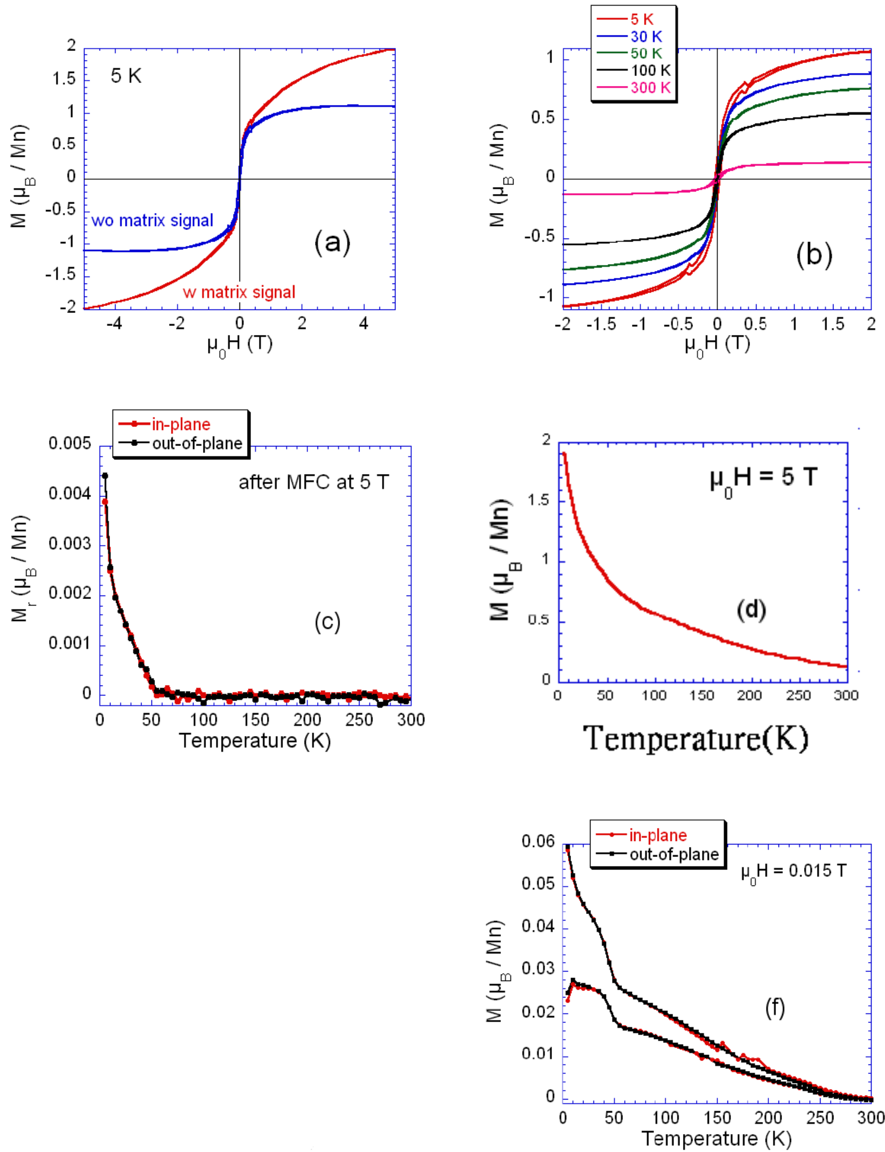

Figure 3.19: Magnetic measurements performed on As-LT-6% sample. (a) Magnetization curve recorded at 5 K with and without the paramagnetic signal from diluted Mn atoms. (b) Magnetization curves as a function of temperature. The matrix signal has been subtracted for each temperature. (c) In-plane and out-of-plane magnetic remanence as a function of temperature recorded after maximum field cooling (MFC) at 5 T. (d) Temperature dependence of the saturation magnetization recorded at 5 T. (f) ZFC-FC curves recorded in-plane and out-of-plane at 0.015 T.

Table 3.2: Magnetic contributions (in %) from the Ge matrix, Mn-rich precipitates and Ge_3Mn_5 clusters. The Mn concentration in the Ge matrix is further given assuming a columns or precipitates volume fraction between 0 % and 10 %.

Samples	Magnetic composition (%)			%Mn in Ge matrix
	matrix	precipitates	Ge_3Mn_5	
Ga-LT-10%	60±6	40±4	-	3.6±0.2 %
As-LT-2%	55±3	21±2	24±2	1.65±0.15%
As-LT-6%	50±4	24±2	26±3	2.35±0.15%
As-HT-6%	52±3	22±2	26±2	2.35±0.15%
As-LT-10%	47.5±3	11.5±0.7	41±3	2.25±0.15%

Table 3.3: In these three columns are reported the blocking temperature (T_B), magnetic moment per Mn atom and magnetic size (estimated at T=30 K) of Mn-rich columns or precipitates.

Samples	Mn-rich precipitates		
	T_B (K)	mag. moment /Mn (μ_B)	magnetic size (μ_B)
Ga-LT-10%	15±5	1.0±0.1	520±50
As-LT-2%	20±5	-	100±40
As-LT-6%	10±5	1.4±0.2	140±20
As-HT-6%	15±5	1.2±0.2	105±20
As-LT-10%	15±5	0.3±0.03	50±20

- For higher growth concentration of Mn, the magnetic signal of Ge_3Mn_5 clusters becomes higher. Ge_3Mn_5 phase appears more easily at higher Mn concentration and higher growth temperature.

- The Mn concentration in Ge matrix is less in As-GeMn (≈ 2%) than in Ga-GeMn (≈ 3.6%). That is because As improves the diffusion of Mn to nucleate Mn-rich precipitates and Ge_3Mn_5 clusters.

- In comparison with As-LT-6% and As-HT-6%, higher growth temperature makes the blocking temperature (T_B) and size of Ge_3Mn_5 clusters increase, which is in agreement with TEM observations.

- The magnetic moment per Mn atom in the precipitates is around $1\mu_B$. However, As-LT-10% drops down to $\approx 0.3\mu_B$ probably due to antiferromagnetically coupled Mn spin within Mn-rich precipitates.

For the study of magnetic anisotropy in As-GeMn, we investigate the samples As-LT-6%, As-HT-6% and As-LT-10% by measuring in-plane and

out-of-plane ZFC-FC curves. In As-LT-6%, we also measure in-plane and out-of-plane magnetic remanence.

- *In samples As-LT-6% and As-LT-10%*, in the resolution limit of our SQUID, in-plane and out-of-plane magnetic remanence and/or ZFC-FC curves nearly superimpose meaning that magnetic anisotropy is very weak in these (Ge,Mn) films. Moreover Ge_3Mn_5 clusters are actually superparamagnetic in the whole temperature range since ferromagnetic Ge_3Mn_5 clusters always exhibit out-of-plane anisotropy[63]. However if we take a closer look at low temperature magnetic signals (below the average blocking temperature of Mn-rich precipitates), out-of-plane curves are slightly above in-plane ones but we cannot unambiguously ascribe this out-of-plane magnetic anisotropy to Mn-rich precipitates since some Ge_3Mn_5 clusters may also be ferromagnetic at these low temperatures.

- *In sample As-HT-6%*, we clearly observe out-of-plane anisotropy. The in-plane blocking temperature is too weak to be measured whereas the out-of-plane blocking temperature equals 100 K (see figure 3.20(f)). Using the standard equation: $KV = 25k_BT_B$, where K=4.2.10^5 J/m^3, V and T_B are the magnetic anisotropy constant of bulk Ge_3Mn_5[65], cluster volume and blocking temperature respectively, we obtain an average diameter of Ge_3Mn_5 clusters 5.4 nm, which is in very good agreement with the size of Moiré contrast areas in TEM pictures (figure 3.17). Due to the strong out-of-plane anisotropy of Ge_3Mn_5 clusters we could not conclude about the magnetic anisotropy and size of Mn-rich precipitates from ZFC-FC curves.

To summarize the study of magnetic anisotropy, the magnetic anisotropy of Mn-rich nanostructures in (Ge,Mn) films grown on GaAs(001) substrates remains very weak which fully justifies the initial assumption that magnetic nanostructures saturate below 5 T.

To sum up this section, in As-GeMn samples, three magnetic phases are observed by SQUID measurement such as paramagnetic Mn atoms diluted in Ge matrix, a low-T_C (50 K) magnetic phase attributed to Mn-rich precipitates, and ferromagnetic Ge_3Mn_5 clusters.

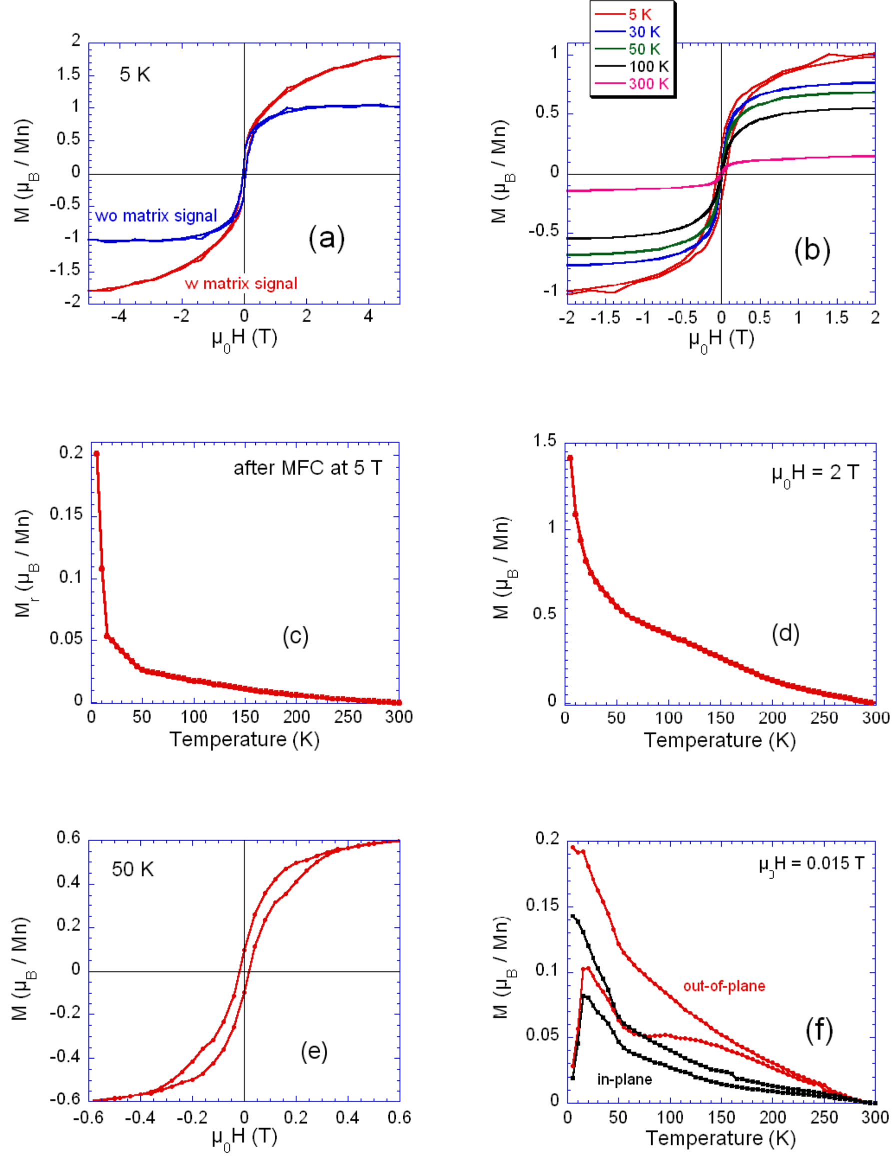

Figure 3.20: Magnetic measurements performed on As-HT-6% sample. (a) Magnetization curve recorded at 5 K with and without the paramagnetic signal from diluted Mn atoms. (b) Magnetization curves as a function of temperature. The matrix signal has been subtracted for each temperature. (c) Magnetic remanence as a function of temperature recorded after maximum field cooling (MFC) at 5 T. The non-zero magnetic signal above 50 K corresponds to ferromagnetic Ge_3Mn_5 clusters up to 300 K. (d) Temperature dependence of the saturation magnetization recorded at 2 T. (e) Out-of-plane magnetization curve recorded at 50 K. At this temperature, we only measure the magnetic signal from both superparamagnetic and ferromagnetic Ge_3Mn_5 clusters. (f) ZFC-FC curves recorded in-plane and out-of-plane at 0.015 T.

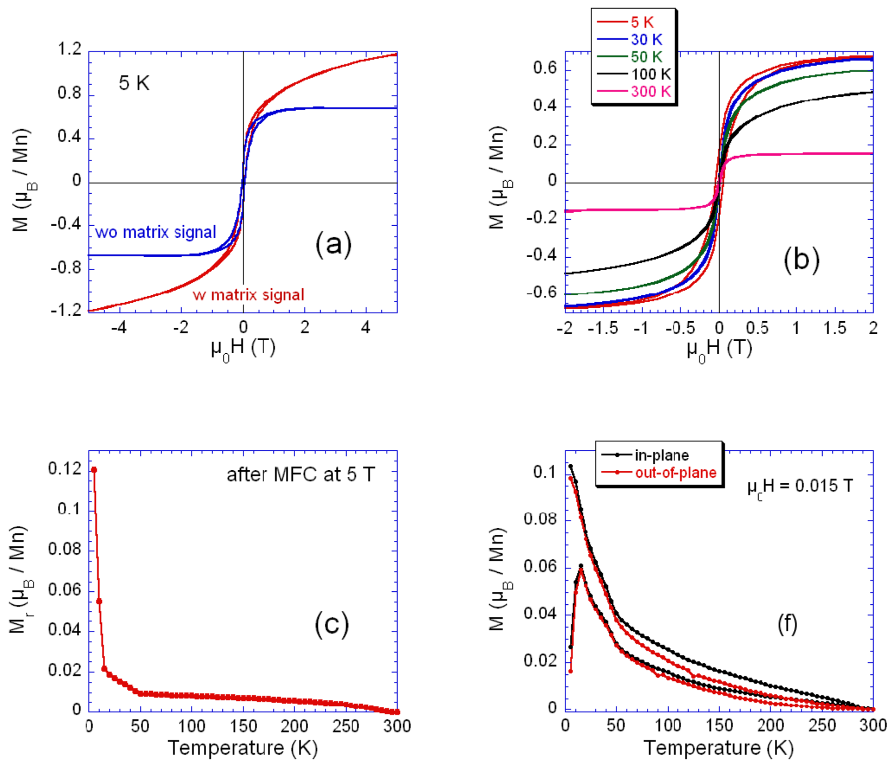

Figure 3.21: Magnetic measurements performed on As-LT-10% sample. (a) Magnetization curve recorded at 5 K with and without the paramagnetic signal from diluted Mn atoms. (b) Magnetization curves as a function of temperature. The matrix signal has been subtracted for each temperature. (c) Magnetic remanence as a function of temperature recorded after maximum field cooling (MFC) at 5 T. (f) ZFC-FC curves recorded in-plane and out-of-plane at 0.015 T.

3.2.3 Magnetotransport of As-GeMn

In this part, we report the magnetotransport measurement of As-GeMn samples. Because large amount of Arsenic atoms are in the (Ge,Mn) films especially for the upper layer of (Ge,Mn) films reported in section 3.2.1, their transport properties are heavily influenced by As. The compensation effect between As as donor and Mn as acceptor makes their transport properties have two groups; one has very high resistivity in high Mn concentration samples, and the other is n-type doping (Ge,Mn) film with very low resistivity which also has very interesting magnetotransport properties such as Anisotropic magnetoresistance (AMR), weak localization and Tunneling magnetoresistance (TMR).

Compensation effect

Arsenic acts as shallow donor (its ionization energy is 14 meV) in germanium and is responsible for the strong compensation effects with Mn acceptors. Consequently, As-GeMn samples exhibit lower hole densities close to the threshold for the metal-insulator transition (MIT) in As-LT-6% and As-LT-10% and n-type doping well above the MIT threshold for low Mn concentrations in As-LT-2% and As-HT-6%. Increasing the Mn content up to 10%, we indeed recover p-type doping. As Table 3.4 shows, As-GeMn samples can be divided into two distinct groups owing to their different electrical properties.

Table 3.4: Carrier density and Hall mobility of As-GeMn samples. The Hall mobility is defined as μ_H=R_H/ρ_0 where R_H is the Hall constant and ρ_0 the zero field resistivity. Sample thickness is 80nm even the nonuniformity of As in (Ge,Mn) films

Samples	carrier density (cm^{-3})	Hall mobility ($cm^2.V^{-1}.s^{-1}$)	doping type
As-LT-2%	$7.8.10^{18}$ / $1.1.10^{19}$ (5 K / 200 K)	21.8 / 20.5 (5 K / 200 K)	n
As-LT-6%	$4.8.10^{17}$ (300 K)	48.9 (300 K)	p
As-HT-6%	$8.9.10^{18}$ / $1.3.10^{19}$ (5 K / 200 K)	14.9 / 14.6 (5 K / 200 K)	n
As-LT-10%	$4.7.10^{17}$ / $6.2.10^{17}$ (150 K / 300 K)	6.5 / 50.1 (150 K / 300 K)	p

First, samples As-LT-6% and As-LT-10% are semi-insulating and have

very low hole densities close to the Mott critical concentration (Table 3.4). The zero-field resistivity can not be measured below temperature 50 K due to the insulating character of these (Ge,Mn) films. In figure 3.22(a), we can find the resistivity become very high as the temperature decreases. In these samples, the magnetotransport measurements are limited to high temperatures, and positive MR exhibits low values as expected from orbital MR in figure 3.22(b). We have compared their OMR with Ga-GeMn samples in figure 3.23. We obtain a rather good agreement, except for the data at low mobility. This point was taken at low temperature, and Table 3.4 reports a strange behavior of the mobility at low temperature in this sample, which suggests that it is quite inhomogeneous.

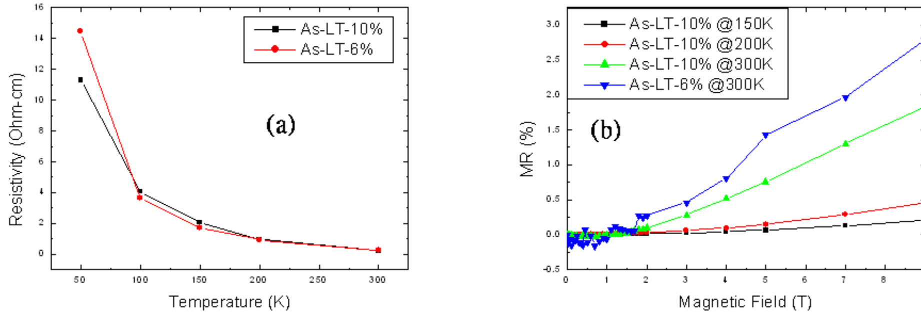

Figure 3.22: P-type As-GeMn samples (As-LT-6% and As-LT-10%): (a) Zero-field resistivity as function of temperature; their resistivities are very high and incerase very quickly as the temperature decreases, (b) Positive MR comes from OMR effect at temperature above 150 K.

In the second group of As-GeMn samples (As-LT-2% and As-HT-6%), (Ge,Mn) films are degenerate semiconductors with high n-type doping in Table 3.4. Zero-field resistivity is of order of $10^{-2}\Omega.cm$ and remains finite down to very low temperature shown in figure 3.24(a). Moreover, these samples exhibit a pronounced negative MR at low temperatures as shown in figure 3.24(b) for As-LT-2% and in figure 3.24(d) for As-HT-6%. If we suppose the electron transport just takes place in the As-rich layer which is around 10nm from SIMS measurement, we can find their carrier concentration very high close to 10^{20} cm^{-3} as shown in Table 3.5. For the Hall measurement, ordinary Hall effect is obtained as shown in figure 3.24(c). We can not find AHE in these samples since spin-orbital scattering is small for electrons in the conduction band of germanium, and also because of the formation of

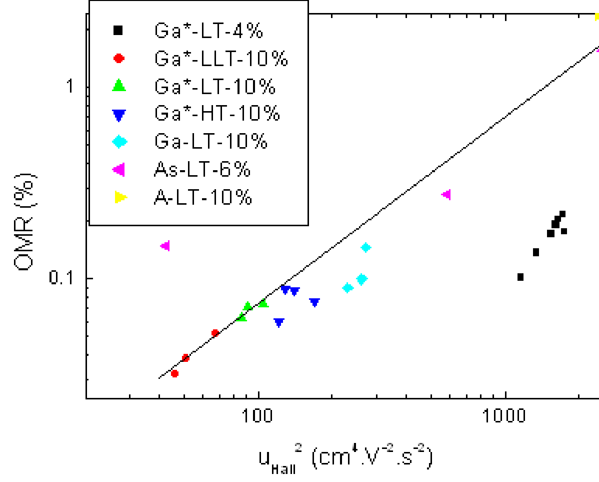

Figure 3.23: OMR effect is observed and proportional to μ^2 in all p-type samples.

Schottky barrier in n-type (Ge,Mn) samples (discussed in next section).

Table 3.5: For n-type As-GeMn samples, we suppose the thickness of electron transport is 10 nm because the high Arsenic concentration in the upper layer of (Ge,Mn)

Samples	carrier density (cm^{-3})	Hall mobility ($cm^2.V^{-1}.s^{-1}$)
As-LT-2%	$6.2.10^{19}$ / $8.8.10^{19}$ (5 K / 200 K)	21.8 / 20.5 (5 K / 200 K)
As-HT-6%	$7.1.10^{19}$ / $1.0.10^{20}$ (5 K / 200 K)	14.9 / 14.6 (5 K / 200 K)

To summarize, compensation effect between As and Mn makes two groups of sample: high-resistivity p-type (Ge,Mn) films with positive MR and low-resistivity n-type (Ge,Mn) films with negative MR. No AHE occurs in the n-type (Ge,Mn) films.

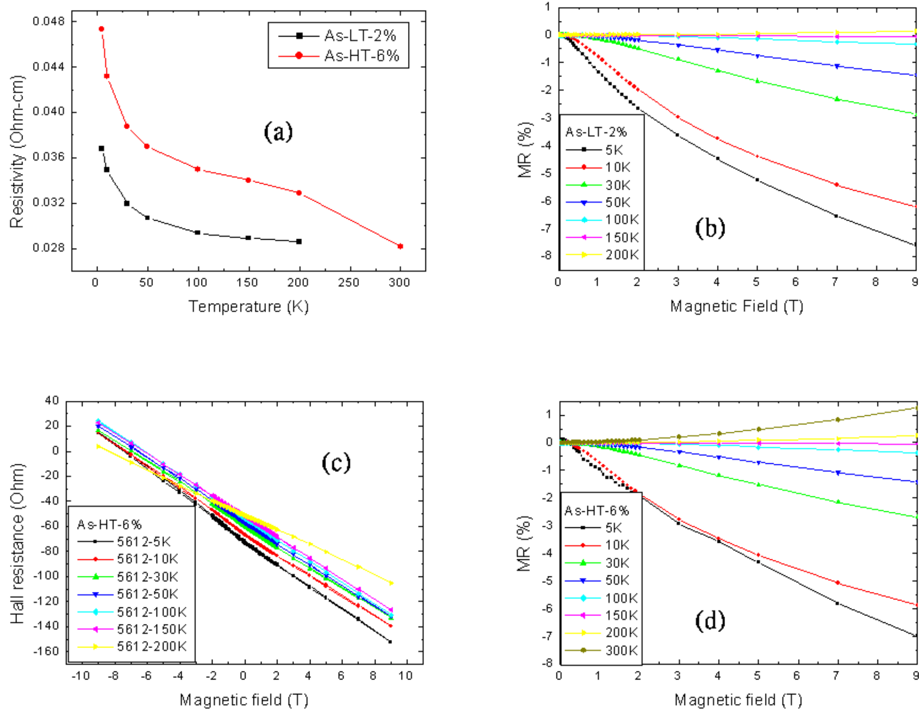

Figure 3.24: N-type As-GeMn samples, (a) Zero-field resistivity as a function of temperature in As-LT-2% and As-HT-6% samples, (b) Magnetoresistance measurement of As-LT-2%; we find a high negative MR ratio as a function of field. (c) Hall measurement of As-HT-6%; normal Hall effect is observed in n-type samples (d) Magnetoresistance as a function of field in As-HT-6%.

Anisotropic magnetoresistance

In these n-type samples, we further performed angular dependent MR measurements by rotating the external field from in-plane (θ=0°) to out-of-plane (θ=90°) as shown in figure 3.25(a) for As-LT-2% and figure 3.25(b) for As-HT-6%. We obtained similar results for both samples at low temperature:

- A strong anisotropy : we will show below that this is well accounted for by the calculation of weak localization effects in the 2D layer induced by As-diffusion. We will show also that this contribution vanishes at θ=0°.
- An isotropic part (measured at θ=0°) which we tentatively attribute to tunneling magnetoresistance (TMR).

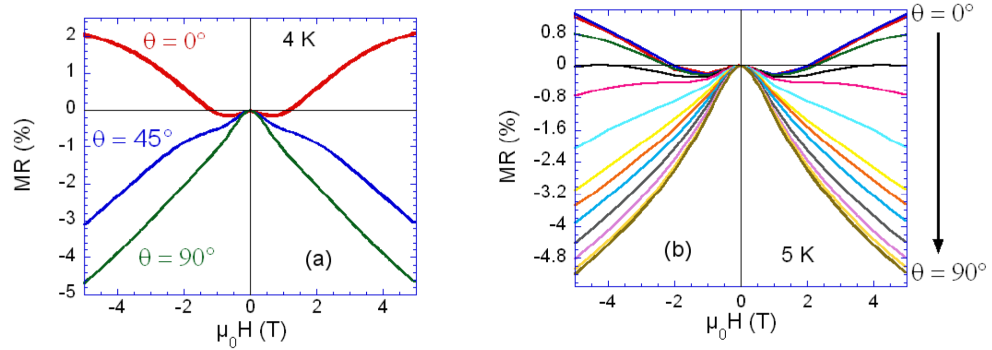

Figure 3.25: AMR measurement (a) In As-LT-2%, magnetoresistance recorded at 4 K and different angles: θ=0°, 45°, and 90°, (b) In As-HT-6%, magnetoresistance recorded at 5 K and different angles from θ=0° to 90°.

In sample As-HT-6%, magnetic field and temperature dependence of the anisotropy of MR is shown in figure 3.26. As electron transport scattering is very strong, and the wavelength of the electrons is close to the mean free path ($k_F\lambda \approx 1$), the spherical wave from the scattering event can interfere with the incoming spherical wave. This quantum interference leads to 2D weak localization which is described by the following equations:

$$\frac{\Delta\rho}{\rho} \approx -\frac{\Delta\sigma}{\sigma} = -A.f_2\left[\frac{4e\mu_0 H sin(\theta) L_\phi}{\hbar}\right] \tag{3.1}$$

$$A = e^2/2\pi^2\hbar\sigma_{2D}(0) \tag{3.2}$$

$$f_2(x) = ln(x) + \Psi(\frac{1}{2} + \frac{1}{x}) \tag{3.3}$$

Here, L_ϕ is the phase relaxation length, the function $f_2(x)$ is defined in Ref [71] and Ψ is digamma function. In this expression, we have neglected spin-orbit scattering: the spin-orbit time is much longer than the electron phase relaxation time: $\tau_{SO}>>\tau_\phi$. This assumption relies on the fact that intrinsic spin-orbit coupling is weak in germanium due to crystal inversion symmetry making spin-dependent scattering like Diakonov-Perel mechanism unefficient. Moreover the exchange coupling between electrons and paramagnetic diluted Mn atoms is very weak and we finally found that the phase coherence length is less than the average distance between Mn-rich precipitates limiting electron on them. In angular fits of MR, we have also made the assumption that intervalley scattering time is very short (much shorter than τ_ϕ) and thus neglected the diffusion coefficient anisotropy (*i.e.* the anisotropy of L_ϕ) due to non-spherical Fermi surface in germanium. Fits in figure 3.26(a) were obtained with only two adjustable parameters: $A = 4\%$, close to the value $A = (6\pm2)\%$ calculated using the experimental value of the 2D conductivity at $H = 0$, and $L_\phi = 11.5$ nm, large enough with respect to the thickness of the conducting layer to justify the use of the 2D regime of weak localization. Moreover, fits of the temperature dependence of the anisotropic MR (figure 3.26) were obtained by simply writing $L_\phi = \sqrt{D\tau_\phi}$, using the temperature dependence of the diffusion coefficient D for an n-doped degenerate semiconductor[72], and a temperature dependence of the phase relaxation time $\tau_\phi \propto T^{-\alpha}$ with $\alpha \approx 1.7$, similar to that obtained in [75] for Ge:Sb ($\alpha = 1.5$) and in [76] for Si-MOSFETs ($\alpha = 1.6$), and currently attributed to both electron-electron and electron-phonon collisions.

To sum up this section, n-type As-GeMn samples are highly anisotropic, and the aggregation of As in upper (Ge,Mn) films makes this electronic systems 2D with weak localization effect at low temperatures.

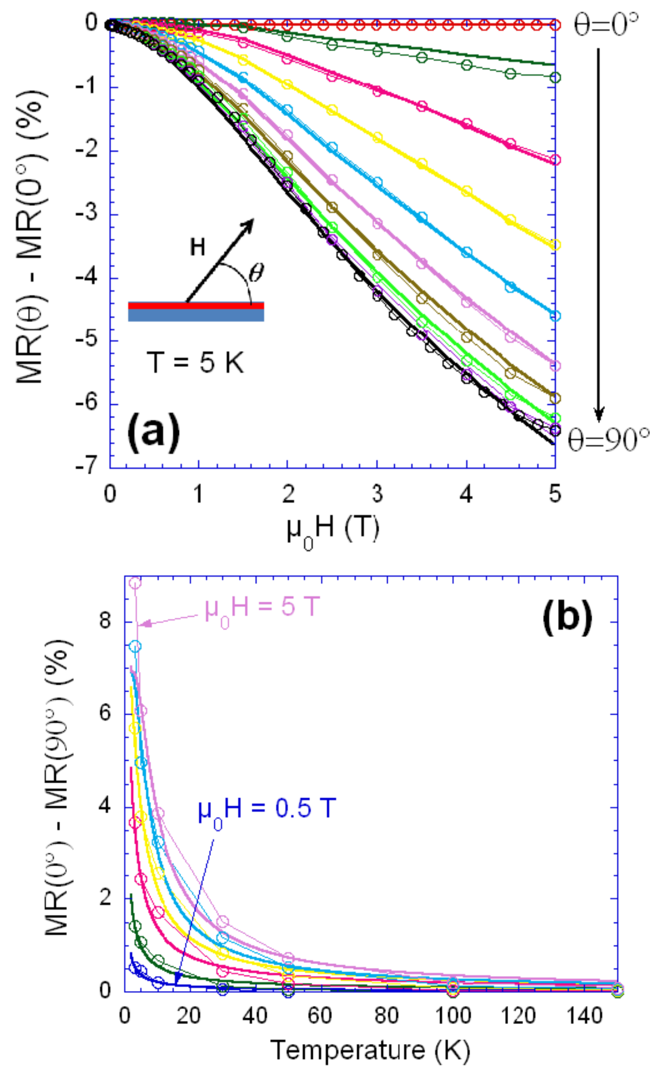

Figure 3.26: Anisotropic Magnetoresistance in As-HT-6%.(a) field dependence and (b) temperature dependence of the MR anisotropy , for different orientations of the field; symbols are experimental data, solid lines are calculated.

Tunneling magnetoresistance

For the isotropic contribution to magnetoresistance of As-HT-6%, which is measured with magnetic field applied in plane (Θ=0) at different temperatures as shown in figure 3.27(a), we can find a negative contribution of MR which vanishes above the Curie temperature of nanoprecipitates (50 K). When we look the MR between -0.4 T and 0.4 T at 5 K and compare with their magnetization from SQUID measurement in figure 3.27(b), it features two maxima at the coercive field of Mn-rich precipitates. Hence, we tentatively ascribe it to tunneling MR (TMR) through the precipitates, and the Schottky barriers formed around them (see the third part of this chapter). By analogy with spin injection from a ferromagnetic metal to a semiconductor[70], efficient spin injection from the precipitates to the matrix requires an interface resistance, provided by the Schottky barrier. This barrier must be high enough to prevent full spin relaxation inside the precipitates but reasonably to allow tunneling MR to occur.

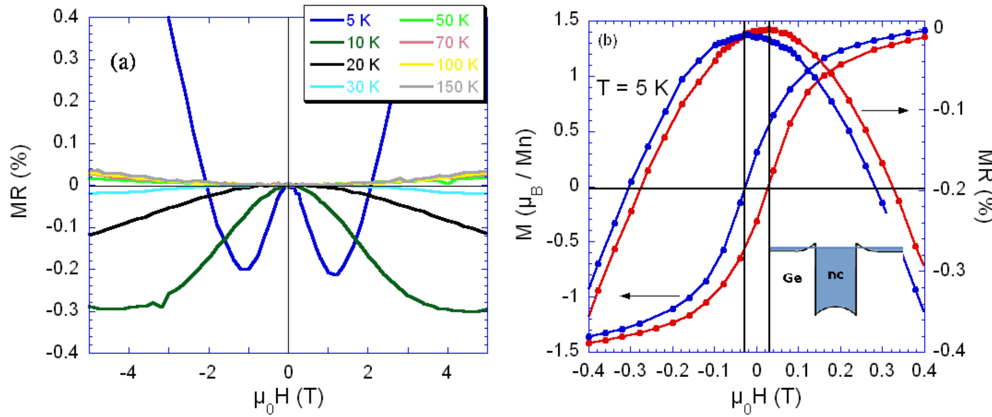

Figure 3.27: TMR of As-HT-6% (a) Isotropic MR as a function of the field applied in-plane at different temperature, (b) Coercive field of Mn-rich precipitates Magnetization and MR at 5 K.

To be brief, in n-type (Ge,Mn) film, isotropic MR is tentatively ascribed to the TMR effect: spin injection from a ferromagnetic metal to a semiconductor with Schottky barrierjunction.

3.3 Discussion and simulation

In this section, we discuss the electron and hole transport behaviors in the Ge matrix containing dispersed Mn-rich nanocolumns. First, the energy-band diagram of the junction between a metal (we assume nanocolumns to be almost metallic) and a semiconductor will be proposed to explain our experimental results. And then, the simulation of magnetotransport will be introduced and employed to calculate the Hall effect and magnetoresistance, which comes from the interaction between holes and Mn-rich ferromagnetic nanocolumns. Finally, we compare the results of experiment and simulation.

3.3.1 Energy-band diagram of nanostructures and Ge matrix

In our non-homogeneous ferromagnetic semiconductor system, Mn-rich nanostructures exist in a Ge matrix with diluted Mn atoms. From the contacting Atomic Force Microscopy (AFM) measurement (not shown), we can find these Mn-rich nanostructures have lower resistivity than Ge matrix. Moreover, X-ray absorption spectroscopy and dichroism evidence the metallic phase of Mn-rich nanostructures[73]. Therefore, for magnetotransport measurement, electrons (As-GeMn samples) and holes (Ga-GeMn samples) transport in the semiconducting Ge matrix with metallic nanostructures. According to our experimental results of previous two sections, we propose an energy-band diagram of the junction between semiconducting Ge matrix and metallic nanostructures as shown in figure 3.28. These are ideal energy-band diagrams for a metal contacting with a n-type semiconductor in As-GeMn samples and a p-type semiconductor in Ga-GaAs samples, and we assume the metal has a high work function (ϕ_m) - or more precisely, the Fermi level in the metal lies in front of the valence band of germanium.

In the first case (n-type semiconductor), there is an ideal barrier (of height ϕ_B) for the transport of electrons (Schottky barrier). This is considered as necessary for the tunneling MR effect to occur, as discussed in section 3.2.3. This barrier also decreases the interaction of electrons and Mn-rich nanoprecipitates, which results in the absence of Anomalous Hall effect (AHE).

For p-type semiconductor, holes can penetrate into the metallic nanostructures directly as shown in figure 3.28. This allows the onset of a Giant MR effect at low temperature since the carriers pass through the nanocolumn where they are expected to experience spin-dependent resistivity. Also, they experience AHE in the nanocolumns, and we will show below that this makes

AHE visible on the whole layer below the T_C of nanocolumns. And finally, we will also show below that this induces a positive MR at low magnetic field (which we call Hall MR effect).

Hence this model of energy-band diagram can qualitatively well explain most of our experimental results.

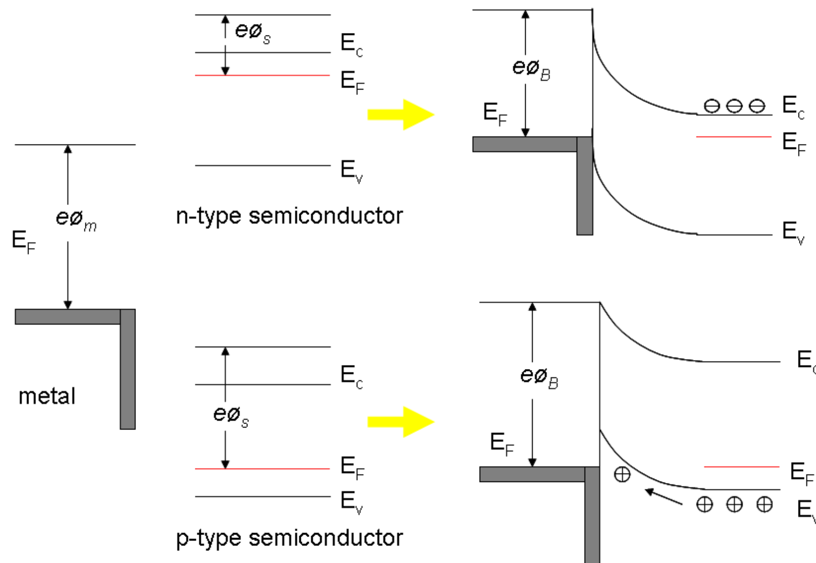

Figure 3.28: Ideal energy-band diagram of the junction between metal and semiconductors: a Schottky barrier forms in n-tpye semiconductors, and an Ohmic contact forms in p-type semiconcuctors.

3.3.2 Simulation of magnetotransport

In this part, we introduce the simulation method of magnetotransport. Then we demonstrate the results of calculations including Hall angle and MR ratio as a function of magnetic field. Finally, we qualitatively compare calculated and experimental data for p-type Ga-GeMn samples.

Simulation method

For the simulation of magnetotransport properties, we have used *Scilab*, *Gmsh* and *GetDP* softwares to calculate the Hall effect and magnetoresistance of the material system like p-type Ga-GeMn samples. First, we introduce these softwares as follows:

- *Scilab* is a high-level, numerically oriented programming language. The language provides an interpreted programming environment, with matrices as the main data type. By utilizing matrix-based computation, dynamic typing, and automatic memory management, many numerical problems may be expressed in a reduced number of code lines.

- *Gmsh* is a 3D finite element grid generator with a build-in CAD engine and post-processor. Its design goal is to provide a fast, light and user-friendly meshing tool with parametric input and advanced visualization capabilities. Gmsh is built around four modules: geometry, mesh, solver and post-processing. The specification of any input to these modules is done either interactively using the graphical user interface or in ASCII text files using Gmsh's own scripting language[74].

- *GetDP* is a general finite element solver using mixed elements to discretize de Rham-type complexes in one, two and three dimensions. The main feature of GetDP is the closeness between the input data defining discrete problems (written by the user in ASCII data files) and the symbolic mathematical expressions of these problems[74].

In our case, we create a geometry like our material system as shown in figure 3.29 and change different parameters to realize the calculation of Hall effect and magnetoresistance.

For the simulation of our material system, we suppose the carrier transport without any barrier at the interface of Mn-rich nanostructure and semiconductor as Ga-GeMn case. In our program of *Scilab*, we can set various parameters such as the dimension (l_x and l_y), dimension of columns (r_{moy}),

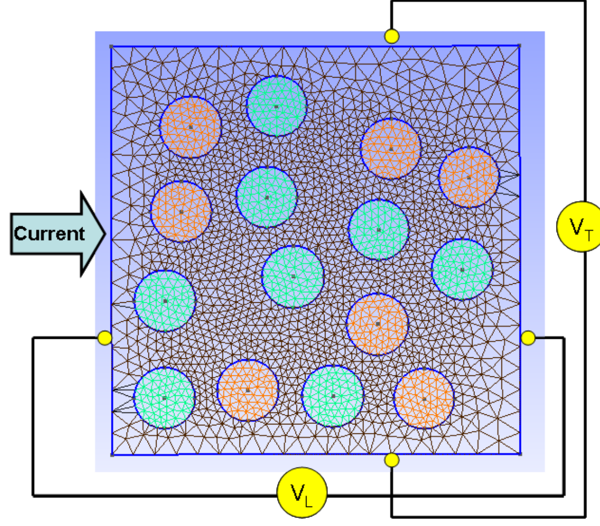

Figure 3.29: Gmsh creates this geometry for the calculation by the software, Scilab.

number of columns (nbc) for geometry parameters. For transport parameters, there are conductivity of matrix ($\sigma_m(0T) \approx 100 \times \mu$, in our case), Hall constant in the matrix ($R_0 = 10^{-6}$, SI units in our case which corresponds to a p-type doping level of $10^{13}m^{-3}$), the ratio of conductivity between columns and matrix ($a = \sigma_c(0T)/\sigma_m(0T)$) and the ratio of Hall constant between columns and matrix ($b = R_s/R_0$). The calculating equations are as follows:

$$\sigma_{c,m}(B, Tesla) = \frac{\sigma_{c,m}(0T)}{1+\beta_{c,m}^2}\begin{pmatrix} 1 & \beta_{c,m} \\ -\beta_{c,m} & 1 \end{pmatrix} \tag{3.4}$$

$$\beta_c = R_s \times \sigma_c(0T) \times \mu_0 M_s \times \frac{2}{\pi} \times Arctan\,(5 \times B) \tag{3.5}$$

$$\beta_m = R_0 \times \sigma_m(0T) \times B \tag{3.6}$$

From the calculation, we have longitudinal resistance ($R_L = V_L/I$) and transverse resistance ($R_T = V_T/I$), and then we can have MR ratio as a function of magnetic field ($MR = 100 \times \left(\frac{R_L(B)-R_L(0)}{R_L(0)})\right)$ and Hall Angle (R_T/R_L) as a function of magnetic field.

Some results from the calculation of magnetotransport

First, to study the role of diameter of nanocolumns in Ge matrix, we set $a = 100$ (ratio of conductivity between columns and matrix) and $b = 1000$

(ratio of Hall constant between columns and matrix) , and we change the parameter of r_{moy} (from $r = 1$ to $r = 5$), and the results are as shown in figure 3.30. As the diameter of nanocolumns increases, both of MR ratio and Hall angle are getting higher. Actually, the general result is simply that the effect increases with the amount of magnetic material in the layer.

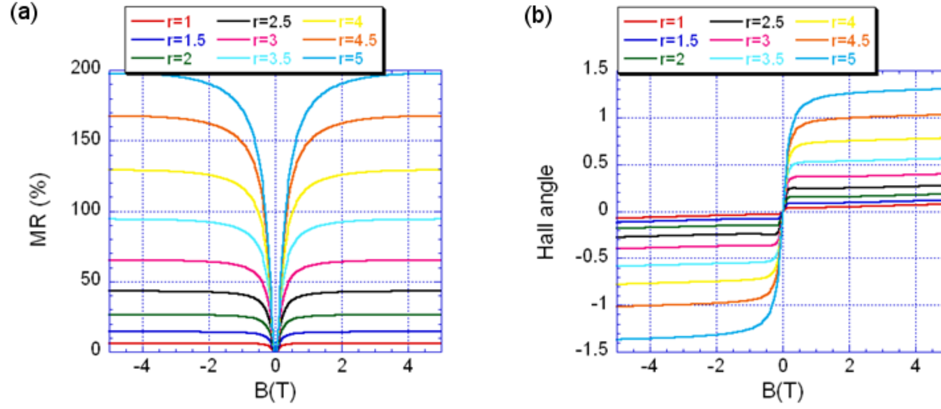

Figure 3.30: The study of different diameters of nanocolumns ($a = 100$, $b = 1000$) (a) MR ratio as a function of magnetic field, and (b) Hall angle as a function of magnetic field.

Second, we consider the transport parameters and fix the geometry parameters. One of transport parameter, a (ratio of conductivity between columns and matrix) is variable, and another parameter, b, is fixed at 100. The results are shown in figure 3.31. As the conductivity ratio decreases to less than 1 (The conductivity of columns is lower than one of matrix), MR and AHE disappear. This is also a simple result: the higher conductivity in the nanocolumns forces the holes to pass through them, and then they are subjected to AHE.

Then, by fixing the geometry parameters, we change the parameter b (ratio of Hall constant between columns and matrix) and set $a = 10$. The results are as shown in figure 3.32. As $b \leq 1$, MR ratio is just attributed to OMR, and AHE disappears. As $b \geq 1$, we find the Hall MR effect increases obviously at low magnetic field regime.

Finally, we include all known effects and try to compare the experimental results with calculated ones. In Ga-GeMn samples (Ga*-LLT-10%, Ga*-LT-10% and Ga*-HT-10%) measured at 50 K, the measurement of MR as a

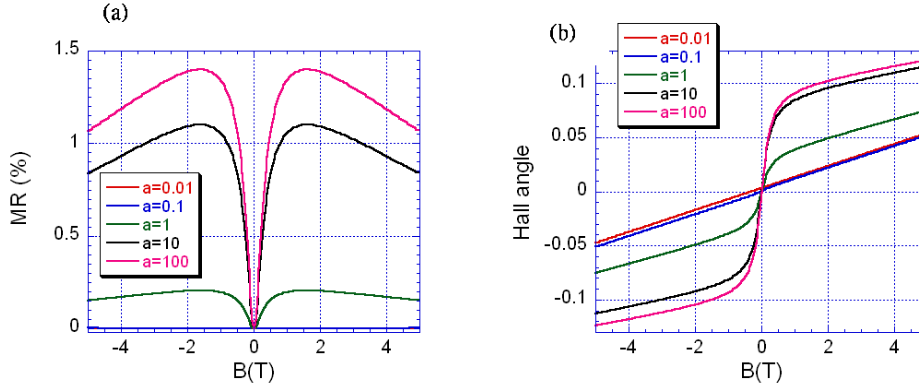

Figure 3.31: The study of conductivity ratio between nanocolumns and matrix ($b = 100$) (a) MR ratio as a function of magnetic field, and (b) Hall angle as a function of magnetic field.

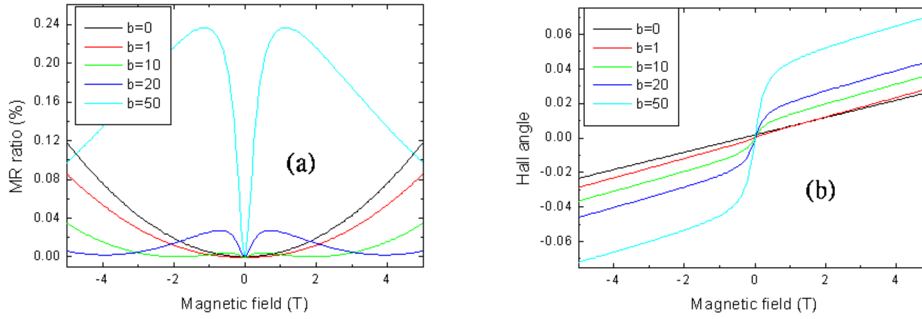

Figure 3.32: The study of Hall constant ratio between nanocolumns and matrix ($a = 10$) (a) MR ratio as a function of magnetic field, and (b) Hall angle as a function of magnetic field.

function of magnetic field is shown in figure 3.33(a), including OMR and HMR (just at low-field regime) . This result is qualitatively similar to the result of calculation in figure 3.32(a). Moreover, the Hall angle as a function of magnetic field is shown in figure 3.33(b), which includes AHE and ordinary HE. This result is similar to the result of calculation in figure 3.32(b).

To summarize this section: we propose a calculating method to have MR ratio and Hall angle as a function of magnetic field, which is qualitatively similar to our experimental results. This supports our attribution of Hall-MR to the AHE in the conducting nanocolumns

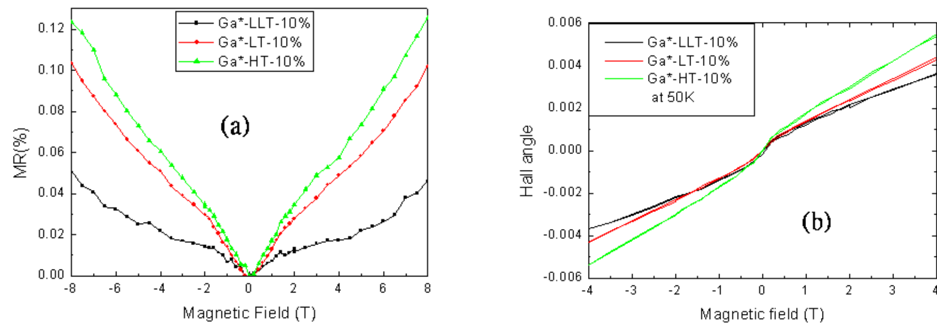

Figure 3.33: Experimental results at 50 K for samples Ga*-LLT-10%, Ga*-LT-10%, and Ga*-HT-10%, (a) MR ratio as a function of magnetic field, (b) Hall angle as a functin of magnetic field.

Chapter 4

Conclusions and outlooks

In this thesis, we have studied the magnetotransport properties of (Ge,Mn) ferromagnetic semiconductor epitaxially grown on GaAs(001), as a first step towards future application in spintronics. By low temperature Molecular Beam Epitaxy , (Ge,Mn) thin films with ferromagnetic nanostructures have been grown on two kinds of GaAs substrates: epiready GaAs(001) (*Ga-GeMn*), and GaAs(001) with an amorphous As capping layer (*As-GeMn*). Our main results are summarized in figure 4.1.

	p-type Ga-GeMn	**n-type As-GeMn**
TEM	Self-organized Mn-rich nanocolumns	3D Mn-rich nanoprecipitates and Ge_3Mn_5 clusters
SIMS	Ga diffusion	As segregation
SQUID	Two magnetic phases (DMS and Mn-rich nanocolumn, Tc=150K)	Three magnetic phases (DMS , nanoprecipitates, Tc=50K, and ferromagnetic Ge_3Mn_5 clusters)
HE	AHE+OHE	OHE
MR	OMR GMR (at low temperature) "HMR" (at low field)	TMR AMR (2D weak localization)

Figure 4.1: Summary of observation on Ga-GeMn and As-GeMn samples.

Main conclusions are as follows:

- *Structure and morphology*: Self-assembled Mn-rich nanocolumns, with T_C=150 K, are obtained on epiready substrates. Depending on the initial surface morphology, they are either parallel (plane surface) or entangled (rough or patterned surface): this confirms the 2D nature of the "spinodal" decomposition, and the role of 2D diffusion and layer-by-layer growth. On As-capped substrates, the presence of As atoms in the growing layer changes the growth mechanism from a 2D spinodal decomposition to a 3D one, with the formation of nanoprecipitates with T_C=50 K, and of ferromagnetic Ge_3Mn_5 clusters.

- *Magnetism*: The magnetic phases in these non-uniform (Ge,Mn) films have been identified by SQUID magnetometry: they are consistent with the observation by TEM.

- *Magnetotransport of Ga-GeMn*: We observe negative MR at low temperature, parabolic ordinary MR, and an additional positive MR at low field. The simulation of magnetotransport properties has been initiated, with some assumptions on the energy-band diagram of p-type Ge semiconductor and Mn-rich nanocolumns, and shows how AHE in the inclusions induces AHE in the whole layer, and a mechanism of MR which accounts for this contribution (which we call Hall MR).

- *MR of As-GeMn*: A highly anisotropic MR is observed in n-type (Ge,Mn) films and shown to be due to weak localization effects. Another contribution is tentatively attributed to tunneling MR due to the Schottky barrier, which forms at the interface between the metallic Mn-rich inclusions and the n-type Ge semiconductor.

For the development of (Ge,Mn) ferromagnetic semiconductor to be applied in future spintronic devices, some interesting questions are still waiting the answers. Some of them are presently studied by collaborators, others will be addressed later:

- Study the crystal structure of Mn-rich nanocolumns, magnetic properties and exchange coupling of nanocolumns in (Ge,Mn) films by X-ray absorption spectroscopy (XAS) and X-ray magnetic circular dichroism (XMCD)[1].

- Control the nucleation of (Ge,Mn) films (embedded nanostructures generating a strain pattern) in order to obtain a 2D positionning of the

[1]S. Tardif, S. Cherifi, J. Cibert (CNRS-Institut Néel), V. Favre-Nicolin (UJF)

nanocolumns, or a 3D superlattice of ferromagnetic segments and grow nanodots of (Ge,Mn)[2].

- Develop a quantitative model of the spinodal decomposition, based on the *ab initio* calculations[3] which they give the formation energy and interface energy of nanocolumns based on an intermetallic (Ge,Mn) phase.

- Develop a quantitative model of magnetotransport. There are some initial results in this thesis[4]. A further step would be to make a link with the results of *ab initio* calculations.

- Study the transport properties of a single Mn-rich nanocolumn[5].

- Study the magnetic anisotropy of (Ge,Mn) by Electron paramagnetic resonance (EPR) and SQUID[6].

---

[2]C. Porret, A. Jain, A. Barski (CEA/INAC/SP2M/SiNaPS) and P. Bayle Guillemaud (/INAC/SP2M/LEMMA)

[3]E. Arras and P. Pochet (CEA/INAC/SP2M/LSim)

[4]A. Marty and M. Jamet (CEA/INAC/SP2M/NM)

[5]R. Mattana, J-M. Georges (CNRS-Thalés) and V. Baltz (CEA/INAC/SPINTEC)

[6]A. Jain, M. Jamet, S. Gambarelli, V. Maurel (CEA/INAC/SCIB)

Bibliography

[1] S. A. Wolf, A. Y. Chtchelkanova, D. M. Treger, *IBM J. Res. and Dev.* **50**, 101 (2006).

[2] G. A. Prinz,*J. Mag. Mag. Mat.* **200**, 57 (1999).

[3] N.F. Mott, *Proc. R. Soc.* **153**, 699 (1936).

[4] P. M. Tedrow, R. Meservey *Phys. Rev. Lett.* **26**, 192 (1971).

[5] M. Julliere, *Phys. Lett. A* **54**, 225 (1975).

[6] M. Johnson and R. H. Silsbee, *Phys. Rev. Lett.* **55**, 1790 (1985).

[7] M. N. Baibich, J. M. Broto, A. Fert, F. Nguyen van Dau, F. Petroff, P. Etienne, G. Creuzet, A. Friederich, J. Chazelas, *Phys. Rev. Lett.* **61**, 2472 (1988).

[8] G. Banisch, P. Grunberg, F. Saurenbach, W. Zinn *Phys. Rev. B* **39**, 4828 (1989).

[9] S. Datta and B. Das, *Appl. Phys. Lett.* **56**, 665 (1990).

[10] G. Schmidt, D. Ferrand, L. W. Molenkamp, A. T. Filip, B. J. van Wees, *Phys. Rev. B* **62**, R4790 (2000).

[11] J. Moodera, P. Leclaire *Nat. Mat.* **2**, 707 (2003).

[12] R. Fiederling, M. Keim, G. Reuscher, W. Ossau, G. Schmidt, A. Waag, L. W. Molenkamp, *Nature* **402**, 787 (1999).

[13] Y. Ohno, D. K. Young, B. Beschoten, F. Matsukura. H. Ohno, D. D. Awschalom, *Nature* **402**, 790 (1999).

[14] H. Ohno, *Science* **281**, 951 (1998).

[15] J. K. Furdyna, *J. Appl. Phys.* **64**, R29 (1988).

[16] F. Matsukura, H. Ohno, A. Shen, Y. Sugawara , *Phys. Rev. B* **57**, R2037 (1998).

[17] K. Wang, R. Campion, K. Edmons, M. Sawicki, T. Dietl, C. Foxon, B. Gallagher, *API Conf. Proc.* **772**, 333 (2005).

[18] T. Dietl, H. Ohno, F. Matsukura, J. Cibert, D. Ferrand, *Science* **287**, 1019 (2000).

[19] A. P. Li, C. Zeng, K. van Benthem, M. F. Chisholm, J. Shen, S. V. S. N. Rao, S. K. Dixit, L. C. Feldman, A. G. Petukhov, M. Foygel, H. H. Weitering, *Phys. Rev. B* **75**, R201201 (2007).

[20] D. Bougeard, S. Ahlers, A. Trampert, N. Sircar, G. Abstreiter, *Phys. Rev. Lett.* **97**, 237202 (2006).

[21] M. Jamet, A. Barski, T. Devillers, V. Poydenot, R. Dujardin, P. Bayle-Guillemaud, J. Rothman, E. Bellet-Amalric, A. Marty, J. Cibert, *et al.*, *Nature Mater.* **5**, 653 (2006).

[22] L. Gu, S. Y. Wu, H. X. Liu, R. K. Singh, N. Newman, D. J. Smith, *J. Magn. Magn. Mat.* **290-291**, 1395 (2005).

[23] A. Bonanni, A. Navarro-Quezada, T. Li, M. Wegscheider, Z. Matej, V. Holy, R. T. Lechner, G. Bauer, M. Rovezzi, F. D'Acapito, M. Kiecana, M. Sawicki, T. Dietl, *Phys. Rev. Lett.* **101**, 135502 (2006).

[24] S. Kuroda, N. Nishizawa, K. Takita, M. Mitome, Y. Bando, K. Osuch, T. Dietl, *Nature Mater.* **6**, 440 (2007).

[25] H. Ohno, D. Chiba, F. Matsukura, T. Omiya, E. Abe, T. Dietl, Y. Ohno, K. Ohtani, *Nature* **408**, 944 (2000).

[26] K. Sato, H. Katayama-Yoshida, P. H. Dederichs, *Jpn. J. Appl. Phys.* **44**, L948 (2005).

[27] T. Fukushima, K. Sato, H. Katayama-Yoshida, P. H. Dederichs, *Jpn. J. Appl. Phys.* **45**, L416 (2006).

[28] I. Zutic, J. Fabian, S. C. Erwin, *Phys. Rev. Lett.* **97**, 026602 (2006).

[29] Y. D. Park, A. T. Hanbicki, S. C. Erwin, C. S. Hellberg, J. M. Sullivan, J. E. Mattson, T. F. Ambrose, A. Wilson, G. Spanos, B. T. Jonker, *Science* **295**, 651 (2002).

[30] T. B. Massalski, *Binary Alloy Phase Diagram, vol.2,*(American Society of Metals, OH, 1990).

[31] R. B. Morgunov, A. J. Dmitriev, O. L. Kazakova, *Phys. Rev. B* **80**, 085205 (2009).

[32] Y. J. Cho, C. H. Kim, H. S. Kim, W. S. Lee, S.-H. Park, S. Y. Bae, B. Kim, H. Lee, J.-Y. Kim, *Chem. Mater.* **20**, 4694 (2008).

[33] P. D. Padova, J.-P. Ayoub, I. Berbezier, P. Perfetti, C. Quaresima, A. M. Testa, D. Fiorani, B. Olivieri, J.-M. Mariot, A. Taleb-Ibrahimi, M. C. Richter, O. Heckmann, K. ricovini, *Phys. Rev. B* **77**, 045203 (2008).

[34] L. Morresi, J. Ayoub, N. Pinto, M. Ficcadenti, R. Murri, A. Ronda, I. Berbezier, *Mat. Sci. Semicond. Process* **9**, 836 (2006).

[35] C. Bihler, C. Jaeger, T. Vallaitis, M. Gjukic, M. S. Brandt, E. Pippel, J. Woltersdorf, U. Gosele, *Appl. Phys. Lett.* **88**, 112506 (2006).

[36] Y. D. Park, A. Wilson, A. T. Hanbicki, J. E. Mattson, T. Ambrose, G. Spanos, B. T. Jonker, *Appl. Phys. Lett.* **78**, 2739 (2001).

[37] L. Ottaviano, M. Passacantando, A. Verna, R. Gunnella, E. Principi, A. D. Cicco, G. Impellizzeri, F. Priolo, *J. Appl. Phys.* **100**, 063528 (2006).

[38] J.-S. Kang, G. Kim, S. C. Wi, S. S. Lee, S. Choi, Sunglae Cho, S. W. Han, K. H. Kim, H. J. Song, H. J. Shin, A. Sekiyama, S. Kasai, S. Suga, B. I. Min, *Phys. Rev. Lett.* **94**, 147202 (2005).

[39] S. Ahlers, D. Bougeard, N. Sircar, G. Abstreiter, A. Trampert, M. Opel, R. Gross, *Phys. Rev. B* **74**, 214411 (2006).

[40] T. Dietl, F. Matsukura, H. Ohno, J. Cibert, D. Ferrand, *arXiv: cond-mat/0306484 v2 20 Jun 2003*

[41] F. Matsukura, H. Ohno, A. Shen, Y. Sugawara, *Phys. Rev. B* **57**, R2037 (1998).

[42] F. Tsui, L. He, L. Ma, A. Tkachuk, Y. S. Chu, K. Nakajima, T.Chikyow, *Appl. Phys. Lett.* **91**, 177203 (2003).

[43] J. X. Deng, Y. F. Tain, S. M. He, H. L. Bai, T. S. Xu, S. S. Yan, Y. Y. Dai, T. X. Chen, G. L. Liu, L. M. Mei, *Appl. Phys. Lett.* **95**, 062513 (2009).

[44] R. Tuschida, J. T. Asubar, Y. Jinbo, N, Uchitomi, *J. Crys. Grow.* **311**, 937 (2009).

[45] O. Riss, A. Gerber, I. Ya. Korenblit, A. Suslov, M. Passacantando, L. Ottivaiano *Phys. Rev. B* **79**, 241202(R) (2009).

[46] A. Y. Cho, J. R. Arthur, *Prog. Solid State Chem.* **10**, 157 (1975).

[47] T. Devillers, *Etude des propriétés physiques des phases de $Ge_{1-x}Mn_x$ ferromagnetiques pour l'électronique de spin*, (2008).

[48] A. Ichimiya, P. I. Cohen *Reflection High Energy Electron Diffraction* (Cambridge University Press, 2004).

[49] J. E. Hilliard, *Spinodal Decomposition in Phase Transformation*, (American Society of Metals, Metals Park, 1970).

[50] D. B. Williams, C. B. Carter, *Transmission Electron Microscopy*, (Plenum Press, New York and London, 1996).

[51] W. Cai, J. Wan *J. Coll. Inter. Scie.* **305**, 366 (2007).

[52] C. Kittel, *Introduction to Solid State Physics*, (1996).

[53] E. H. Hall, *Am. J. Math.* **2**, 287 (1879).

[54] N. A. Sinitsyn, *J. Phys.: Condens. Matter.* **20**, 023201 (2008).

[55] R. Karplus and J. M. Luttinger, *Phys. Rev.* **100**, 580 (1954).

[56] J. Smit, *Physica* **24**, 39 (1958).

[57] L. Berger, *Phys. Rev. B* **2**, 4559 (1970).

[58] T. Shinjo, *Nanomagnetism and Spintronics*, (2009).

[59] P. L. Rossiter, *The Electrical Resistivity of Metals and Alloys*, (2009).

[60] C. L. Chien, *Annual Review of Materials Science* **25**, 129 (1995).

[61] J. Q. Xiao, J. S. Jiang and C. L. Chien, *Phys. Rev. Lett.* **68**, 3749 (1992).

[62] A. E. Berkowitz, J. R; Mitchell, M. J. Carey, A. P. Young, S. Zhang, F. E. Spata, F. T. Parker, A. Hutten, G. Thomas, *Phys. Rev. Lett.* **68**, 3745 (1992).

[63] T. Devillers, M. Jamet, A. Barski, V. Poydenot, P. Bayle-Guillemaud, E. Bellet-Amalric, S. Cherifi, J. Cibert, *Phys. Rev. B* **76**, 205306 (2007).

[64] A. Lecycuras, *Appl. Phys. Lett.* **66**, 1800 (1995).

[65] Y. Tawara, K. Sato, *J. Phys. Soci. Jap.* **18**, 773 (1963).

[66] T. Dietl, *J. Appl. Phys.* **103**, 07D111 (2008).

[67] G. Ottaviani, C. Canali, C. Jacoboni, A. Alberigi Quaranta, and K. Zanio, *J. Appl. Phys.* **44**, 360 (1973).

[68] W. Zhu, Z. Zhang, and E. Kaxiras, *Phys. Rev. Lett.* **100**, 027205 (2008).

[69] W. Zhu, Z. Zhang, and E. Kaxiras, *Phys. Rev. Lett.* **93**,673 (2004).

[70] A. Fert and H. Jaffres, *Phys. Rev. B* **64**, 184420 (2001).

[71] B. L. Altshuler and A. G. Aronov, in *Electron - Electron Interactions in Disordered Systems*, edited by A. L. Efros and M. Pollak (North-Holland, Amsterdam, 1985).

[72] S. M. Sze, *Physics of Semiconductors Devices* (Wiley, New York, 1981).

[73] S. Tardif, I.-S. Yu, T. Devillers, M. Jamet, S. Cherifi,J. Cibert, A. Barski, P. Bayle-Guillemaud, E. Bellet-Amalric, *Proc. SPIE* **7036**, 40 (2008).

[74] C. Geuzaine, J.-F. Remacle, *Inte. J. Nume. Meth. Engi.* **0**, 1 (2009).

[75] T. A. Polyanskaya *et al.*, *Sov. Phys. JETP Lett.* **34**, 361 (1981).

[76] M. J. Uren *et al.*, *J. Phys. C* **14**, L395 (1981).

[77] T. C. Schulthess and W. H. Butler, *J. Appl. Phys.* **89**, 7021 (2001).

[78] H. H. Woodbury, W. W. Tyler, *Phys. Rev.* **100**, 659 (1955).

[79] R. Newman, H. H. Woodbury and W. W. Tyler *Phys. Rev.* **102**, 613 (1956).

[80] T. Dietl, F. Matsukura, H. Ohno, J. Cibert and D. Ferrand, *Cond. Mat.* **2**, 0306484 (2003).

[81] B. T. Josephon, *Phys. Lett.* **1**, 251 (1962).

Résumé

En utilisant l'épitaxie par jets moléculaires á basse température, nous avons élaboré des couches de (Ge,Mn), contenant des nanostructures ferromagnétiques, sur deux types de substrats GaAs d'orientation (001) : des substrats GaAs *epiready* (échantillons *Ga-GeMn*), et des substrats encapsulés par de l'arsenic amorphe (échantillons *As-GeMn*).

Dans les échantillons Ga-GeMn, nous obtenons la formation de nanocolonnes riches en Mn ; celles-ci sont paralléles entre elles, ou enchevêtrées, suivant la morphologie de surface initiale. Les mesures de magnétométrie révélent deux phases magnétiques : les nanocolonnes ferromagnétiques avec une température de Curie de 150 K, et la matrice de germanium, rendue paramagnétique par la présence de Mn dilué. Les mesures de magnétotransport montrent que ces couches sont de type p, et révélent un l'effet Hall anormal (AHE) et plusieurs contributions á la magnétorésistance : une magnétorésistance géante négative, á basse température, la magnétorésistante orbitale, parabolique, et une contribution supplémentaire á faible champ. Un calcul des propriétés de magnétotransport a été commencé en s'appuyant sur des hypothéses de la structure de bande entre les inclusions riches en Mn et la matrice semiconductrice de type p : celui-ci montre que la présence d'AHE dans les inclusions donne naissance á un AHE sur tout l'échantillon, mais aussi á un mécanisme de magnétorésistance qui rend compte de cette contribution (que nous appelons magnétorésistance Hall).

Dans les échantillons As-GeMn, la diffusion de l'arsenic change le mode de croissance, avec une décomposition spinodale qui perd son caractére bidimensionnel pour devenir tridimensionnelle, avec la formation d'agrégats riches en Mn (température de Curie de l'ordre de 50 K) et d'agrégats de la phase ferromagnétique connue Ge_3Mn_5. La compensation entre Mn (accepteur) et As (donneur) gouverne les propriétés de transport. Dans les couches de type n, une forte anisotropie de la magnétorésistance est observée, dont nous montrons qu'elle est due á des effets de localisation faible. Une autre contribution á la magnétorésistance est observée, que nous suggérons d'attribuer á une magnétorésistance tunnel á travers la jonction Schottky qui se forme á l'interface entre les inclusions riches en Mn, qui sont métalliques, et le semiconducteur Ge de type n.

Mots clefs: semiconducteur ferromagnétique, magnétorésistance géante, effets de localisation faible, magnétorésistance tunnel, MBE, AHE

Abstract

By low temperature Molecular Beam Epitaxy (MBE), (Ge,Mn) thin films with ferromagnetic nanostructures are grown on two kind of GaAs substrates: *epiready* GaAs(001) (*Ga-GeMn*) and GaAs(001) with amorphous As capping layer (*As-GeMn*).

In the Ga-GeMn samples, we observe self-organized Mn-rich nanocolumns which, depending on the initial surface morphology, are either parallel or entangled. Magnetic measurements evidence two magnetic phases: ferromagnetic nanocolumns with Curie temperature around 150K, and the Ge matrix made paramagnetic by diluted Mn. From measurements of magnetotransport, this p-type layer exhibits anomalous Hall effect (AHE) and various magnetoresistivity (MR): negative Giant MR at low temperature, parabolic ordinary MR, and an additional positive MR at low field. The simulation of magnetotransport properties has been initiated, with some assumptions on the energy-band diagram of p-type Ge semiconductor and Mn-rich nanocolumns, and shows the way that AHE in the inclusions induces AHE in the whole layer, and a mechanism of MR which accounts for this contribution (which we call Hall MR).

In the As-GeMn samples, the outdiffusion of As atoms changes the growth mechanism, from a 2D spinodal decomposition to a 3D one with the formation of nanoprecipitates with Tc=50K and of ferromagnetic Ge_3Mn_5 clusters. Compensation effect between Mn (donor) and As (acceptor) dominates the transport behaviors. A highly anisotropic MR is observed in n-type (Ge,Mn) films and shown to be due to weak localization effects. Another contribution is tentatively attributed to tunneling MR due to the Schottky barrier, which forms at the interface between the metallic Mn-rich inclusions and the n-type Ge semiconductor.

Keywords: ferromagnetic semiconductor, Giant magnetoresistivity, weak localization effect, tunneling magnetoresistivity, MBE, AHE